

Molassembler: Molecular graph construction, modification and conformer generation for inorganic and organic molecules

Jan-Grimo Sobez¹ and Markus Reiher²

Laboratory of Physical Chemistry, ETH Zurich,
Vladimir-Prelog-Weg 2, 8093 Zurich, Switzerland

June 26, 2020

Abstract

We present the graph-based molecule software MOLASSEMBLER for building organic and inorganic molecules. MOLASSEMBLER provides algorithms for the construction of molecules built from any set of elements from the periodic table. In particular, poly-nuclear transition metal complexes and clusters can be considered. Structural information is encoded as a graph. Stereocenter configurations are interpretable from Cartesian coordinates into an abstract index of permutation for an extensible set of polyhedral shapes. Substituents are distinguished through a ranking algorithm. Graph and stereocenter representations are freely modifiable and chiral state is propagated where possible through incurred ranking changes. Conformers are generated with full stereoisomer control by four spatial dimension Distance Geometry with a refinement error function including dihedral terms. Molecules are comparable by an extended graph isomorphism and their representation is canonicalizable. MOLASSEMBLER is written in C++ and provides Python bindings.

¹ORCID:0000-0002-3264-0622

²Corresponding author; e-mail: markus.reiher@phys.chem.ethz.ch; ORCID:0000-0002-9508-1565

1 Introduction

Software encoding of molecules has become indispensable to many research fields. Significant effort has been invested into the formal description of organic molecules, owing to their importance as small-molecule drugs amenable to a characterization by chemical concepts. A trove of open-source cheminformatics programs exists serving various needs.^{1,2} Many of these computer programs have some support for inorganic molecules, for which reliable and simple chemical principles are more difficult to define owing to an increased electronic structure. For example, take fragment-based³ and evolutionary⁴ organometallic compound design applications, whose primary conformer generation is facilitated by Marvin⁵ and Chemistry Development Kit,⁶ respectively.

The set of software whose primary focus is an encoding of organometallic and inorganic molecules is small, but steadily expanding. The high-level complex generator molSimplify⁷ is based on three-dimensional manipulation of preoptimized molecular fragments. AARON⁸ automates the generation of configurations and conformations of organometallic molecules in transition-metal catalytic explorations. HostDesigner⁹ selects ligands to complement metal ion guests. DENOPTIM¹⁰ is a fragment-based transition metal compound design tool. The fast quantum mechanical metadynamics conformer ensemble generator CREST¹¹ and a related force-field method GFN-FF¹² for molecular mechanics are further recent additions.

For our efforts toward the automated exploration of chemical reaction networks based on first-principles heuristics,¹³⁻¹⁵ we require structure-identification and -construction algorithms that are applicable to molecules composed of any element from the periodic table (in particular, to inorganic compounds) in order not to restrict explorations to irrelevant parts of chemical reaction space if certain reactants cannot be represented. No existing cheminformatics implementation provides the capabilities required for truly general mechanism exploration algorithms that identify nodes in a reaction network as chemical species described by a graph. To be more specific, the requirements for this purpose are: (i) The algorithm must be able to interpret a local minimum on the Born-Oppenheimer potential energy hypersurface as a chemical graph and capture the stereochemical configuration. (ii) The molecular model must encompass multidentate and haptic ligands. (iii) It must be possible to change the connectivity of atoms and enumerate all stereoisomers without restriction. (iv) Molecules must be comparable. (v) It must be possible to generate new conformers of molecules. This set of features does not exist in any software supporting inorganic molecules, because bonding patterns and stereochemistry in inorganic molecules present significant challenges for cheminformatics tools due to their immense variability.

This variability affects how atom-centered chirality manifests. Compared to organic chemistry, the most complicated chiral unit will no longer be the tetrahedron with at most two distinct spatial arrangements (i.e., R or S) if its substituents are all deemed different by a ranking algorithm. Instead, the local shape can have as many as twelve vertices and most vertex counts accommodate multiple shapes. For instance, five sites can arrange into idealized shapes of a trigonal bipyramid, a square pyramid or a pentagon. The number of distinct spatial arrangements for the maximally asymmetric substitution situation scales approximately as the factorial of the number of sites. Note also that individual shape vertices are not necessarily occupied by single atoms, but possibly by multiple atoms in a haptic configuration.

The degree to which these ostensibly slight structural changes complicate the design of algorithms necessarily depends on the specific aims of the molecule construction software. Let us consider some of the consequences of the proposed aims individually: In order to interpret a local minimum of the potential energy hypersurface as a chemical graph and capture the stereochemical configuration, the software must base its atom-connectivity representation on a graph and find a data representation of stereocenters that is general, and in particular, suitable for inorganic molecules. Returning to atom-centered chirality, this implies that for an arbitrary local shape, the software must enumerate rotationally non-superimposable arrangements of variable numbers of different substituents. This enumeration must consider the effects of site interconnectivity for multidentate ligands and abstract away the additional complication of haptic binding. The algorithm must decide which substituents are chemically different with a ranking algorithm that encompasses stereodescriptors of inorganic stereocenters.

Local shapes and especially non-superimposable arrangements within those shapes must be reliably identifiable from Cartesian coordinates. An imposed rigid model of chiral arrangements might also consider interconverting molecular dynamics such as nitrogen inversion to avoid overstating chiral character. Given a molecule's connectivity, deciding on the local shape at each non-terminal atom involves more complex electronic structures. For a reasonable degree of accuracy, it will in general be insufficient to base this decision on simple concepts such as Gillespie's valence shell electron pair repulsion. If the molecular graph and the stereocenter representations are to be freely modifiable and if they are identified through relative substituent ranking, stereodescriptors must be propagated through the ranking changes that arbitrary edits can incur. For editing continuity, stereocenters should not generally lose their state upon addition or removal of a site while transitioning between different molecular structures (shapes).

Moreover, the comparison of molecules will require the implementation of a graph isomorphism and optionally a graph canonicalization algorithm to accelerate re-

peated comparisons. Generation of conformations of arbitrary graphs requires a spatial model that can encompass multidentate and haptic ligands and a methodology that reliably generates specific stereocenter configurations in Cartesian coordinates.

Note that model-free molecule comparison algorithms such as G-RMSD,¹⁶ and continuous representations of molecules¹⁷ are certainly also viable approaches to some of the challenges we seek to solve. However, we do not consider direct comparisons of Cartesian coordinates through measures such as root mean square deviations an option here, because increasing deviations may be expected for increasing molecule sizes of structures that actually resemble the same compound.

In this work, we present a new molecular construction software, MOLASSEMBLER, that seeks to encompass organometallic and inorganic bonding patterns in a more complex graph-based model. Comparably few of these sub-problems of our non-exhaustive list require entirely new solutions. Many can be solved by implementing existing algorithms or through careful extension of existing partial solutions, as we will discuss in the following. For instance, we will show that through partial abstraction of the International Union of Pure and Applied Chemistry (IUPAC) organic ranking sequence rules,¹⁸ a configurational index of permutation can serve as a comparative stereodescriptor in a ranking algorithm. Moreover, through extension, the original algorithm can serve to differentiate not merely direct graph substituents, but binding sites. By contrast, the canonicalization of stereodescriptors and their propagation into new structures (shapes) or through ranking changes will require new solutions.

2 Molecule model

MOLASSEMBLER applies a molecule model split into an undirected graph and a list of data structures named stereopermutators. Vertices of the graph represent atoms, each storing an element type. Edges of the graph represent bonds, storing an idealized bond order (i.e., an integer number that may be extracted from a real-valued bond order obtained from a quantum mechanical analysis of the electronic wave function). Idealized bond types comprise bond orders from single to sextuple and an algorithm-internal special bond called 'eta' indicating connectivity to an atom forming part of a haptic binding site following the η -notation¹⁹ for such bonding situations. The molecular graph must form a single connected component. Accidental graph disconnects upon atom or bond removal are prevented by permitting only the removal of non-bridge bonds or non-articulation vertices (removal of articulation vertices would enlarge the number of connected components). Intentional molecule

splitting along bridge bonds is possible through specialized functions.

Stereopermutators manage relative spatial orientations of groups of bonded atoms. They reduce the set of relative spatial orientations to an abstract permutational space. Special relative spatial orientations are reduced to an index of permutation. Collectively, stereopermutators capture a molecule’s configurational space. Stereopermutators are not named stereocenters because they also manage non-stereogenic cases. MOLASSEMBLER comprises two types of stereopermutators: Atom-centered stereopermutators capture configurational differences between different orientations of the direct graph adjacents of a central atom. Bond-centered stereopermutators capture configurational differences arising due to rotational barriers along bonds.

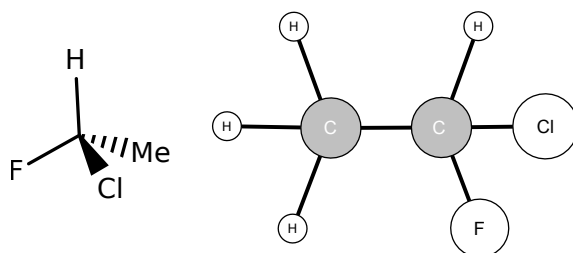


Figure 1: Illustration of spatial structure and molecule graph. *Left:* A typical Lewis structure encoding also stereoinformation. *Right:* The connectivity of this molecule represented as a graph.

Consider the example given in Figure 1. The graph of the Lewis structure captures its connectivity, but not its spatial shape or chiral character. In addition to the graph, this requires two atom-centered stereopermutators. One is placed at the methyl group’s carbon atom, indicating a tetrahedral local shape and an abstract binding situation AAAB (three ranking-identical hydrogen atoms and one different group), for which case there are no multiple non-superimposable arrangements. That stereopermutator is therefore not stereogenic. The other stereopermutator is placed at the carbon atom central in the Lewis structure. It also has a tetrahedral local shape, but ranking-wise all its substituents are different in an ABCD abstract binding situation. In that shape, there are two non-superimposable spatial permutations of its substituents. The Lewis structure represents the S variation of this stereocenter, and the stereopermutator represents it as an index of permutation that parallels the IUPAC stereodescriptor.

Our molecular representation model is capable of transferring molecular structures at local minima on the Born-Oppenheimer potential energy surface given in Cartesian coordinates to an abstract permutational space in which configurational variations can be enumerated easily and transformed back into Cartesian coordinates via conformer generation close to local minima on the potential energy surface. However, the model is not well suited for capturing structural elements of other regions of the

potential energy surface.

MOLASSEMBLER places no structural limitations on the graph aside from constraining it to remain a single connected component. As a consequence, it is possible to generate graphs for which MOLASSEMBLER cannot generate a spatial model allowing the graph to be embedded into three dimensions, such as the set of complete graphs (i.e., those in which all vertices are connected with all other vertices) with more than four vertices. Deciding graph embeddability in three dimensions is NP-hard,²⁰ and no attempt is made to guarantee that a supplied graph is embeddable during its construction.

In the following sections, we discuss the individual domains of responsibility for atom- and bond-centered stereopermutators, the implemented ranking algorithm, manipulation of molecules and conformer generation.

3 Local shapes and stereopermutations

Atom-centered stereopermutators manage the spatial orientation of the graph substituents of a non-terminal atom by abstracting into a permutational space in which each permutation constitutes a mutually non-superimposable spatial orientation. If multiple permutations are geometrically feasible, the respective atom is a stereocenter.

The local spatial arrangement of an atom’s substituents is classified into a set of idealized polyhedral shapes. MOLASSEMBLER currently comprises thirty different shapes ranging from two to twelve vertices. The choice of shapes aims to reflect common geometric patterns while avoiding too fine distinctions. All chosen shapes are spherical, i.e. within their coordinate frames, all vertices of the encoded shapes have the same distance from the origin. The first class of chosen shapes is of reduced dimensionality and contains the following shapes: Line, bent line, equilateral triangle, T-shape, regular square, pentagon, and hexagon.²¹ Next, four of the five Platonic solids are included: tetrahedron, octahedron, cube, and icosahedron. Then, some other polyhedra composed of regular faces: Uniform triangular prism, square antiprism, and cuboctahedron. Several Johnson solids are included without modification as they are by construction spherical: Square pyramid, pentagonal pyramid, trigonal bipyramid, and pentagonal bipyramid. Furthermore, the hexagonal and heptagonal bipyramids are also included. Several non-spherical Johnson solid shapes have been spherized by projection onto a sphere and subsequent minimization on the Thomson potential²² to a local minimum that retains the original point group symmetry: Capped square antiprism, trigonal dodecahedron, and capped trigonal

prism. The shapes of the global minima for nine, ten and eleven particles on the Thomson potential are also included: Tricapped trigonal prism, bicapped square antiprism and edge-contracted icosahedron. Lastly, some derived shapes are also present: Capped octahedron, a tetrahedron with one vertex vacant and both apical- and equatorial-monovacant variations of the trigonal bipyramid. The spatial arrangement of a non-terminal atom's immediate substituents can be classified as one of these shapes, as demonstrated in Figure 2.

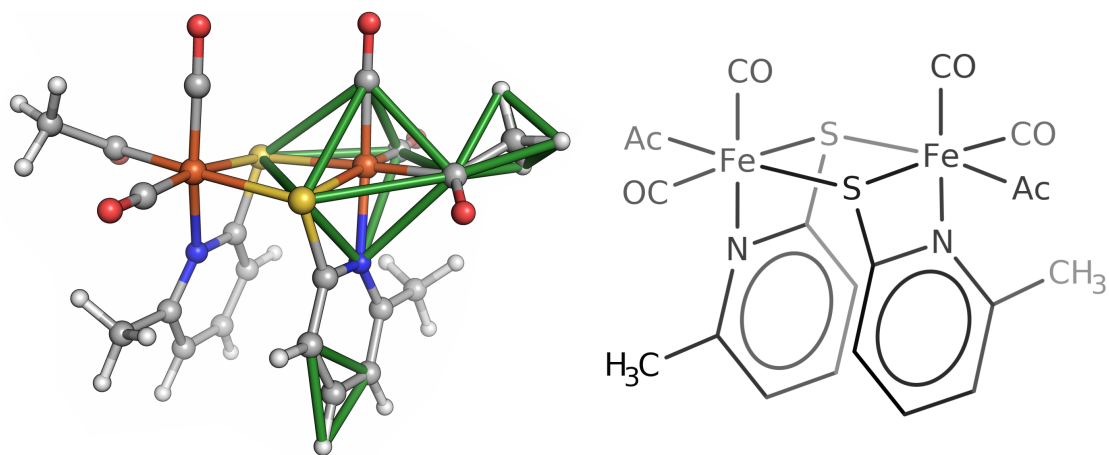


Figure 2: *Left*: An example of a molecule with classified shapes shown in green for three of its non-terminal atoms: An equilateral triangle at the bottom, an octahedron in the center, and a tetrahedron at the right edge. *Right*: Simplified Lewis structure of the left compound. Images of molecules in Cartesian coordinates were generated with PyMOL,²³ simplified Lewis structures with MarvinSketch.²⁴ Atom coloring: Hydrogen in white, carbon in gray, oxygen in red, iron in orange, sulfur in yellow, and nitrogen in blue.

A binding site is a contiguous set of vertices adjacent to a central atom. If a site comprises more than a single atom, the binding site is haptic and the bonds of its edges (collected and idealized, for instance, from bond orders evaluated from an electronic wave function) to the central atom vertex are relabeled as eta bonds. Spatially, a binding site's vertex-set centroid is modeled to co-locate with a vertex of the local shape as shown in Figure 3. Haptically binding atoms are free to rotate around the axis defined by the local shape's central atom and the binding site's vertex-set centroid.

Binding sites are ranked by an algorithm described in Section 7. Ranking is necessary to decide which binding sites are chemically different. Permuting chemically identical groups does not create a new non-superimposable configuration, which must be considered in the enumeration of stereopermutations. Links between binding sites, and by proxy multidentate ligands, are identified with cycle perception from the

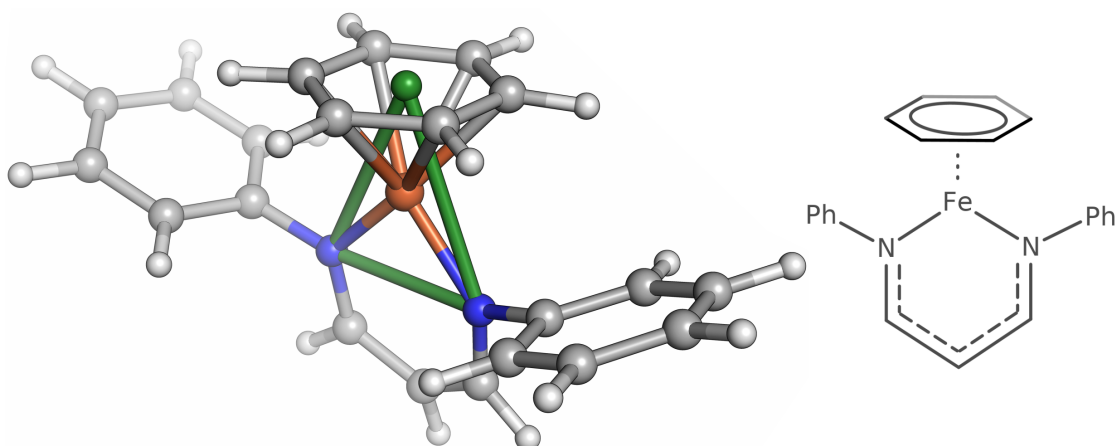


Figure 3: *Left:* An example of a molecule with a haptic binding site. The central iron atom has two binding sites consisting of single nitrogen atoms. The carbon atoms of the benzene molecule above the iron atom form a third binding site, as they are a contiguous group of atoms bonded to the central iron atom. The centroid of the haptic binding site is shown as a pseudoatom in the center of the carbocycle. The shape of the substituents of the central iron atom has three vertices, one for the centroid of each binding site, and is classified as an equilateral triangle, shown in green. *Right:* Simplified Lewis structure of the left compound. Atom coloring: Hydrogen in white, carbon in gray, nitrogen in blue, and iron in orange.

external software library RingDecomposerLib.²⁵

From an idealized shape, a set of binding sites, their ranking, and their links, MO-LASSEMBLER enumerates a set of abstract non-superimposable permutations following a method reported in the literature.²⁶ In preparation, the ranked sites and their links are transformed into an abstract case such as AA(B-C) that merely reflects whether sites are different from one another and their connectivity. This is done by transforming the nested list of ranked sites into a flat list where each site is represented by an incrementing character. Within the considered shape, all permutations of vertex occupations are generated and the rotationally non-superimposable permutations are collected. These are the stereopermutations of the abstract case within the considered shape.

Generating a mapping from sites to shape vertices for a particular stereopermutation will be nontrivial if links (paths between site constituting atoms not including the central atom) exist and there are multiple sites with equal ranking. In any situation, it is possible to represent the ranked sites and their links as a colored graph: Vertices are sites and links are edges between sites. Similarly, a stereopermutation can be represented as a graph: Vertices are shape vertices and edges are their links. Any isomorphism mapping between the two graphs is a valid mapping from sites to shape

vertices.

Within stereopermutation enumeration, three-dimensional feasibility of links between binding sites in each permutation is not considered. For instance, a bidentate oxalate ligand cannot coordinate in a trans-arrangement within an octahedron shape, but must be cis-coordinated: stereopermutations in which its sites are trans-arranged are not viable in three dimensions. Such stereopermutations arise in the abstract permutational scheme, and must be removed to avoid false classification of an atom as a stereocenter and unexpected failures in conformer generation. We consider it undesirable to exclude trans-ligating arrangements on principle for specific shapes and prefer to make general geometric arguments on a case-to-case basis. Unfeasible stereopermutations are avoided by probing whether a cyclic polygon can be modeled for each links' cycle without non-binding atoms of the bridge entering a bonding distance to the central atom. This geometric algorithm is depicted in Figure 4. The cyclic polygon was chosen because it maximizes the area of the polygon and by proxy the distance of its vertices from the original center. This scheme will identify individual cycles that, when modeled in a particular stereopermutation, would contradict the graph, but miss instances where multiple individually feasible cycles are impossible to realize jointly. For instance, in an octahedral shape with three bidentate ligands with bridges of sufficient length to achieve trans-ligation individually, this scheme will not remove the stereopermutation in which all are ligated in a trans-arrangement. If the bridges are too short for each to distort sufficiently to accommodate the others, conformer generation will fail. It may be possible to discover a lack of viability by modeling all bridges in a joint distance bounds matrix and applying triangle and tetrangle inequality smoothing, but this has not yet turned out to be fruitful. For haptic ligands, an additional feasibility criterion is applied: MOLASSEMBLER estimates the conical space the site occupies and removes stereopermutations in which the conical spaces of multiple haptic binding sites overlap.

A stereopermutator with multiple feasible stereopermutations may be left unspecified: Although a set of feasible stereopermutations might exist, stereopermutators can be set as none of them. In other terms, their assigned stereopermutation is nullo. When unspecified, stereopermutators represent all of their possible stereopermutations. For example, a conformational ensemble generated from a compound with a single asymmetric, tetrahedral, and unspecified stereopermutator represents a racemic mixture of both configurations.

In summary, MOLASSEMBLER executes the following steps to identify stereopermutations from coordinates: First, it ranks the central atom's graph adjacents and groups the substituents into sites. Second, it combines substituent ranking and binding site groups into a site ranking. Third, it classifies the local shape (see next

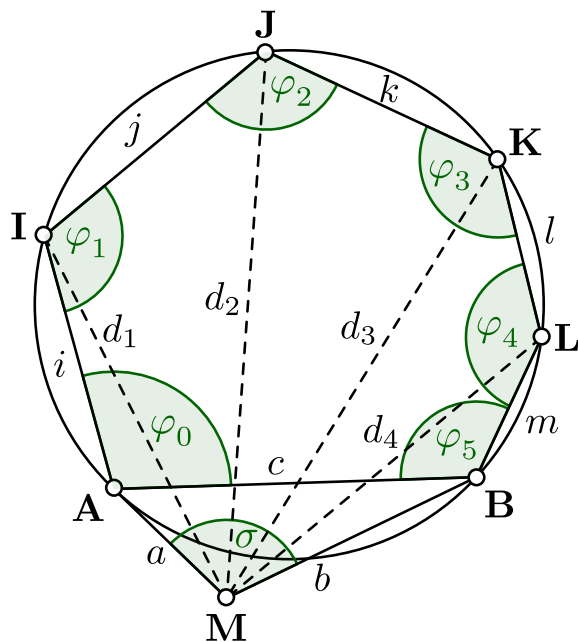


Figure 4: Geometric construction for determining the viability of an arbitrary bidentate cycle. The spatial distances between atoms are modeled on the basis of their element type and mutual bond orders. The idealized angle between immediate adjacents of the central atom **M** is known in the given stereopermutation. The resulting distance between atoms **A** and **B** is the closing edge to the polygon defined by the cycle path between **A** and **B** excluding the central atom (labeled i through m). This uniquely determines the cyclic polygon. From these quantities, the upper bound on the distances d_i between members of the cycle and the central atom can be calculated. If, for any of the cycle members, the upper bound on the distance to the central atom is lower than a modeled distance in case they were bonded, then the stereopermutation will be considered unfeasible since any spatial realization will contradict the graph.

section). Fourth, MOLASSEMBLER enumerates abstract permutations and removes permutations deemed unfeasible. Finally, it identifies the stereopermutation present by finding the realized stereopermutation within the set of permutations deemed feasible.

4 Shape information from Cartesian coordinates

To extract which particular stereopermutation is present at a non-terminal atom in a molecular structure, local shapes must first be classified starting from Cartesian coordinates. This is achieved by calculating the continuous shape measures²⁷ of all

shapes with a number of vertices matching the number of binding sites and choosing the shape for which the continuous shape measure is minimal. The calculation of continuous shape measures is principally of factorial complexity since the point-pairwise mapping minimizing the measure is unknown. A faithful implementation of the suggested algorithm is prohibitively expensive for shapes with many vertices, particularly because the shape centroid must also be considered. The problem is not without exploitable structure, however: Although a faithful implementation prescribes minimizing both relative orientation and scaling over all point pairings, minimization over scaling can be relegated to after the minimal pairing regarding relative orientation is found, hence reducing the complexity of evaluating a single pairing. If the shape features rotational symmetries, these can be exploited to avoid redundant pairings. This divides the theoretical complexity by the shape’s number of superimposable rotations. A larger reduction in complexity is reached by the application of the following heuristic: The spatial rotation is considered converged with only a reduced, fixed number of point pairings. After performing a rotational minimization of square distances by a quaternion fit with limited pairings, the cost of adding individual pairings to the current set is calculated for all remaining pairs and the minimal variation is chosen without recalculating the spatial rotation with intermediate choices. This heuristic can fail if multiple points lie within a small spherical area, implying the rotation matrix is not converged by few point pairs. This failure mode is both detectable and unlikely to occur in molecular structures. The resulting complexity in terms of quaternion fits scales as $\mathcal{O}(N!/(N - D)!)$ where N is the number of vertices of the shape including the centroid and D is the number of point pairings for which the rotation is considered converged. MOLASSEMBLER applies $D = 5$ and pre-sets the centroid point pair known from stereopermutator shape fitting. We made further algorithmic attempts at finding the minimal pairing permutation at reduced cost with simulated annealing, stochastic tunneling,²⁸ thermodynamic simulated annealing,²⁹ fixed-cost greedy, and locally optimal minimizations with reshuffling, all without bearing fruit against the heuristic described above with respect to correctness and speed.

Initially, shapes were recognized through minimizing the sum of absolute angular deviations between binding site centroids of the coordinates from the idealized geometry. Although it is difficult to objectively evaluate the agreement between shape classification algorithms and human perception, it can be plainly stated that shape classification through angular deviations alone quickly breaks subjective tests. Geometry indices as defined for limited sets of shapes with four^{30,31} and five³² vertices can improve angular deviation classification, but are limited in applicability: MOLASSEMBLER contains more shapes with four vertices than the geometry index can classify. For example, the trigonal pyramid, here denoting an axially monovacant trigonal bipyramid, not a monovacant tetrahedron, is not considered in the value

range definition of the geometry index τ_4 . Hence, the geometry index is only applied to exclude that shape for which its value indicates the largest distance. Overall, both the pure angular deviation and its hybrid with geometry indices are fast and effective, but do not match visual intuition for strongly distorted structures.

Another shape classification algorithm that we considered was the continuous symmetry measure,³³ which measures the degree to which a set of points has a particular point group symmetry. Unfortunately, this is untenable as a matching point group symmetry does not demonstrate similarity to a particular polyhedral shape. If, for instance, a viable shape in classification were the equatorially monovacant trigonal bipyramid (also known as disphenoid or seesaw) of C_{2v} point group symmetry, a collinear arrangement of all points would minimize the continuous symmetry measure. Another thought experiment demonstrates a further weakness: Imagine one wants to classify a shape of four vertices, and the set of possible shapes includes the square and the equatorially monovacant trigonal bipyramid, which have D_{4h} and C_{2v} point group symmetries, respectively. The C_{2v} point group is a subgroup of the D_{4h} point group. A regular square has continuous symmetry measures $S(D_{4h}) = 0$ and $S(C_{2v}) = 0$, highlighting the ambiguity of polyhedral shape matching to point group symmetry.

In the context of continuous shape measures, the concept of minimum distortion paths were introduced between distinct shapes.³⁴ Another, in hindsight fruitless, shape classification algorithm studied was based on calculating the distance of the shape to be classified from the paths separating all pairs of viable shapes. That pair for which the distance from the path was minimal was chosen and then the smaller shape measure of that shape pair was the classified shape. However, this is a poor shape classification algorithm, indicated by a strong disconnect between its classification choices and visual intuition beginning at slight distortions.

In an attempt to quantify and visualize the behavior of experimental shape classification algorithms, we compared their results on a uniform random distortion scale. In this attempt, the base shape to be re-identified was distorted by addition of fixed-length distortions of uniform random direction to each vertex including the centroid and the resulting point cloud reclassified as a shape. For a sense of scale of distortion vector norms relative to the shape size, recall that MOLASSEMBLER encompasses only spherical shapes whose vertices are at unit distance from the coordinate origin, where the centroid is placed. From a reductionistic perspective disregarding the distinct relationships between particular shapes, an algorithm that reclassifies shapes correctly for larger distortion vector norms could be considered better. We shall argue with this metric by distinguishing algorithms with restricted or extensive *distortion tolerance*.

A comparison of shape classification algorithms at the example of the tetrahedron is visualized in Figure 5 (cf. also the subsequent two figures discussed below). For each algorithm, the idealized shape in a unit sphere is uniformly distorted one-hundred times by applying vectors of uniform random direction at each vertex point. Then, the one-hundred distorted point clouds are reclassified as shapes. This is repeated for increasing distortion vector norms.

In Figure 5, the pure angular deviation algorithm shows extensive distortion tolerance, but the continuous symmetry measure based algorithm misclassifies an undistorted tetrahedron into the C_{3v} symmetry of the trigonal pyramid and classifies all distorted tetrahedra as closer to C_{2v} or C_{3v} point groups than the T_d point group. The continuous shape measure has a much reduced distortion tolerance, but classifies structures into more diverse shapes at large distortions than the angular deviation algorithm. The minimum distortion path deviation continuous shape measure algorithm has even further reduced distortion tolerance than the pure continuous shape measure algorithm and over-represents the trigonal pyramid at the expense of the seesaw, which is classified only once. In this example, the discussed shortcomings of algorithms based on the continuous symmetry measure or minimum distortion path deviation continuous shape measure become clear.

We now compare some shape classification algorithms at the example of multiple shapes. For all shapes with four vertices encompassed in MOLASSEMBLER, shape classification with angular distortion and its hybrid with geometry indices are compared by the aforementioned metric in Figure 6. It is noticeable that the trigonal pyramid (more specifically an axially monovacant trigonal bipyramid), despite being a rare occurrence when compared to the tetrahedron or the square, is overrepresented compared to a random shape distribution. The addition of geometry indices as an exclusion criterion exacerbates this, presumably because the trigonal pyramid is never excluded by geometry index, whereas all other shapes are. Generally, both variations of the angular distortion algorithm have good distortion tolerance. Merely the square shape dissipates quickly in the hybrid algorithm. Note that this is not necessarily bad as we have introduced distortion tolerance as a measure that does not consider the relationships between shapes, but solely as a means to compare algorithms.

Lastly, consider the continuous shape measure based algorithm and a biased variation in Figure 7. For all shapes except the tetrahedron, the unbiased algorithm exhibits good distortion tolerance characteristics, and the set of classified shapes at large distortions is consistently diverse when compared to the angular distortion algorithm. The seesaw and trigonal pyramid shapes, which are equatorially or axially monovacant trigonal bipyramids, are comparatively rare structures relative to the tetrahedron or square. The biased variation reweights continuous shape measures

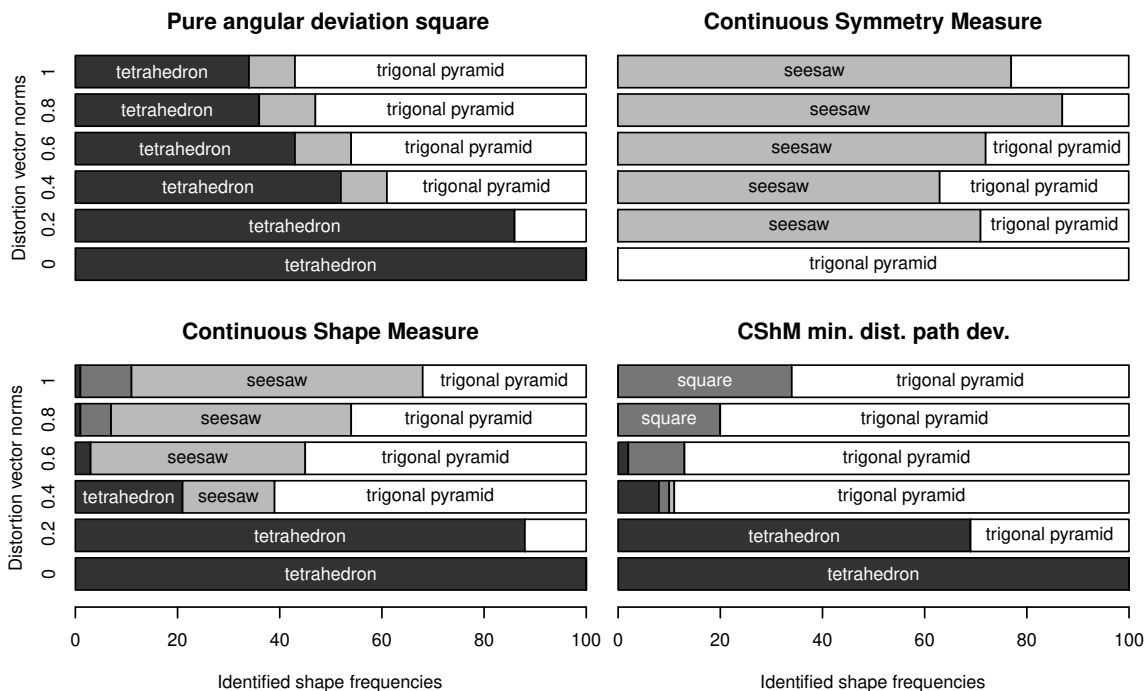


Figure 5: Shape classifications of four algorithms with varying distortion vector norms applied to all vertices of a regular tetrahedron. From left to right, top to bottom: Minimal sum of angular deviation square, minimal continuous symmetry measure, minimal continuous shape measure, and continuous shape measure (CShM) minimum distortion path deviation algorithms. 'Frequencies' denotes the occurrence of a shape in the set of one-hundred distorted structures generated.

of seesaw and trigonal bipyramids to reduce their classification probability. As a result, the algorithm exhibits extensive distortion tolerance for the tetrahedron and square shapes and reduced distortion tolerance for the seesaw and trigonal pyramid shapes. This biased algorithm is the shape classification algorithm chosen for MOLASSEMBLER.

Returning to the identification of a stereopermutation from Cartesian coordinates: By calculating the continuous shape measure in order to classify the shape, one also obtains a minimal square distance pairwise mapping between shape vertices and binding site centroids. This allows for direct mapping into the realized stereopermutation, which can then be sought in a generated set of feasible stereopermutations.

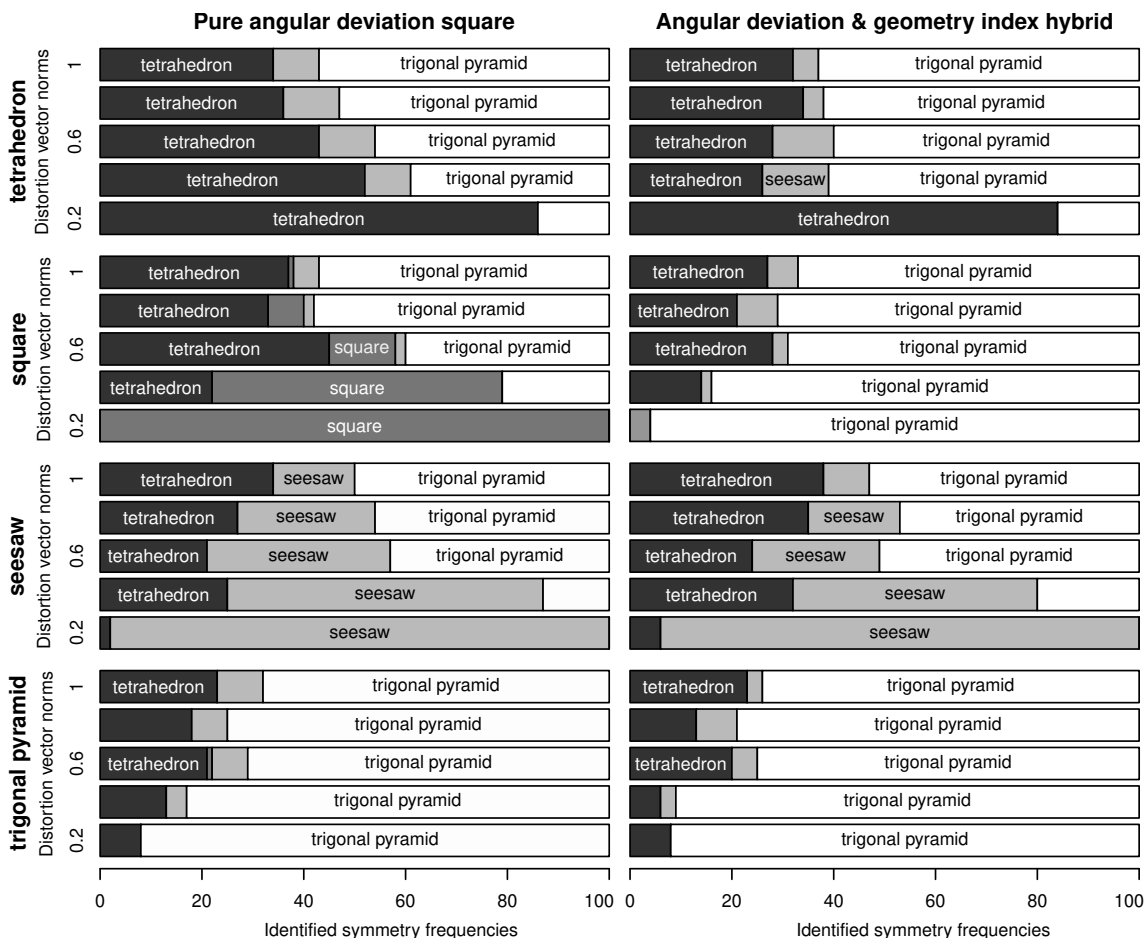


Figure 6: Shapes identified by sum of angular deviation squares algorithm (left column) and its hybrid algorithm with geometry indices (right column) for four-vertex shapes with varying distortion vector norms applied to all vertices. Classification of the base undistorted shape is not shown as both algorithms correctly identify it. 'Frequencies' denotes the occurrence of a shape in the set of one-hundred distorted structures generated.

5 Atom-centered stereopermutators

Instead of IUPAC stereodescriptors such as *R* and *S* for the two stereopermutations of an asymmetric tetrahedron, MOLASSEMBLER exposes two indices of permutation that serve as transferable and comparable stereodescriptors under different conditions. The first is the index of permutation within the abstract permutational space disregarding feasibility. This integer stereodescriptor is transferable among equivalent abstract inputs: If the number of different binding sites (as determined by ranking), their linking, and the local shape match between cases, the index of permutation will be comparable. The second is the index of an abstract stereoper-

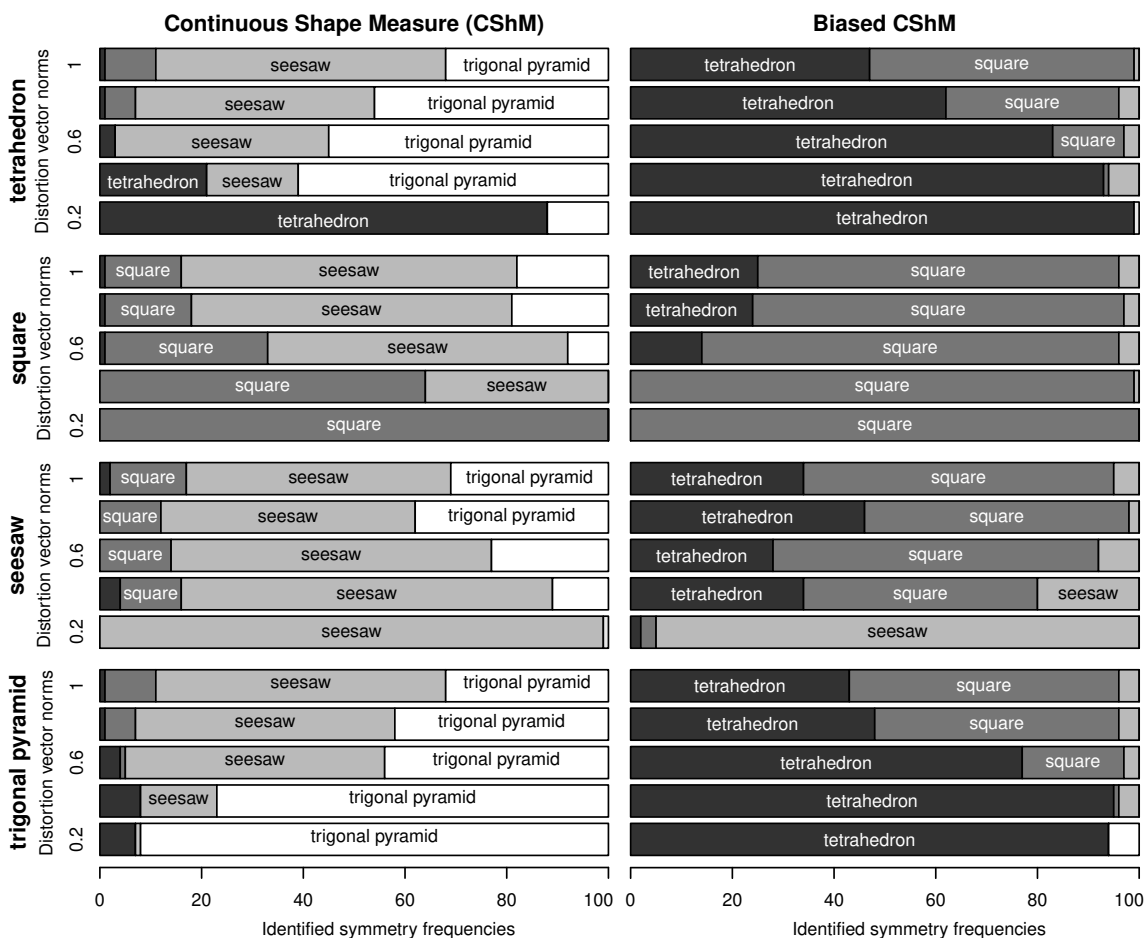


Figure 7: Shapes identified by the continuous shape measure algorithm (left column) and a biased variant algorithm (right column) for four-vertex shapes with varying distortion vector norms applied to all vertices. Classification of the base undistorted shape is not shown as both algorithms correctly identify it. 'Frequencies' denotes the occurrence of a shape in the set of one-hundred distorted structures generated.

mutation within an ordered list of stereopermutations deemed feasible, which will be comparable only if all previous conditions hold and all linking cycles are composed of matching element types and bond orders. Note that the value range of the second stereodescriptor can change upon changes to the algorithm determining feasibility.

The idealization of orientations into local shapes enables the enumeration of stereopermutations in an abstract space. However, two issues arise: Most importantly, distorted geometries present challenges for shape classification and conformer generation. It can be difficult to recognize the correct shape in strongly distorted structures. Special care must be taken not to misinterpret distortions owing to, e.g., small cycles in terms of a false shape, and tolerances on internal coordinates must be expanded in spatial modeling if distortions are necessary to form a con-

formation. This problem is discussed further in Section 9. Second, as the list of local shapes is bounded, the particular local shape one might require to adequately describe a molecular configuration may not be in the available set. However, the list of available shapes is designed to be extensible with little effort to alleviate such problems.

The applied model of spatial orientations around a central atom cannot intrinsically distinguish in which combinations of atoms and shapes stereopermutations can interconvert with low energy barriers (consider, for example, inversion at a nitrogen atom). In essence, the current model treats molecular configuration as rigid, a situation considered to be realized classically at zero Kelvin. Though optional, a thawing protocol is invoked by default in which a stereopermutator managing a nitrogen atom in a monovacant tetrahedral local shape with three different binding sites will be a stereocenter only if it is a member of a cycle of size three or four.³⁵ Without this protocol, any monovacant tetrahedral nitrogen atom with three different binding sites is a stereocenter. If none of the ligands are linked in a trigonal or pentagonal bipyramid, axial and equatorial ligands interchange at room temperature through Berry pseudorotation³⁶ and the Bartell mechanism,³⁷ respectively. MOLASSEMBLER will therefore 'thermalize' stereopermutations in such shapes in the thawing approximation if none of the binding sites are linked, reducing such shapes' chiral character.

In spite of an abstract model of orientation, molecules are modifiable in close analogy to three-dimensional editing. If an atom and its immediate surroundings constitute a stereocenter and its stereopermutation is known, then under specific circumstances, adding or removing a binding site will not cause loss of information. In two situations, chiral state loss is the correct result. First, if the resulting set of binding sites post-edit cannot constitute a stereocenter in the target shape. Second, binding site addition can be ambiguous; from a square shape to a square pyramid shape, the new apical position can be either above or below the plane of existing shape vertices. By default, the algorithm opts to discard chiral state on ambiguous transitions or on significant total angular or chiral deviations of shape vertices. Alternatively, one can choose to retain chiral state if the transition is unique, or to let MOLASSEMBLER choose at random from the best transitions. The set of best transitions between shapes of adjacent sizes is partially computed at compile-time with certain compilers in order to avoid runtime costs. Transitions are calculated instead of hard-coded to keep the list of local shapes easily extensible.

Atom-centered stereopermutator propagation encompasses substituent count changes, site count changes, ranking order changes, and shape changes, any combination of which may occur simultaneously. To limit implementation complexity, propagation is limited to shape size, site, and substituent count changes of at most one. Un-

der these circumstances, a mapping between sites can be generated on the basis of constituting substituent set similarity quantified by an edit distance metric in analogy to string edit distance metrics like Levenshtein distance.³⁸ If the shape is changed, a mapping of shape vertices between shapes is chosen in accordance with propagation settings. Propagation then proceeds in four steps: First, site indices are placed at the old shape vertices with the stereopermutator’s set stereopermutation. Second, if a shape vertex mapping exists, the old site indices will be transferred into the new shape. Third, old site indices are mapped to new site indices with the site index mapping. From the new site indices placed at the shape vertices of the new shape, a stereopermutation is generated that can then be sought in the set of new stereopermutations. If the stereopermutation cannot be propagated and the stereopermutator in its new shape and ranking is a stereocenter, it will be left undetermined. The propagation practiced here has distinct parallels to the transformations in reaction rules of Andersen et al.,³⁹ particularly with respect to shape vertex propagation.

6 Bond-centered stereopermutators

In contrast to atom-centered stereopermutators that capture non-superimposable orientations of the immediate graph adjacents of a single atom, bond-centered stereopermutators capture non-superimposable relative orientations of a bond’s substituents that arise due to hindered rotation around the bond axis; consider, e.g., substituents bonded to the atoms of a non-rotatable double bond (see Figure 8), where for each atom there exists also an atom-centered stereopermutator characterizing the local shape. Bond-centered stereopermutators are generalized to arbitrary combinations of shapes instead of being specialized toward the common combinations among and between equilateral triangles and bent shapes that constitute most rotational barriers along double bonds.

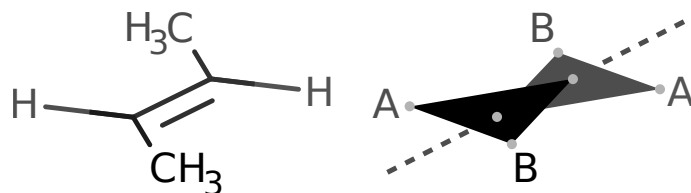


Figure 8: *Left:* Lewis structure of (E)-but-2-ene. *Right:* Abstract classification of the double-bond motif of (E)-but-2-ene into two triangle shapes and the substituents’ ranking cases. Light gray circles denote shape vertex loci.

Stereodescriptors derived from a procedure enumerating all possible rotational orientations must be comparable and transferable among equivalent situations. Con-

sequently, inputs to the stereopermutation enumeration algorithm are standardized and abstracted. Each side of the bond is reduced to its local shape, the fused shape vertex within that shape (i.e., the vertex that is part of the bond), and the ranking characters of all non-fused vertices, as shown in Fig. 8.

The stereopermutators at each end of the bond carry the information required for the abstraction: The ranking of their binding sites permits the abstraction to ranking characters, and the specified stereopermutation places ranking characters at shape vertices.

There exist degrees of freedom in the data representation of the input to the stereopermutation enumeration algorithm. Any shape vertex may be fused into a bond. Additionally, shape vertex enumeration is arbitrary. These degrees of freedom can be removed by rotating the fused vertex to the algebraically smallest shape vertex of its set of rotationally interconvertible vertices. For example, the octahedron has a single set of interconvertible vertices, but the square pyramid has two: The equatorial set of four vertices, and the singleton set containing the apical vertex. Removing representational degrees of freedom ensures the stereopermutation enumeration algorithm generates transferable stereodescriptors.

The enumeration scheme proceeds to identify the set of closest off-axis shape vertices that will be most relevant to rotational energy barriers. If, at either side of the bond, this shape vertex set's ranking characters are all equivalent, then rotation around the bond is isotropic. Next, dihedral orientations are generated by sequentially aligning off-axis shape vertices across both sets. Alignment of off-axis shape vertices does not need to be eclipsic, but can also be staggered, enabling bond-centered stereopermutators to also enumerate hypothesized rotational minimum-energy structures in e.g. alkanes.

This scheme will omit the trans-alignment in a combination of two bent shapes, however, so it is explicitly added. Furthermore, the emergent ordering of stereopermutations does not yield stereodescriptors paralleling the relative order of the IUPAC stereodescriptors *E/Z* as defined in the sequence rules. To ease the implementation of a ranking algorithm, the stereopermutation sequence is modified to match the relative order of IUPAC stereodescriptors.

Bond-centered stereopermutators can be placed at any bond where both constituting atoms are managed by a stereopermutator whose stereopermutation is specified. Unspecified atom-centered stereopermutators cannot form the basis of a bond-centered stereopermutator because their mapping from binding sites to shape vertices is unknown. Constituting shapes are not limited to the common cases constituting multiple-order bonds in organic chemistry. The rotational energy structure of wild combinations of shapes with many vertices is likely to be more complex than MO-

LASSEMBLER would suggest, however.

Analogously to atom-centered stereopermutators, bond-centered stereopermutations may not be viable in small rings. For instance, altering the orientation of the double bond in cyclopentene to an *E* orientation yields an unembeddable graph, and this bond should therefore not be considered for bond-centered stereopermutation. Unfeasible bond-centered stereopermutations can be identified in analogy to unfeasible links in atom-centered stereopermutators.

In atom-centered stereopermutator feasibility, one segment of the cyclic polygon is the segment *c* that replaces the 1–3 distance modeled explicitly by two atomic distances and one angle in Figure 4. In bond-centered stereopermutator feasibility, this segment is the replacement of the 1–4 distance, which is explicitly modeled via three atomic distances, two angles, and one dihedral angle. Another difference is that the cyclic polygon expansion plane must be modeled in three dimensions (see Supporting Information). In a sequence of four atoms at a dihedral angle of zero, the cyclic polygon expands within the same plane as the dihedral-constituting atoms to maximize atomic distances from cycle atoms to dihedral-angle-constituting atoms. At dihedral angle π , the expansion plane maximizing cycle-atom distances to the dihedral-angle base atoms lies perpendicular to that of the dihedral-angle-constituting atoms, as shown in Figure 9.

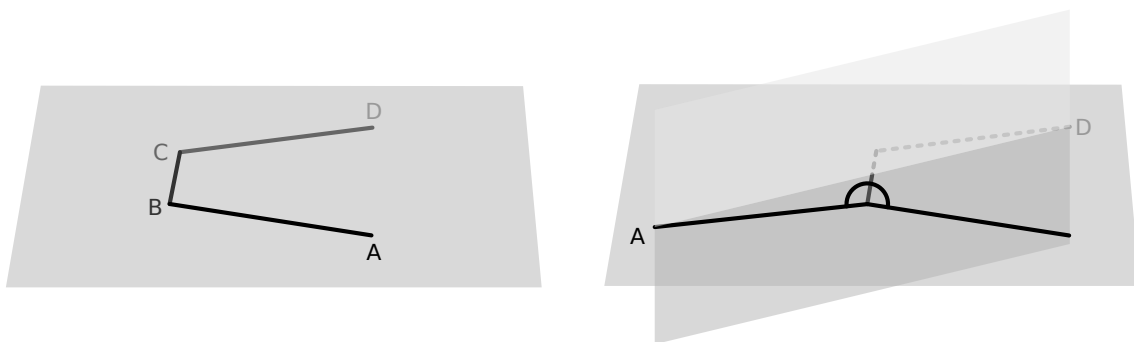


Figure 9: *Left:* A dihedral sequence *ABCD* composed of segments of unit length and joined at $\frac{2\pi}{3}$ angles with dihedral angle zero. The plane in which the cyclic polygon expands coincides with the plane composed of the points *BCD* as this offers points on the cycle the maximal distance to the base vertices *BC*. *Right:* The same dihedral sequence at dihedral angle π . The cyclic polygon now expands in a plane perpendicular to that of *BCD*.

Local modeling of bond-centered stereopermutator feasibility by cyclic polygons has a necessarily limited purview. Consider a graph cycle of arbitrary length containing two bond-centered stereopermutators each composed of two atom-centered stereopermutators of equilateral triangle shape. Each bond-centered stereopermutator permits a cis and trans arrangement of the cycle continuation. At small cycle sizes,

individual feasibility modeling detects that only a cis arrangement is possible and argue that neither bond-centered stereopermutator is stereogenic. At large cycle sizes, both arrangements are deemed feasible. It is conceivable that a cycle size exists in which only one bond-centered stereopermutator can be cis at a time for the graph to be embeddable. Individual bond-centered stereopermutator feasibility modeling will not capture this.

In carbocycles of size seven and below, bond stereopermutators are not stereogenic, yet they do serve to enforce planarity of their substituents in conformers. During molecule construction, if a cycle is detected as approximately flat, bond-centered stereopermutators are placed at all edges of the cycle, enforcing coplanarity of all cycle edges.

As chiral state propagation of bond-centered stereopermutators on alterations of underlying atom-centered stereopermutators apart from ranking changes has not been implemented, alterations of atom-centered stereopermutators forming a bond-centered stereopermutator cause the bond-centered stereopermutator to be dropped.

7 Ranking algorithm

Ranking is based on the IUPAC sequence rules for organic molecules.¹⁸ The rules for organic molecules form a starting point for the differentiation of ligands that is generalizable to MOLASSEMBLER’s model of stereocenters. Without the ambition to generate canonical IUPAC names for molecules of either organic or inorganic character, there is no need to implement further rules and relative preferences were laid out for inorganic molecules in Ref. 40. Differences to organic-molecule ranking arise mainly from generalization of the sequence rules from organic stereodescriptors to the library model and from partial omissions of sequence rules due to missing implementations. The stereodescriptors *R* and *S* arising from maximally asymmetric tetrahedral centers directly correspond to indices of permutation arising from the atom-centered permutational scheme. The stereodescriptors *Z/seqCis* and *E/seqTrans* similarly correspond to indices of permutation arising from the bond-centered stereopermutation scheme. Note that helical chirality stereodescriptors *M* and *P* are currently not detected by MOLASSEMBLER.

The following changes and omissions were made with respect to the IUPAC sequence rules: First, no algorithm to enumerate mesomeric Kekulé structures is currently implemented, so the relevant part of sequence rule 1a in Ref. 18 is discarded. This omission is planned to be fixed in a future version of our software. Second, no distinction will be made between asymmetric and pseudoasymmetric stereogenic units,

affecting sequence rules 4a and 4c. Third, MOLASSEMBLER considers stereopermutators alike for sequence rule 4b if the number of stereopermutations and the index of permutation match. This is merely an abstraction of the sequence rule that covers all explicit cases laid out in the sequence rule definition. Lastly, the relative priority of stereodescriptors *R* before *S* and *Z* before *E* defined in sequence rule 5 is abstracted to algebraic ordering of the index of permutation. Inherently, since the vertex enumeration of shapes is arbitrary, the relative order of indices of permutation is also arbitrary. We can therefore choose the vertex enumeration at the tetrahedron and monovacant tetrahedron so that the integer ordering parallels the order of the corresponding *R* and *S* stereodescriptors.

The generation of indices of permutation at bond-centered stereopermutators is similarly altered to parallel the IUPAC stereodescriptors *E/seqCis* and *Z/seqTrans*. Indices of permutation for shapes with more vertices than the tetrahedron can distinctly depend on the abstract binding case. For instance, indices of permutation for a trigonal bipyramid of abstract binding case **ABCDE** are not comparable to indices of permutation for the abstract binding case **AABCD**. Furthermore, they are not comparable across different shapes. Consequently, relative ordering of stereodescriptors in sequence rule 5 is established by sequential comparison of the shape (algebraic ordering of its index in the list of all shapes), lexicographic comparison of the abstract binding case, and finally comparison of the index of permutation. The relative ordering established remains arbitrary, but the sequence rule distinguishes more cases that may occur in inorganic compounds without affecting the relative priority of the organic stereodescriptors.

A ranking algorithm based upon these modified IUPAC sequence rules can establish chemical differences between individual atom substituents, but not between binding sites. For a ranking at the level of binding sites, MOLASSEMBLER applies two sequence rules. First, sites consisting of more atoms precede sites consisting of fewer atoms. Second, sites are ordered lexicographically by their constituting atoms' ranking positions set. The ranking positions set is ordered descending by value.

Ranking implementation correctness was tested against relevant IUPAC examples¹⁸ and a validation suite from a proposed revision of the sequence rules.⁴¹ Not surprisingly, owing to the implementation of only a limited set of sequence rules and some omissions from their definitions (as discussed above), MOLASSEMBLER did not pass all tests from this validation suite. However, additional differences arose due to different interpretations of the sequence rules. The consequence of an incorrect ranking can be twofold. By falsely differentiating substituents, duplicate stereopermutations can arise that are superimposable. By falsely equating substituents, stereopermutations can be missed. These issues point to future work on the implementation, which will lift limitations imposed upon sequence rules so that sequence

rule interpretation can be brought into full agreement with that of the validation set.

Currently, the generalization of the sequence rules to MOLASSEMBLER’s molecule model resulted in a ranking algorithm that can be applied in myriad situations. Stereodescriptors of multidentate and haptic ligands in arbitrary polyhedral shapes and stereodescriptors of any multiple bond-order combination of polyhedral shapes at any fused vertices are accounted for. Despite its incompleteness, the ranking algorithm as implemented is correct for a vast majority of typical cases.

8 Molecule representation, equivalence, and manipulation

A set of atom (nuclear) Cartesian coordinates is in principle free of any information about the presence of bonds between atoms. MOLASSEMBLER allows the translation of molecules given as a set of nuclear coordinates and a bond order matrix into graphs. This proceeds by discretization of the bond order matrix, subsequent connected component identification, and finally classification of local shapes and identification of stereopermutations of a specific molecule.

Crucial for the correct molecule interpretation is that bonds are identified correctly. A vast number of methods may be applied to calculate bond orders for systems under study. Generally, we do not recommend a particular method that will always work for any kind of system, simply because of the fact that the assignment of chemical bonds will be affected by subjective ratings in regions where bond orders are not close to an integer number. Instead, we chose not to integrate any particular scheme into the process, requiring a floating-point bond order matrix as input instead. Additionally, MOLASSEMBLER explicitly supports two variants of bond order discretizations. The first mode interprets bonds between atoms according to a bond order matrix in a binary fashion: Bonds either exist or they do not exist, and no differentiation is made regarding their order, (with the exception of ‘eta’ bonds). Little detail in modeling of molecules is lost in this mode because bond stereopermutators are checked in a phenomenological fashion: If a dihedral angle is aligned in eclipsed fashion, it is assumed that there is an energetic reason for it. Similarly, flat cycles are detected and preserved by bond stereopermutators, ensuring at least a structural capture of aromaticity. Generally, this method of molecule interpretation is robust and can be combined with low-effort bond order calculation methods such as the comparison of atom-pair spatial distances against sums of covalent radii. The other mode of discretization of the floating-point bond order matrix is rounding into

the nearest integer bond order. Bond stereopermutators can be checked either at all bonds or only at those bonds above a specified real-number bond order threshold to reduce the likelihood that a spuriously eclipsed dihedral angle is misconstrued as an energetically favorable effect. Recall that MOLASSEMBLER expects structures at a local potential energy surface minimum as input. Methods yielding floating-point bond orders suitable for discretization in this mode may be system-appropriate force fields or quantum mechanical methods, possibly with Natural Bond Order 42 or Intrinsic Bond Order 43 approaches. The generated conformational ensembles of molecules interpreted by binary bond discretization are generally poorer in quality than those of the nearest-integer approach, because atom-pair distances are then universally estimated as if they were of order one, losing fidelity from their input. Note, however, that MOLASSEMBLER does not aim to generate conformational ensembles of thermodynamic quality. A generated conformer merely has to be close enough to a local potential energy surface minimum so that subsequent refinement by an appropriate method (e.g., quantum chemical structure optimization) leads into the intended minimum, and this property is preserved. By supporting both manners of bond order discretization, MOLASSEMBLER allows a trade-off between reliability of interpretation against fidelity of modeling and quality of generated conformational ensembles if the system under study imposes it. In future work, a possible extension of the bond discretization procedure may attempt to maximize the number of low-distortion recognized local shapes either to correct the discretization itself or serve to highlight problematic cases.

Small manipulations of molecules, as trivial as they may seem, impose a significant amount of nontrivial work. Stereodescriptors are propagated at binding site additions and removals to the target shape as discussed above. Since stereodescriptors are chosen based on substituent ranking, which may have been altered by the edit, it is necessary to re-rank all binding sites of non-terminal atoms. For an example see Figure 10. Should a binding site ranking change by the edit, assigned stereopermutations are propagated to the new ranking. Consequently, to ensure continuity, molecule edits scale at least linearly in the number of atoms.

In large-scale manipulations of molecules such as connecting multiple molecules we may avoid increasing complexity by delaying chiral state propagations due to ranking changes until all graph modifications are finished. Hence, specialized functions for large-scale manipulations such as connects, disconnects, substitutions, and chelating ligand additions are made available in our software.

Equivalence between two molecules is based on a colored graph isomorphism algorithm with modular vertex coloring so that molecules can be compared for varying definitions of molecular equality. The information that can be exploited to color vertices are element types, bond orders, local shapes, and stereopermutations. To

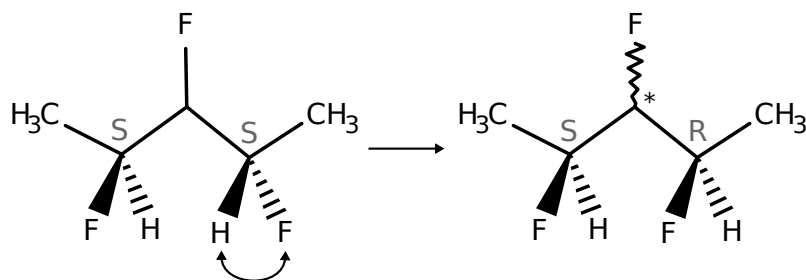


Figure 10: *Left*: This example shows a molecule with two substituents at the central carbon atom that are constitutionally isomeric and carry the same stereodescriptor, yielding an identical ranking. The central carbon atom is not stereogenic. If a molecule edit changes the stereopermutation of one of these substituents, akin to swapping the hydrogen and fluorine atom as indicated, the stereodescriptor flips. *Right*: The desired result of the molecular manipulation. Although the change is local to the right arm of the molecule, it incurs a differentiation between the two arms at the central carbon atom, which is stereogenic and unspecified after re-ranking.

expedite molecular-graph comparisons in large sets, it is helpful to standardize all involved graphs. If both graphs in a comparison are in canonical form, it is no longer necessary to search for an index permutation matching vertices across the graphs; instead, it is possible to base comparisons on an identity vertex mapping. Such canonicalization is modular, as is the colored graph isomorphism. If two molecular graphs have been brought into standardized form with the same level of information as the comparison is tasked with, equivalence comparison of molecule instances is a direct identity mapping comparison instead of a colored graph isomorphism.

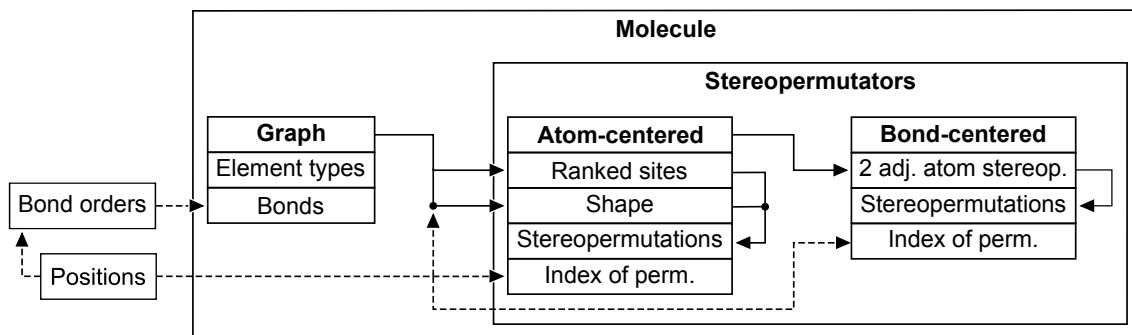


Figure 11: Simplified data flow in construction of a molecule representation from various primitive data types. Solid paths represent the default flow of data, dashed paths represent optional data flow. For instance, by default, the local shape of non-terminal atoms is inferred from the graph in the construction of atom-centered stereopermutators. Optionally and preferably, if positions are available, local shapes can be classified from atom (nuclear) positions.

The components of the molecule model and some of their dependencies are illus-

trated in Figure 11. Nuclear Cartesian coordinates and bond orders are optional primitive data types in the construction of a molecule. Minimally, a molecule representation consists of a graph storing element types and bonds. Atom-centered stereopermutators are constructed at non-terminal atoms of the graph from a ranking of its substituents and a local shape either inferred from the graph or classified from coordinates. These parts are combined into the set of stereopermutations. Two adjacent atom-centered stereopermutators can form the foundation of a bond-centered stereopermutator, which determines its stereopermutations from the information embedded in both atom-centered stereopermutators. The indices of permutation of both atom-centered and bond-centered stereopermutators can be inferred from positions.

Worth mentioning are a number of further available features: (i) Molecule instances are serializable into plain-text JavaScript Object Notation and its binary encodings for database or file storage. (ii) It is possible to assert whether molecules are enantiomers of one another. (iii) McGregor’s maximum common subgraph algorithm⁴⁴ with custom vertex comparators enables subgraph matching. (iv) MOLASSEMBLER also contains an openSMILES⁴⁵ compliant SMILES parser notably implementing stereoconfiguration for square, trigonal bipyramid and octahedron shapes in addition to the tetrahedron.

9 Conformer generation

Conformer generation in MOLASSEMBLER is achieved with Distance Geometry.⁴⁶ In the context of molecular conformer generation, Distance Geometry enables a multi-step transformation from an atom-pairwise distance bounds matrix to atom coordinates. A distance bounds matrix is filled with lower and upper bounds on atom-pair distances as desired in the resulting conformer.

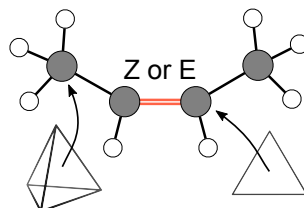
Conformer generation proceeds in three major steps (refer to Figure 12): The first stage is preparatory, where we exclude some graphs that cannot be modeled and assign unspecified stereopermutators. Second is spatial modeling, where the molecular model is translated into a distance bounds matrix. In the third step, we apply Distance Geometry and obtain Cartesian atom coordinates.

It is necessary for spatial modeling that all stereopermutators of a molecule must have at least one feasible stereopermutation and may not be unspecified. In the first preparatory stage, unspecified stereopermutators are set iteratively by choosing a random unspecified stereopermutator and setting its stereopermutation at random until no unspecified stereopermutators remain. For atom-centered stereopermuta-

```
import scine_mol assembler as masm
mol = masm.io.experimental.from_smiles("CC=CC")
conf = masm.dg.generate_random_conformation(mol)
```

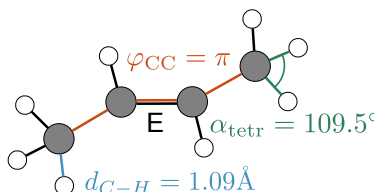
1. Input preparation

- Asserts no unfeasible stereopermutators
- Assigns unspecified stereopermutators



2. Spatial modeling

- Generates distance bounds of ensemble
- Bond distances from graph
- Angles from atom-stereopermutators
- Dihedrals from bond-stereopermutators



3. Distance Geometry

- Chooses distance matrix
- Embeds metric matrix
- Refines coordinates against error function
- Checks optimization result against bounds

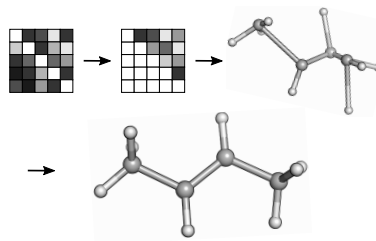


Figure 12: Condensed steps of the conformer generation procedure at the example of but-2-ene with an unspecified bond stereopermutator at the double bond. Input to conformer generation is a modelled molecule. After the unspecified bond stereopermutator is randomly assigned, spatial modelling proceeds by generating a distance bounds matrix. This distance bounds matrix is then finally converted into spatial coordinates by Distance Geometry.

tors, each stereopermutation is weighted by its relative statistical occurrence.

In the spatial modeling stage, we leverage the molecular model to collect atom-pairwise distance bounds for a distance bounds matrix. Distance bounds are estimated between all pairs of atoms up to a graph distance of three. The distance bounds of immediate graph adjacents are populated from estimations of atom distances for the given bond order. Each atom-centered stereopermutator provides angular information between its substituents, which allows the modeling of the distance bounds of 1–3 bonded atoms when combined with 1–2 distance bounds. Each bond-centered stereopermutator provides dihedral information between substituents, which allows the modeling of the distance bounds of 1–4 bonded atoms

when combined with 1–2 distance bounds and the angular information of the two atom-centered stereopermutators constituting the bond. If no bond-centered stereopermutator is present on a bond, default full definition range dihedral bounds are assumed instead in the modeling of the 1–4 bonded distance.

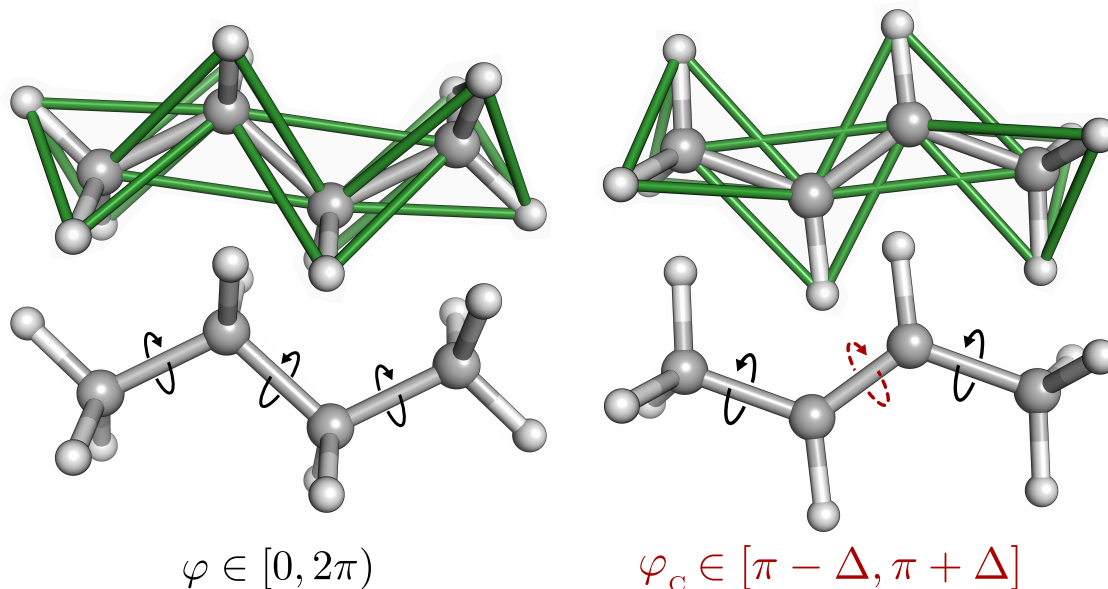


Figure 13: Representations of the molecular model of butane (left) and but-2E-ene (right) and differences in conformer generation spatial modeling. While butane has an atom-centered stereopermutator at each carbon atom indicating a local tetrahedral shape, the central two atom stereopermutators of but-2E-ene indicate a local equilateral-triangle shape. When modeling butane, all dihedrals along the carbon atoms are freely rotatable. In contrast, but-2E-ene has a bond-centered stereopermutator placed at the central carbon bond whose assigned stereopermutation matching the stereodescriptor 'E' restricts e.g. the carbon dihedral angle to a range of width Δ centered around the trans-dihedral angle.

For example, a butane molecule will have atom-centered stereopermutators placed at each carbon atom indicating the local shape of a tetrahedron, as shown in Figure 13. All dihedral angles are freely rotatable as no bond-centered stereopermutators are present. In contrast, atom-centered stereopermutators of but-2-ene at the double bond indicate the local shape of an equilateral triangle. The single bond-centered stereopermutator placed at the double bond indicates whether a *Z*- or *E*-ethene substructure is modeled by its assigned stereopermutation. The distance bounds among the atoms adjacent to the double bond are affected by the selected bond stereopermutation.

Spatial modeling modifies the collected bounds to encompass distorted structures. Angle bounds of local shapes are expanded if they are a member of a cycle with

fewer than six members. Angles between substituents of spirocenters with small cycles are explicitly modeled. It is possible to specify fixed positions for atoms, albeit with the condition that none, one or all of its binding sites' atom positions must be fixed as well.

Having obtained a distance bounds matrix from spatial modeling, we proceed with the final stage, the application of Distance Geometry. A distance matrix is generated by triangle inequality bounds smoothing the distance bounds matrix and iteratively choosing pairwise distances between the resulting bounds. To avoid $O(N^5)$ complexity for full metrization, the triangle inequality smoothing problem is transferred to a shortest-path graph problem.⁴⁷ The resulting single-source shortest-path problem on a graph with negative edge weights is solved by the simplified GOR1 algorithm⁴⁸ as it performs well on such graphs. MOLASSEMBLER implements three metrization⁴⁹ variants: Full metrization, 10% metrization, and four-atom metrization.

The distance matrix is then transformed into the metric matrix and embedded into Cartesian coordinate space. These coordinates typically poorly reflect their distance bound inputs and require optimization against an error function. Such error functions typically contain two types of terms: Distance errors mediating particle pair distances, and chiral errors mediating four-particle relative orientation by a signed tetrahedron volume, similar to an improper dihedral.

In refinement, distance bound violation error terms can prevent the tetrahedron volume spanned by a chiral constraint from inverting. The more chiral constraints occur, the more problematic this becomes, in particular if chiral constraints have overlapping particle domains. The more vertices the local shape of an atom-centered stereopermutator has, the more chiral constraints are emitted to ensure capture of its chirality, exacerbating the problem. To ensure proper inversion of incorrectly embedded chiral constraints, we adopted multiple-stage four spatial coordinates refinement: Distance errors are applied on four spatial coordinates while chiral errors are applied on three. In the first stage of refinement, the structure is free to expand into the fourth spatial dimension to minimize chiral errors. When all chiral constraints have the correct sign, an additional potential is applied on the fourth spatial dimension to compress structures back into three dimensional space.

The refinement error function in our implementation features two further changes: Bond-centered stereopermutators emit dihedral bounds and hence the refinement error function contains dihedral error terms. In contrast to enforcing zero-dihedral angle orientations of four particles with chiral constraints of zero volume, dihedral error terms offer more flexibility in the specificity of refined structures. Additionally, for haptic ligands, in which the centroids of the set of vertices forming the binding site occupy a shape vertex, chiral and dihedral errors are calculated with centroids

of particle sets instead of with positions of individual particles.

The refinement error function depends on a set of N particles with positions \vec{r}_i . The symmetric matrices \mathbf{L} and \mathbf{U} contain the lower and upper distance bounds. Each chiral constraint of the set C consists of four particle sets $S_\alpha, S_\beta, S_\gamma, S_\delta$, and a lower and an upper signed volume bound L_V and U_V , respectively. Each dihedral constraint of the set D consists of four particle sets, a lower and an upper signed dihedral bound L_ϕ and U_ϕ , respectively.

The signed tetrahedron volume of a chiral constraint is calculated from the centroids of its constituting particle sets \vec{s}_j as:

$$\vec{s}_j = \frac{1}{|S_j|} \sum_{i=1}^{|S_j|} \vec{r}_{S_j,i} \quad (1)$$

$$V_{\alpha\beta\gamma\delta} = \frac{1}{6} (\vec{s}_\alpha - \vec{s}_\delta)^T \cdot [(\vec{s}_\beta - \vec{s}_\delta) \times (\vec{s}_\gamma - \vec{s}_\delta)]. \quad (2)$$

The distance error d_{ij} , the chiral error $C_{\alpha\beta\gamma\delta}$, and the dihedral error $D_{\alpha\beta\gamma\delta}$ are defined as:

$$d_{ij} = \max^2 \left(0, \frac{(\vec{r}_j - \vec{r}_i)^2}{U_{ij}^2} - 1 \right) + \max^2 \left(0, \frac{2L_{ij}^2}{L_{ij}^2 + (\vec{r}_j - \vec{r}_i)^2} - 1 \right) \quad (3)$$

$$C_{\alpha\beta\gamma\delta} = \max^2(0, V_{\alpha\beta\gamma\delta} - U_V) + \max^2(0, L_V - V_{\alpha\beta\gamma\delta}) \quad (4)$$

$$D_{\alpha\beta\gamma\delta} = \max^2 \left(0, \left| \phi_{\alpha\beta\gamma\delta} + \begin{cases} 2\pi & \phi < \frac{U_\phi + L_\phi - 2\pi}{2} \\ 0 & \phi > \frac{U_\phi + L_\phi + 2\pi}{2} \end{cases} - \frac{U_\phi + L_\phi}{2} \right| - \frac{U_\phi - L_\phi}{2} \right) \quad (5)$$

where \max^2 denotes the operation 'square the largest element out of the two given in parenthesis'. The total error function then reads

$$\text{erf}(\{\vec{r}_i\}) = \sum_{i < j}^N d_{ij} + \sum_{(S_\alpha, S_\beta, S_\gamma, S_\delta, U_V, L_V) \in C} C_{\alpha\beta\gamma\delta} + \sum_{(S_\alpha, S_\beta, S_\gamma, S_\delta, U_\phi, L_\phi) \in D} D_{\alpha\beta\gamma\delta} \quad (6)$$

(note the doubled letter 'r' introduced in the abbreviation of the function to distinguish it from the standard error function). The error function erf is minimized with analytical gradients by L-BFGS⁵⁰ in three stages: First, without application of a potential on the fourth spatial dimension and dihedral errors, the tetrahedra modeled

by chiral errors are allowed to invert. Second, a potential is applied to the fourth dimension and components along the fourth spatial dimension are eliminated. Lastly, dihedral errors are enabled. Conformer generation can then be trivially parallelized.

Directed conformer generation has been implemented by placing bond stereopermutators enumerating staggered arrangements at bonds whose rotations are non-isotropic. MOLASSEMBLER implements a trie data structure to track and ease generation of rotational combinations among the set of staggered bond stereopermutators. These combinations can then be passed to a special conformer generation function. Until feasibility criteria for combinations of dihedral arrangements in cycles are devised and implemented, bonds in cycles of any size are excluded from consideration in directed conformer generation, however.

10 Shortcomings

As mentioned before, the general model of stereopermutators treats molecular configuration as frozen with the exceptions of (i) nitrogen atom inversion, (ii) the Berry pseudorotation, and (iii) the Bartell mechanism, for all of which the thawing of stereopermutations has been implemented as an option. Most likely, these are not the only cases in which stereopermutations can easily interconvert. In all unhandled cases, MOLASSEMBLER may overstate chiral character.

Feasibility determination of stereopermutations involving haptic binding sites based on conical-space overlap avoidance is limited by the algorithm estimating the required conical space. This algorithm currently estimates the required conical space for biatomic or cyclic topologies; apart from this, no feasibility checks are made. The potential consequences are overstatements of chiral character and failures to generate conformations.

Our effort to ensure that modeled conformers are close to local minima of the potential energy hypersurface is still rather limited and improved structure prediction can be envisioned for future improvement of our software. In the present version, atom pair distances in discrete bond orders are simply estimated by Universal Force Field⁵¹ parameters. Systematic distortions of common local shapes such as those due to Jahn-Teller distortion⁵² in an octahedron have not been addressed. It is therefore inadvisable to directly analyze generated conformational ensembles without subjecting the generated structures to suitable structure optimization or molecular mechanics methods.

The fundamentally factorial complexity of shape recognition and stereopermutation enumeration will limit the applicability of MOLASSEMBLER for compounds with

very high coordination numbers. Additionally, for such compounds, the approach of classifying shapes into a strict set of defined shapes may be impractical. The Thomson Potential²² demonstrates effectively that the more point charges are introduced, the more local minima the potential surface exhibits. Similarly, the set of shapes with numerous vertices would have to expand significantly to correctly capture various exotic shapes and point group symmetries. In particular for many vertices, it might be preferable to cut shape classification from the library entirely and instead try to identify rotational symmetry elements that the stereopermutation algorithm could apply directly.

MOLASSEMBLER does not pass the validation test set proposed by Hanson et. al.⁴¹ The library ranking algorithm predates their work, which laid bare the possibility of alternate interpretations of the existing sequence rules. The validation set also includes test cases for a proposed additional sequence rule which is not implemented in MOLASSEMBLER. In future work, the library ranking algorithm will be brought into closer alignment with their proposed changes. A ranking algorithm capable of exact differentiation is of paramount importance as stereogenicity of atom centers may be misrepresented. Furthermore, no axial or helical chirality is yet identified by our implementation and certain molecular features may be missed.

11 Demonstration examples

MOLASSEMBLER has already been employed in the context of automated exploration of chemical reaction networks,⁵³ in which it served as molecular graph interpreter, equivalence oracle, and conformer generator. Therefore, we begin with a demonstration of two of its core features:

We shall consider an example where feasibility checks are important: An octahedral center with three short-bridge bidentate ligands. For the abstract binding case $(A-A)_3$, there are four stereopermutations, as shown in Figure 14. In the particular case of $[Fe(\mu^2-Oxalate)_3]^{3+}$, the feasibility algorithm rules out all stereopermutations in which an oxalate is trans-arranged due to its short bridges. MOLASSEMBLER reports that the stereopermutator has four stereopermutations but only two of these are feasible.

Next, we demonstrate that the abstraction MOLASSEMBLER introduces regarding binding sites is effective for haptic ligands. In Figure 15, an example molecule is shown with a relatively complex case for shape classification, ranking, and stereopermutation – all at once. The assumption that the centroid of a set of contiguous binding atoms is placed at a vertex of an underlying shape is well-applicable here,

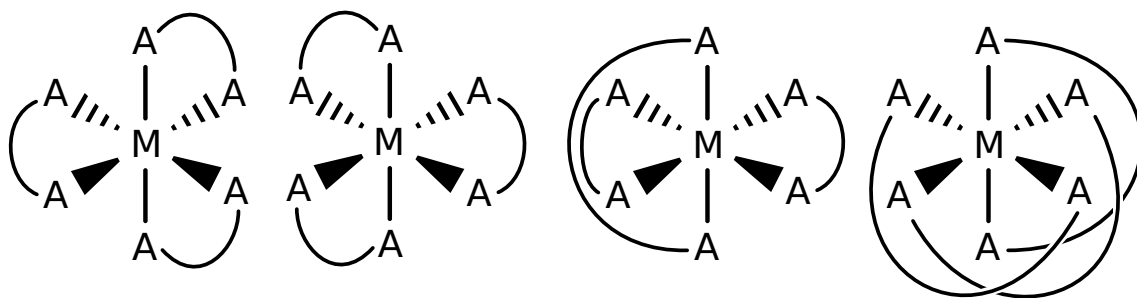


Figure 14: The four abstract stereopermutations of the binding case $(A-A)_3$ in an octahedron, from left to right: The Λ and Δ isomers, in which all bidentate ligands are cis-arranged, a stereopermutation in which a single ligand is trans-arranged, and lastly a stereopermutation in which all ligands are trans-arranged.

reducing the five-atom copper atom to a three-site equilateral triangle. Ranking correctly deduces that its haptic ligands are identical in an $(A-A)B$ abstract binding case. Similarly, the twelve-atom titanium atom is reduced to a four-site tetrahedron with a $(A-A)(B-B)$ binding case. Stereopermutation concludes that neither center is stereogenic.

In order to show that MOLASSEMBLER can accurately capture stereochemistry, we have interpreted the full set of compounds collected by Proppe and Reiher,⁵⁴ which comprises 44 iron compounds with diverse bonding patterns, into the presented molecular model. Some selected examples are shown in Figure 16 and the full compound set is arrayed in Figures S2–S9. This is a significant stress test since the test set contains a varied set of coordination polyhedra, some with significant distortions. In our judgment, only in the case of compound #26 (displayed bottom right in Figure 16) is the shape classification result dubious: A trigonal bipyramid is classified instead of a square pyramid. Apart from generating molecular models, we have also generated conformers of stereoisomers for a selected compound to exhibit more of the program interface. For further details, see the Supporting Information.

12 Conclusions

The molecular model applied in MOLASSEMBLER is capable of accurately representing many inorganic molecular complexes. The data representation of stereoisomerism generalizes to complex shapes and ligands, permitting an abstract high-level approach to molecular structure. Transferable stereodescriptors are devised for any combination of shape and abstract binding case, including haptic and multidentate ligands. Molecule instances are interpretable from Cartesian coordinates, constructible from various cheminformatics formats, editable, canonicalizeable, se-

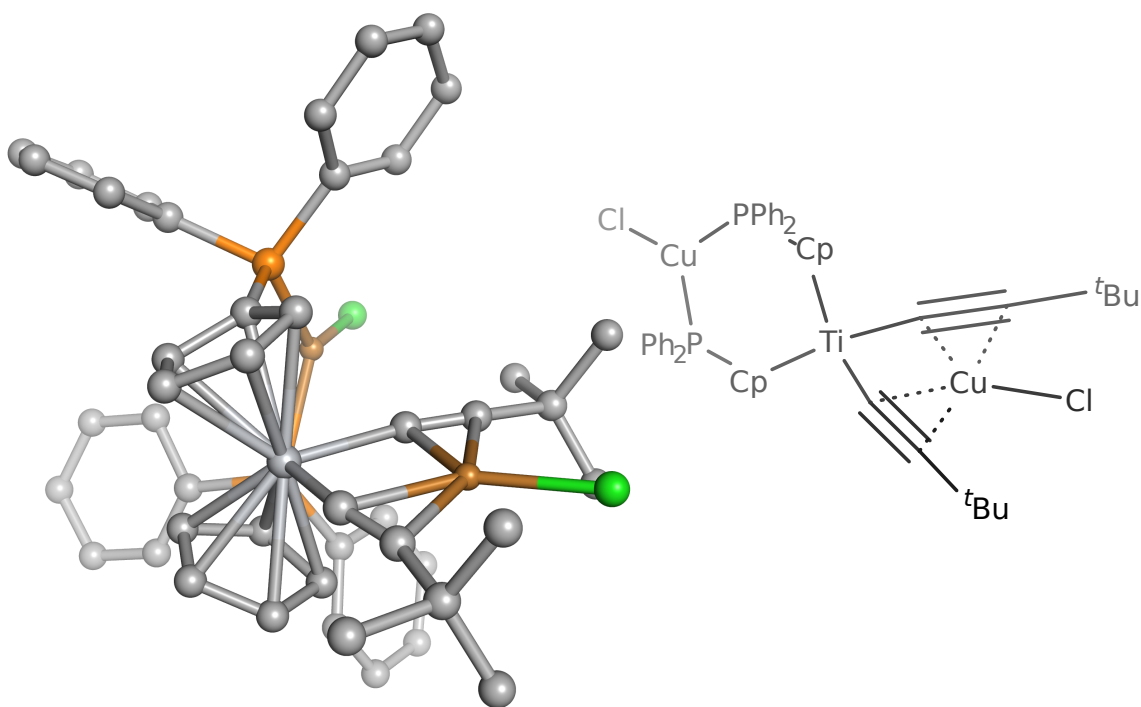


Figure 15: *Left*: The heavy-atom skeleton of a molecule with two types of haptic ligands: The bridged cyclopentadienyl groups bonded to a titanium atom in the center, and the triple bonds bonded to the copper atom towards the right. *Right*: Simplified Lewis structure of the left compound. Atom coloring: Carbon and titanium in gray, phosphorus in orange, copper in brown, and chlorine in green.

realizable, and comparable. Both stochastic and directed conformer generation are implemented. Despite the few shortcomings in its first version, MOLASSEMBLER is already a feature-rich, general-purpose program that enables programs to expand into parts of organometallic and inorganic chemical space. In future releases, we will address the existing shortcomings, particularly with regard to ranking and handling of aromaticity. MOLASSEMBLER is open-source under the BSD 3-clause license and available in the SCINE project.⁵⁵

Acknowledgments

This work has been financially supported by ETH Zürich (ETH-38 17-1).

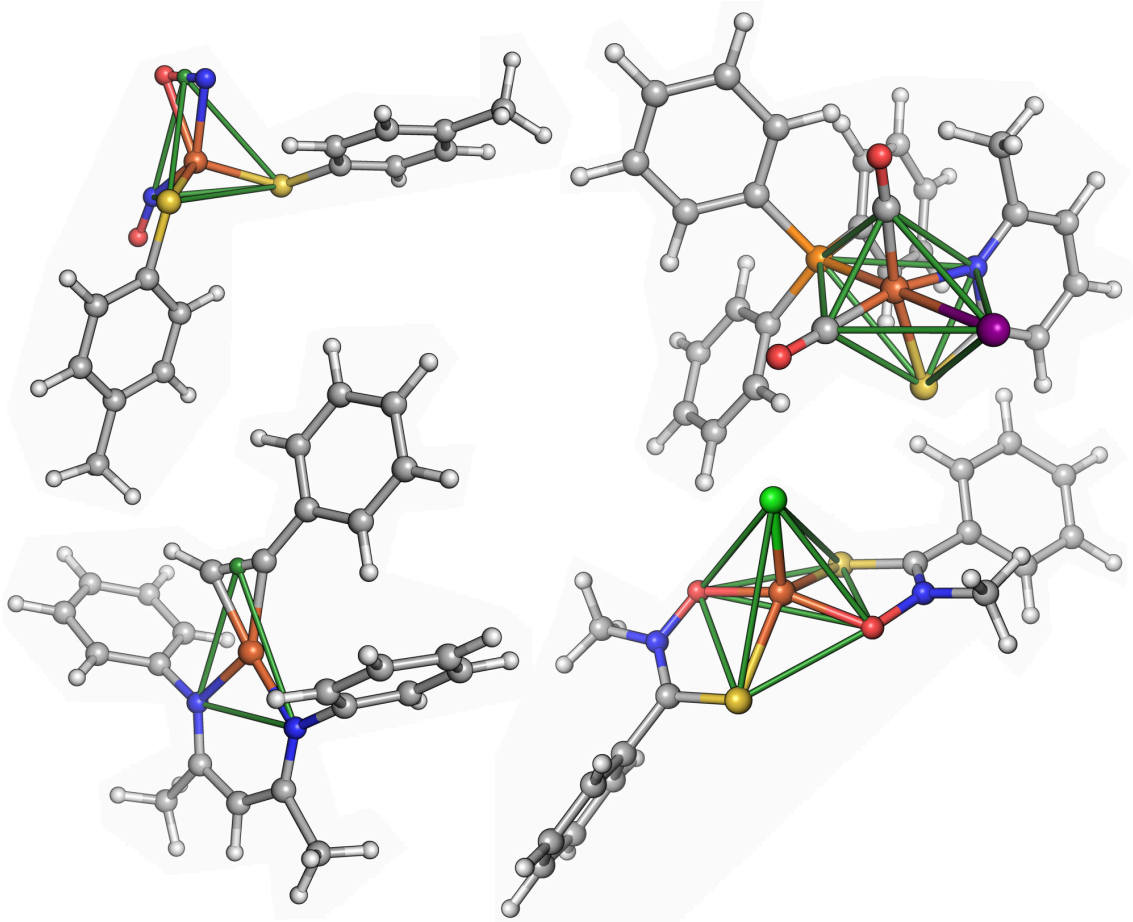


Figure 16: Clockwise from top left: Compounds #28, #34, #26, and #14 from the dataset of Ref.,⁵⁴ with the interpreted polyhedral shape of iron atoms highlighted in green.

A Library architecture and dependencies

MOLASSEMBLER is a C++ library written in the C++14 language standard. It has multiple dependencies: The SCINE Utilities⁵⁵ form the data exchange formats prevalent throughout our software. Linear algebra computations are mediated by the Eigen⁵⁶ library. RingDecomposerLib^{25,57} provides graph cycle perception with a chemical perspective, nauty⁵⁸ serves graph canonicalization purposes, JSON for Modern C++⁵⁹ offers serialization and deserialization to JavaScript Object Notation (JSON), and several Boost libraries^{60–68,68–73} form the basis of the molecular graph representation and offer relevant algorithms and data structures.

Optional dependencies offer functionality if available: If one wishes to compile the available Python bindings, the C++ library pybind11⁷⁴ will be required. Parallelization of core library algorithms will be available if OpenMP⁷⁵ is supported by the

available compiler and linker. MOLASSEMBLER will accept SMILES⁷⁶ and InChI⁷⁷ input if OpenBabel's⁷⁸ chemical file format conversion utility is found at runtime.

Configuration of optional components, compiler-agnostic building and installation are supported cross-platform by modern CMake scripts.

MOLASSEMBLER draws from two sub-libraries, each serving singular purposes. One is responsible for defining the local shapes and calculating properties and transition mappings between them. The other is responsible for the symbolic permutation required in stereopermutation. Further sub-libraries model cyclic polygons, implement the simplified GOR1 shortest path algorithm for Boost Graph Library data structures, and provide data structures and algorithms for compile-time computation. The main body of MOLASSEMBLER itself is split into the application programming interface and the private implementations thereof. Overall, MOLASSEMBLER consists of roughly sixty thousand lines of code and twenty thousand lines of comments and documentation. With the open-source release we provide an installation and user's manual as well as separate technical documentations for the C++ library and the Python module (see <https://scine.ethz.ch/download/molassembler>).

B Supporting Information

B.1 Shape classification algorithms

Algorithms to classify point clouds into idealized polyhedral shapes that we investigated for our purposes are listed in Table 1.

Table 1: List of shape classification algorithms

Name	Listing	Reference
Continuous shape measure	1	27
Continuous shape measure with heuristics	2	
Continuous shape measure minimum distortion path deviation	3	34
Continuous symmetry measure	4, 5	33
Angular square deviation	6	
Angular deviation and geometry index hybrid	7	30,31

Note, however, that several algorithms in this table refer to undefined functions. These are briefly explained in the accompanying text. All algorithms listed here have been implemented in MOLASSEMBLER. For further details, we refer to the source code and its accompanying documentation.

B.1.1 Continuous shape measure-derived algorithms

The continuous shape measure calculation is presented in Alg. 1. For each possible mapping of the N vertices of the point cloud to the vertices of the reference polyhedron, this algorithm involves separate minimizations over a rotation matrix and an isotropic scaling parameter. The minimization over the rotation matrix is here explicitly carried out by a quaternion fit, but is in principle open to other optimization methods. There are three undefined functions in this listing. `Coordinates` yields the idealized coordinates of its shape parameter. The function `Shapes` returns the set of all shapes with a number of vertices equal to its integer parameter. Finally, the `VertexCount` function returns the number of vertices of a shape. In brief, this algorithm classifies a point cloud as that shape of matching number of vertices for which the continuous shape measure is minimal.

A number of heuristics can be added, of which the authors themselves suggest several, such as pre-pairing vertices. Our benchmarks indicate that the quaternion fit is the most time intensive step within the loop. We chose several changes, presented in Alg. 2. For one, we performed the minimization over isotropic scaling only on

Algorithm 1 Continuous shape measure

```
1: function NORMALIZE( $\mathbf{R}$ ) ▷  $\mathbf{R}$  is  $N$  Cartesian coordinates  $\vec{r}_i$ 
2:    $\bar{r} = \frac{1}{N} \sum_i^N \vec{r}_i$  ▷  $\bar{r}$  centroid
3:    $\mathbf{S} \leftarrow \mathbf{R} - \bar{r}$ 
4:    $l \leftarrow 0$ 
5:   for all  $\vec{s}_i \in \mathbf{S}$  do
6:      $l \leftarrow \max(l, |\vec{s}_i|)$ 
7:   end for
8:   return  $\frac{1}{l} \cdot \mathbf{S}$  ▷ Rescale so largest vector is unit length
9: end function
10:
11: function SHAPEMEASURE( $\mathbf{P}, s$ ) ▷  $\mathbf{P}$  is  $N$  Cartesian coordinates,  $s$  a shape
12:   require  $N = \text{VERTEXCOUNT}(s)$ 
13:    $\mathbf{C} \leftarrow \text{NORMALIZE}(\mathbf{P})$  ▷ Point cloud coordinates
14:    $\mathbf{S} \leftarrow \text{COORDINATES}(s)$  ▷ Idealized shape coordinates
15:    $s_{\min} \leftarrow \infty$  ▷ Minimal shape measure
16:   for all  $\sigma \in \text{PERMUTATIONS}(N)$  do
17:      $\mathbf{S}_\sigma \leftarrow \sigma \mathbf{S}$  ▷ Apply permutation
18:      $\mathbf{R} \leftarrow \text{QUATERNIONFIT}(\mathbf{C}, \mathbf{S}_\sigma)$ 
19:      $\mathbf{S}_R \leftarrow \mathbf{R} \mathbf{S}_\sigma$  ▷ Apply rotation
20:      $s \leftarrow \min_a \sum_i^N |\vec{c}_i - a \vec{s}_{R,i}|^2$  ▷ Minimize over isotropic scaling
21:      $s_{\min} \leftarrow \min(s_{\min}, s)$ 
22:   end for
23:   return  $100 \cdot s_{\min} \div \sum_i^N |\vec{c}_i|^2$  ▷ Normalized shape measure
24: end function
25:
26: function CLASSIFYSHAPEBYCSHM( $\mathbf{P}$ )
27:   return  $\underset{s \in \text{SHAPES}(N)}{\text{argmin}} \text{SHAPEMEASURE}(\mathbf{P}, s)$ 
28: end function
```

Algorithm 2 Continuous shape measure, with heuristics

```
1: function SHAPEMEASUREHEURISTICS( $\mathbf{P}, s$ ) ▷ As in Alg. 1
2:   require  $N = \text{VERTEXCOUNT}(s)$ 
3:    $\mathbf{C} \leftarrow \text{NORMALIZE}(\mathbf{P})$  ▷ Point cloud coordinates
4:    $\mathbf{S} \leftarrow \text{COORDINATES}(s)$  ▷ Idealized shape coordinates
5:    $s_{\min} \leftarrow \infty$  ▷ Minimal shape measure
6:    $\sigma_{\min} \leftarrow \emptyset$ 
7:   for all  $i \neq j \neq k \neq l \neq m \mid \{i, j, k, l, m\} \in \{1, 2, \dots, N\}$  do
8:      $\sigma_p \leftarrow \begin{pmatrix} 1 & 2 & 3 & 4 & 5 \\ i & j & k & l & m \end{pmatrix}$  ▷ Partial point mapping from  $\mathbf{C}$  to  $\mathbf{S}$ 
9:      $\mathbf{R} \leftarrow \text{PARTIALQUATERNIONFIT}(\mathbf{C}, \mathbf{S}, \sigma_p)$ 
10:     $\mathbf{S}_p \leftarrow \mathbf{R}\mathbf{S}$ 
11:     $s_p \leftarrow \sum_i^5 |\vec{c}_i - \vec{s}_{p, \sigma_p(i)}|^2$ 
12:    if  $s_p > s_{\min}$  then ▷ Partial fit penalty greater than best?
13:      continue ▷ Skip this permutation
14:    end if
15:     $U \leftarrow \{6, 7, \dots, N\}$  ▷ Points of  $\mathbf{C}$  not mapped by  $\sigma_p$ 
16:     $V \leftarrow \{1, 2, \dots, N\} \cap \sigma_p$  ▷ Points of  $\mathbf{S}$  not mapped by  $\sigma_p$ 
17:     $a_{i,j} \leftarrow |\vec{c}_{U_i} - \vec{s}_{p, V_j}|^2$  ▷ Cost matrix of adding a mapping
18:     $\sigma_{c, \min} \leftarrow \underset{\sigma_c}{\operatorname{argmin}} \sum_i^{N-5} a_{i, \sigma_c(i)} \mid \sigma_c \in \text{PERMUTATIONS}(N-5)$ 
19:     $\sigma \leftarrow \sigma_p \cup \begin{pmatrix} U_1 & U_2 & \dots & U_{N-5} \\ V_{\sigma_c(1)} & V_{\sigma_c(2)} & \dots & V_{\sigma_c(N-5)} \end{pmatrix}$  ▷ Merge cost min. perm.
20:     $\mathbf{R} \leftarrow \text{QUATERNIONFIT}(\mathbf{C}, \sigma\mathbf{S})$ 
21:     $\mathbf{S}_R \leftarrow \mathbf{R}\sigma\mathbf{S}$ 
22:     $s \leftarrow \sum_i^N |\vec{c}_i - \vec{s}_{R,i}|^2$ 
23:    if  $s < s_{\min}$  then
24:       $s_{\min} \leftarrow s$ 
25:       $\sigma_{\min} \leftarrow \sigma$ 
26:    end if
27:  end for
28:   $\mathbf{R} \leftarrow \text{QUATERNIONFIT}(\mathbf{C}, \sigma_{\min}\mathbf{S})$ 
29:   $\mathbf{S}_R \leftarrow \mathbf{R}\sigma_{\min}\mathbf{S}$  ▷ Apply rotation
30:   $s \leftarrow \min_a \sum_i^N |\vec{c}_i - a\vec{s}_{R,i}|^2$  ▷ Minimize over isotropic scaling
31:  return  $100 \cdot s \div \sum_i^N |\vec{c}_i|^2$  ▷ Normalized shape measure
32: end function
```

the best permutation, outside the main loop. Another change was that we consider quaternion fits converged after five vertex pairs have been mapped. For this partial mapping, a quaternion fit is performed. Afterwards a cost matrix is set up for all remaining possible vertex mappings, and the minimal cost permutation is merged with the initial five vertex pairs. Only then are a full quaternion fit performed and the square deviations calculated. Shape classification from a point cloud proceeds as before, except that the shape measure calculation algorithm is replaced with the presented `ShapeMeasureHeuristics` method.

Algorithm 3 Continuous shape measure minimum distortion path deviation

```

1: function PATHDEVIATION( $\mathbf{X}$ ,  $s_1$ ,  $s_2$ )      ▷  $\mathbf{X}$  is  $N$  Cart. coord.,  $s_i$  are shapes
2:    $\theta \leftarrow \arcsin \left( \sqrt{\text{SHAPEMEASURE}(\text{COORDINATES}(s_1), s_2)} \div 10 \right)$ 
3:    $C \leftarrow \text{NORMALIZE}(\mathbf{X})$ 
4:    $\alpha \leftarrow \arcsin \left( \sqrt{\text{SHAPEMEASURE}(C, s_1)} \div 10 \right)$ 
5:    $\beta \leftarrow \arcsin \left( \sqrt{\text{SHAPEMEASURE}(C, s_2)} \div 10 \right)$ 
6:   return  $(\alpha + \beta) \div (\theta - 1)$ 
7: end function
8:
9: function CLASSIFYSHAPEBYPATHDEV( $\mathbf{X}$ )      ▷  $\mathbf{X}$  is  $N$  Cart. coord.
10:   $p \leftarrow \underset{s_1 \neq s_2 \in \text{SHAPES}(N)}{\text{argmin}} \text{PATHDEVIATION}(\mathbf{X}, s_1, s_2)$       ▷  $p$  is a pair of shapes
11:  if  $\text{SHAPEMEASURE}(\mathbf{X}, p_1) < \text{SHAPEMEASURE}(\mathbf{X}, p_2)$  then
12:    return  $p_1$ 
13:  else
14:    return  $p_2$ 
15:  end if
16: end function

```

Lastly, the minimum distortion path deviation shape classification algorithm is based on the concept of minimum distortion paths between two shapes. It proceeds by calculating the distance of the point cloud from the minimum distortion path between all pairs of viable shapes. For the pair of shapes for which the distance from the distortion path is minimal, the shape with the lower shape measure is chosen.

B.1.2 Continuous symmetry measure

An algorithm for the calculation of the continuous symmetry measure is presented in Algs. 4 and 5. There are several undefined functions here. The function `PointGroup` returns the point group of its shape parameter. `Elements` returns the full set of symmetry elements of a point group. `Partition`, which accepts a set of symmetry

Algorithm 4 Continuous symmetry measure

```
1: function ELEMENTPARTITIONS( $S$ ) ▷  $S$  set of symmetry elements
2:    $G \leftarrow \emptyset$  ▷ Set of element partitions
3:    $P \leftarrow \emptyset$  ▷ Set of probe points
4:   procedure PROCESSPOINT( $\vec{p}$ )
5:     if  $\vec{p} \in P$  then
6:       return
7:     end if
8:      $G \leftarrow G \cup \text{PARTITION}(S, \vec{p})$  ▷ Partition  $S$  by result of application to  $\vec{p}$ 
9:      $P \leftarrow P \cup \vec{p}$ 
10:  end procedure
11:  PROCESSPOINT( $\vec{e}_z$ )
12:  PROCESSPOINT( $\vec{e}_z + \Delta \vec{e}_x$ ) ▷ With  $\Delta < 1$ 
13:  PROCESSPOINT( $\vec{e}_x$ )
14:  PROCESSPOINT( $\vec{e}_y$ )
15:  for all  $\vec{v} \in \{\text{AXIS}(\mathbf{E}) \mid \mathbf{E} \in S\}$  do ▷ AXIS yields unaltered line, if exists
16:    PROCESSPOINT( $\vec{v}$ )
17:  end for
18:  return  $P$ 
19: end function
20:
21: function CSM( $\mathbf{X}, P, E$ )
22:  require ( $|P| = |E|$ )  $\wedge \forall (|P_i| = |E_i|)$ 
23:   $M \leftarrow |P|$ 
24:   $N \leftarrow |P_1|$ 
25:   $v_{\min} \leftarrow \infty$ 
26:  for all  $\sigma \in \text{PERMUTATIONS}(M)$  do
27:     $\bar{x} \leftarrow \frac{1}{MN} \sum_i^M \sum_j^N \mathbf{E}_{i,j} \vec{x}_{\sigma(P_i)}$  ▷ Fold points by symmetry elements
28:     $v \leftarrow \sum_i |\mathbf{E}_{i,1}^{-1} \bar{x} - \vec{x}_{\sigma(P_i)}|^2$  ▷ Unfold and sum square difference norms
29:     $v_{\min} \leftarrow \min(v_{\min}, v)$ 
30:  end for
31:  return  $100 \cdot v_{\min} \div M$ 
32: end function
33: ▷ Continued in Alg. 5
```

Algorithm 5 Continuous symmetry measure (continued from Alg. 4)

```

34: function ALIGNEDSYMMETRYMEASURE( $\mathbf{X}, g$ )
35:    $E \leftarrow \text{ELEMENTS}(g)$ 
36:    $P \leftarrow \text{ELEMENTPARTITIONS}(E)$ 
37:    $a_k \leftarrow |P_k|$  ▷  $a_k$  coefficients of diophantine eq.
38:   if  $N > |E|$  then
39:      $a \leftarrow a \wedge |E|$  ▷ Extend coefficients by order of point group
40:      $P \leftarrow P \cup \{E\}$  ▷ Extend partitions by set of all elements
41:   end if
42:    $v_{\min} \leftarrow \infty$ 
43:   for all sequences  $x \mid \sum_i a_i x_i = N, \forall x_i \in \mathbb{N}_0$  do ▷ Solve diophantine
44:     for all partitions  $P_X$  of  $N$  points into  $x_i$  sets of size  $a_i$  do
45:        $v \leftarrow \frac{1}{|P_X|} \sum_i \text{CSM}(\mathbf{X}, P_{X,i}, P_i)$ 
46:       ▷  $P_i$  a partition of into sets of size equal to  $P_{X,i}$ 
47:        $v_{\min} \leftarrow \min(v_{\min}, v)$ 
48:     end for
49:   end for
50:   return  $v_{\min}$ 
51: end function
52:
53: function SYMMETRYMEASURE( $\mathbf{X}, g$ ) ▷  $\mathbf{X}$  is  $N$  Cart. coord.,  $g$  a point group
54:   return  $\min_{\mathbf{R} \in \text{SO}(3)} \text{ALIGNEDSYMMETRYMEASURE}(\mathbf{R}\mathbf{X})$ 
55: end function
56:
57: function CLASSIFYSHAPEBYCSM( $\mathbf{X}$ ) ▷  $\mathbf{X}$  is  $N$  Cartesian coordinates
58:    $\mathbf{C} \leftarrow \text{NORMALIZE}(\mathbf{X})$ 
59:   return  $\text{argmin}_{s \in \text{SHAPES}(N)} \text{SYMMETRYMEASURE}(\mathbf{C}, \text{POINTGROUP}(s))$ 
60: end function

```

elements and a vector, groups symmetry elements by identical results of applying the transformation matrix of the symmetry elements to the vector argument.

The continuous symmetry measure calculation implementation presented in Algs. 4 and 5 is admittedly clumsy. The minimization over all rotation matrices of a function, which is as costly to evaluate as `AlignedSymmetryMeasure`, is difficult to streamline. The algorithm presented here is noticeably more complex than the sketch laid out for the measure’s calculation from the original authors, because the sketch lays out the optimal path through a full algorithm. The additional complexities, such as exploring all possible solutions of the diophantine equation at 5.43 and all possible partitions of the N points according to the current solution of the diophantine immediately thereafter, are necessary. Perhaps the complexity they incur can be significantly reduced through application of heuristics. This is not explored here, however.

B.1.3 Angular deviation variations

Algorithm 6 Angular square deviation

```

1: function ANGULARDEVIATION( $\mathbf{X}$ ,  $s$ )
2:   return  $\min_{\sigma \in \text{ROTATIONS}(s)} \sum_{i < j} [\text{ANGLE}(\mathbf{X}, i, j) - \text{IDEALANGLE}(s, \sigma(i), \sigma(j))]^2$ 
3: end function
4:
5: function CLASSIFYSHAPEBYANGULARDEVIATION( $\mathbf{X}$ )  $\triangleright$   $\mathbf{X}$  is  $N$  Cart. coord.
6:    $\mathbf{C} \leftarrow \text{NORMALIZE}(\mathbf{X})$ 
7:   return  $\text{argmin}_{s \in \text{SHAPES}(N)} \text{ANGULARDEVIATION}(\mathbf{C}, s)$ 
8: end function

```

The pure angular deviation shape classification algorithm is based only on the central angles of vertices within their polyhedral shape. It requires knowing which vertex of the point cloud is the central vertex of the polyhedron since that is the base point with which the angles are calculated. The algorithm is shown in Alg. 6. The undefined functions are `Angle` and `IdealAngle`, the latter of which returns the angle between the vertices from the idealized coordinates of the shape.

Finally, the hybrid algorithm with geometry indices τ'_4 and τ_5 as shown in Alg. 7 leverages the geometry indices to exclude the most unlikely shapes according to their value range definitions.

Algorithm 7 Angular deviation and geometry index hybrid

```
1: function CLASSIFYSHAPEBYHYBRID(X)      ▷ X is  $N$  Cartesian coordinates
2:   C  $\leftarrow$  NORMALIZE(X)
3:   S  $\leftarrow$   $\emptyset$                                 ▷ Set of excluded shapes
4:   if  $N = 4$  then
5:      $\tau \leftarrow$  TAU4PRIME(C)
6:     if  $\tau < 0.12$  then
7:       S  $\leftarrow$  {Seesaw, Tetrahedron}
8:     else if  $0.12 \leq \tau < 0.62$  then
9:       S  $\leftarrow$  {Square, Tetrahedron}
10:    else if  $0.62 \leq \tau$  then
11:      S  $\leftarrow$  {Square, Seesaw}
12:    end if
13:  else if  $N = 5$  then
14:     $\tau \leftarrow$  TAU5(C)
15:    if  $\tau < 0.5$  then
16:      S  $\leftarrow$  {Trigonal bipyramid}
17:    else if  $\tau > 0.5$  then
18:      S  $\leftarrow$  {Square pyramid}
19:    end if
20:  end if
21:  V  $\leftarrow$  SHAPES( $N$ )  $\cap$  S                                ▷ Set of viable shapes
22:  return  $\underset{s \in V}{\operatorname{argmin}}$  ANGULARDEVIATION(C,  $s$ )
23: end function
```

B.2 Stereopermutations

B.2.1 Atom stereopermutation enumeration

An individual atom stereopermutation is represented as the product type of a sequence of ranking characters c_k and a set of ordered pairs L representing links between shape vertices. The sequence of ranking characters has length equal to the number of vertices of the shape and represents a mapping from a vertex position to a ranking character. Relational ordering of stereopermutations is defined via sequential lexicographical comparison of ranking characters and vertex links.

The enumeration of atom stereopermutations with tracking of relative statistical occurrence weights proceeds as laid out in Alg. 8. Note that a stereopermutation is represented as a tuple.

Algorithm 8 Atom stereopermutation enumeration

```
1: function APPLYPERMUTATION( $(c_k, L), \sigma$ ) ▷  $\sigma$  a permutation
2:   return  $(\sigma c_k, \{(\inf\{\sigma(l_1), \sigma(l_2)\}, \sup\{\sigma(l_1), \sigma(l_2)\}) \mid l \in L\})$ 
3: end function
4:
5: function ALLROTATIONS( $(c_k, L), s$ ) ▷  $s$  a shape
6:   return  $\{\text{APPLYPERMUTATION}((c_k, L), \sigma) \mid \sigma \in \text{ROTATIONS}(s)\}$ 
7: end function
8:
9: function ENUMERATE( $c_k, L, s$ ) ▷  $s$  a shape
10:   $u_1 \leftarrow \text{inf ALLROTATIONS}((c_k, L), s)$  ▷ Sequence of stereopermutations
11:   $v_1 \leftarrow 1$  ▷ Sequence of occurrence counts
12:  for all  $\sigma \in \text{PERMUTATIONS}(\text{VERTEXCOUNT}(s))$  do
13:     $r \leftarrow \text{inf ALLROTATIONS}(\text{APPLYPERMUTATION}((c_k, L), \sigma))$ 
14:    if  $r \in u_k$  then
15:       $i \leftarrow u_k^{-1}(r)$  ▷ Get index of  $r$  in sequence  $u$ 
16:       $v_i \leftarrow v_i + 1$  ▷ Increment occurrence count
17:    else
18:       $u \leftarrow u \hat{\ } r$  ▷ Extend sequence of permutations
19:       $v \leftarrow v \hat{\ } 1$  ▷ Extend sequence of counts
20:    end if
21:  end for
22:  return  $\{(u_i, v_i \div \text{GCD}(v_k)) \mid i \in \{1, \dots, |u|\}\}$ 
23: end function
```

B.2.2 Bond stereopermutation

Rotational isomerism along multiple bond-order bonds is modeled with bond stereopermutations. Each side of the bond must have an atom stereopermutator with an assigned stereopermutation. Indeterminate atom stereopermutators cannot map their graph substituents to shape vertices, which is necessary for bond stereopermutation enumeration. The two atom stereopermutators each contribute a shape, a mapping of graph substituents to shape vertices, and their local substituent rankings.

First, representational degrees of freedom are removed to ensure that the stereopermutation enumeration algorithm generates transferable stereodescriptors. Any shape vertex may fuse, but shape vertices that are rotationally interconvertible yield the same set of permutation, but in a different order. Additionally, shape vertex enumeration is ordered arbitrarily. These degrees of freedom are removed by rotating the fused vertex to the algebraically smallest shape vertex of its set of rotationally interconvertible vertices. For example, the octahedron has a single set of interconvertible vertices, but the square pyramid has two: The equatorial set of four vertices, and the singleton set containing the apical vertex.

The degree of freedom reduction is laid out in Algs. 9,10. `Orbits` collects sets of vertices that interconvert in a permutation. `MergePermutations` is an undefined function that merges overlapping orbits. `VertexGroups` yields the vertex sets that are interconvert rotationally in a given shape. The last auxiliary function, `IndexOfPermutation`, establishes ordering of permutations. With these auxiliaries, the representational freedom at each side of the double bond, consisting of a shape, a fused vertex and the ranking characters at each vertex of the shape, can be reduced as shown in Alg. 10.

The enumeration of bond stereopermutations is less amenable to concise expression in mathematical terms than existing algorithm listings, but can be sketched well in words. After reducing the representational degrees of freedom of the state at each side of the bond, the group of shape vertices with minimal angle to the fused vertices is selected at each side. These groups' mutual interaction is the first-order approximation to the dihedral potential and the interaction of vertices further back is neglected entirely. Next, the vertices of each set are ordered by their ranking characters and their value.

If the ranking characters of the set of shape vertices closest to the fused vertex at either side is a singleton set, i.e. all of these vertices have the same ranking character, then rotation around the bond being modeled will be isotropic and there will be only one stereopermutation.

Algorithm 9 Bond stereopermutation degree of freedom reduction auxiliaries

```
1: function ORBITS( $\sigma$ )
2:    $O \leftarrow \emptyset$ 
3:   for all  $i \in \{1, \dots, |\sigma|\}$  do
4:     if  $i \in O_j$  for any  $j$  then
5:        $S \leftarrow \{1\}$ 
6:        $j \leftarrow \sigma(i)$ 
7:       while  $j \neq i$  do
8:          $S \leftarrow S \cup \{j\}$ 
9:          $j \leftarrow \sigma(j)$ 
10:      end while
11:       $O \leftarrow O \cup \{S\}$ 
12:    end if
13:  end for
14:  return  $O$ 
15: end function
16:
17: function VERTEXGROUPS( $s$ )
18:   return ORBITS(MERGEPERMUTATIONS(ROTATIONS( $s$ )))
19: end function
20:
21: function INDEXOFPERMUTATION( $\sigma$ )
22:    $x \leftarrow 0$ 
23:    $a \leftarrow 1$  ▷ Factor
24:    $b \leftarrow 2$  ▷ Position
25:   for all  $i \in \{N - 1, N - 2, \dots, 1\}$  do
26:      $l \leftarrow 0$  ▷ Number of larger successors
27:     for all  $j \in \{i + 1, i + 2, \dots, N\}$  do
28:       if  $\sigma(j) < \sigma(i)$  then
29:          $l \leftarrow l + 1$ 
30:       end if
31:     end for
32:      $x \leftarrow x + l \cdot a$ 
33:      $a \leftarrow a \cdot b$ 
34:      $b \leftarrow b + 1$ 
35:   end for
36:   return  $x$ 
37: end function
```

Algorithm 10 Bond stereopermutation degree of freedom reduction

```

1: function REDUCEDOF( $s, v, c_k$ )  ▷ shape  $s$ , fused vertex  $v$ , ranking chars.  $c_k$ 
2:    $v_{\min} \leftarrow \inf \{X \mid X \in \text{VERTEXGROUPS}(s) \wedge v \in X\}$   ▷ Smallest in orbit
3:    $P \leftarrow \{\sigma \mid \sigma \in \text{ROTATIONS}(s) \wedge \sigma(v) = v_{\min}\}$ 
4:    $\sigma_{\min} \leftarrow \underset{\sigma \in P}{\text{argmin}} \text{INDEXOFPERMUTATION}(\sigma)$ 
5:   return ( $\sigma_{\min}(v), \sigma_{\min}c_k$ )
6: end function
  
```

Otherwise, the dihedral angles are explicitly modeled by arranging both shapes along the fused vertices in a joint coordinate system and sequentially aligning pairs of vertices across both vertex sets in the previously established order and measuring all pairs of dihedral angles at each alignment.

B.2.3 Bond stereopermutation feasibility

The plane that the cyclic polygon expands into is modeled as follows: We define the dihedral point sequence $\vec{A}, \vec{B}, \vec{C}, \vec{D}$ with angles $\alpha = \angle ABC, \beta = \angle BCD$ and dihedral $\varphi = \angle ABCD$ with $|AB| = a, |BC| = b, |CD| = c$ and $\alpha, \beta \in [0, \pi], \varphi \in [-\pi, \pi]$.

We choose the following positions for the points without loss of generality:

$$\vec{A} = \mathbf{R}_z(\alpha)a\vec{e}_x \quad (7)$$

$$\vec{B} = \vec{0} \quad (8)$$

$$\vec{C} = b\vec{e}_x \quad (9)$$

$$\vec{D} = \mathbf{R}_x(\varphi) \left[\vec{C} + \mathbf{R}_z(\pi - \beta)c\vec{e}_x \right], \quad (10)$$

where \vec{e}_x is the unit vector along the x -axis and \mathbf{R}_i is the rotation matrix along the axis i . The dihedral distance is the length of the line segment \overline{AD} . In order to find the shortest distance between the line segments \overline{AD} and \overline{BC} , we define:

$$\overline{BC} : \vec{r}(\lambda) = \vec{B} + \lambda(\vec{C} - \vec{B}) = \lambda\vec{C}, \lambda \in [0, 1] \quad (11)$$

$$\overline{AD} : \vec{s}(\mu) = \vec{A} + \mu(\vec{D} - \vec{A}), \mu \in [0, 1] \quad (12)$$

The shortest distance between the line segments must be orthogonal to both line segments' direction vectors:

$$\left[\lambda\vec{C} - \left(\vec{A} + \mu(\vec{D} - \vec{A}) \right) \right] \cdot \vec{C} = 0 \quad (13)$$

$$\left[\lambda\vec{C} - \left(\vec{A} + \mu(\vec{D} - \vec{A}) \right) \right] \cdot (\vec{D} - \vec{A}) = 0 \quad (14)$$

Solving this system of equations yields:

$$\mu_0 = -\frac{A_y S_y + A_z S_z}{S_y^2 + S_z^2} \quad (15)$$

$$\lambda_0 = \frac{A_x + \mu_0 S_x}{b} \quad (16)$$

with $\vec{S} = \vec{D} - \vec{A}$. These solutions do not satisfy their conditions yet, and must be adjusted slightly:

$$\lambda_m = \min(\max(\lambda_0, 0), 1) \quad (17)$$

$$\mu_m = \begin{cases} -\frac{A_x}{S_x} & \lambda_0 \leq 0 \\ \frac{b - A_x}{S_x} & \lambda_0 \geq 1 \\ \lambda_0 & \text{else} \end{cases} \quad (18)$$

The plane in which the cyclic polygon expands can then be defined through the three points \vec{A} , \vec{D} , and $\vec{r}(\lambda_m)$. For $\varphi = \pm\pi$, these points become collinear and the plane definition is not uniquely defined. Under these circumstances, the plane can instead be defined using the point \vec{A} and the two vectors $(\vec{D} - \vec{A})$ and \vec{e}_z .

B.3 Isomorphism and Canonicalization

The graph data structures and several related algorithms in MOLASSEMBLER are provided by the Boost Graph Library from the Boost family of C++ libraries.⁶⁴ Molecule comparison is implemented as a colored graph isomorphism that is modular in vertex coloring. The following types of information can be collected to color a vertex: the element type of the atom, its bond orders to adjacent vertices, the shape of its atom stereopermutator (if present), and the stereopermutation of its stereopermutator (if present). Note that indeterminate atom stereopermutators will have a different color than a stereopermutator with a set stereopermutation. As a consequence, molecules with indeterminate stereopermutators will not compare equal to an otherwise equivalent molecule with assigned stereopermutators. The varying levels of information for graph coloring are collected into a 128-bit hash, but in a bijective manner, i.e. without the possibility of hash collision. These hashes then represent the color of each vertex and are passed as input to the Boost isomorphism function.

Canonicalization of the molecule representation is similarly modular. First, modular hashes of vertices are calculated according to algorithm input. Next, the canonical automorphism is determined by processing the graph and its vertex hashes by the

nauty⁵⁸ library. Specifically, the SPARSENAUTY function is called, specifying distance vertex invariants for canonical labeling. Lastly, the canonical automorphism is applied to the graph and its stereopermutators.

B.4 Distance Geometry error function derivative

For a given set of N particles with positions \vec{r}_i , the Distance Geometry error function applied is the sum of distance errors a , chiral errors b and dihedral errors c .

$$a = \sum_{i < j}^N \left[\max^2 \left(0, \frac{r_{ij}^2}{U_{ij}^2} - 1 \right) + \max^2 \left(0, \frac{2L_{ij}^2}{L_{ij}^2 + r_{ij}^2} - 1 \right) \right] \quad (19)$$

The symbols U_{ij} and L_{ij} are the upper and lower distance bounds for the atoms i and j .

$$b = \sum_{(S_\alpha, S_\beta, S_\gamma, S_\delta, U_V, L_V) \in C} \max^2(0, V_{\alpha\beta\gamma\delta}(\{\vec{r}_i\}) - U_V) + \max^2(0, L_V - V_{\alpha\beta\gamma\delta}(\{\vec{r}_i\})) \quad (20)$$

Within the chiral errors, C is a set of chiral constraint tuples consisting of the particle sets $S_\alpha, S_\beta, S_\gamma$ and S_δ . These contain mutually disjoint particle indices and contain at least one element. In further notation, \vec{s} denotes the average spatial position of all elements of a set, e.g. for S_α :

$$\vec{s}_\alpha = \frac{1}{|S_\alpha|} \sum_{i=1}^{|S_\alpha|} \vec{r}_{S_\alpha, i}, \quad (21)$$

where $|S_\alpha|$ denotes the number of elements in the set and $S_{\alpha, i}$ is the i -th element in the set.

The constraint tuple further consists of the scalars U_V and L_V , which are upper and lower bounds on the volume spanned by the average positions of the sets $S_\alpha, S_\beta, S_\gamma$ and S_δ . This volume is calculated in the symbol $V_{\alpha\beta\gamma\delta}$, which is the signed tetrahedron volume spanned by $\vec{s}_\alpha, \vec{s}_\beta, \vec{s}_\gamma$ and \vec{s}_δ :

$$V_{\alpha\beta\gamma\delta}(\{\vec{r}_i\}) = (\vec{s}_\alpha - \vec{s}_\delta)^T \cdot [(\vec{s}_\beta - \vec{s}_\delta) \times (\vec{s}_\gamma - \vec{s}_\delta)]. \quad (22)$$

It is important to note that tetrahedron volumes such as U_V are signed values. On odd permutations of constituting indices, these quantities change sign.

$$c = \sum_{(S_\alpha, S_\beta, S_\gamma, S_\delta, U_\phi, L_\phi) \in D} \max^2 \left(0, \left| \phi + \bar{\phi} - \frac{U_\phi + L_\phi}{2} \right| - \frac{U_\phi - L_\phi}{2} \right) \quad (23)$$

Within the dihedral errors, D is a set of dihedral constraint tuples. Each tuple consists of four particle index sets $S_\alpha, S_\beta, S_\gamma$ and S_δ and upper and lower bounds on the dihedral angle U_ϕ and L_ϕ . Exactly as for chiral errors, the particle index sets do not intersect and each contain at least a single element. The dihedral angle ϕ is defined via the particle index sets, where $\vec{s}_{ij} = \vec{s}_j - \vec{s}_i$:

$$\phi = \text{atan2}\left((\vec{s}_{\alpha\beta} \times \vec{s}_{\beta\gamma}) \times (\vec{s}_{\beta\gamma} \times \vec{s}_{\gamma\delta}) \cdot \frac{\vec{s}_{\beta\gamma}}{|\vec{s}_{\beta\gamma}|}, (\vec{s}_{\alpha\beta} \times \vec{s}_{\beta\gamma}) \cdot (\vec{s}_{\beta\gamma} \times \vec{s}_{\gamma\delta}) \right) \quad (24)$$

Here we have used a three-vector dihedral angle definition and inserted the index set average-position differences that constitute the dihedral angle. Another definition of the dihedral angle with merely the inverse cosine is:

$$\phi = \arccos \frac{(\vec{s}_{\beta\alpha} \times \vec{s}_{\gamma\beta})(\vec{s}_{\gamma\beta} \times \vec{s}_{\gamma\delta})}{|\vec{s}_{\beta\alpha} \times \vec{s}_{\gamma\beta}| |\vec{s}_{\gamma\beta} \times \vec{s}_{\gamma\delta}|}, \quad (25)$$

whose derivatives w.r.t. the constituting position vectors are considerably easier to evaluate. $\bar{\phi}$ is defined as:

$$\bar{\phi} = \begin{cases} 2\pi & \text{if } \phi < \frac{U_\phi + L_\phi - 2\pi}{2} \\ -2\pi & \text{if } \phi > \frac{U_\phi + L_\phi + 2\pi}{2} \\ 0 & \text{else} \end{cases} \quad (26)$$

For a scalar-valued function E , the columnar gradient of the error function is composed of partial derivatives to the individual position vectors \vec{r}_i :

$$\nabla E = \left(\frac{\partial E}{\partial \vec{r}_1}, \frac{\partial E}{\partial \vec{r}_2}, \dots, \frac{\partial E}{\partial \vec{r}_N} \right)$$

Each individual component $(\partial E / \partial \vec{r}_\xi)$ is a vector whose components are the scalar derivatives:

$$\frac{\partial E}{\partial \vec{r}_\xi} = \begin{pmatrix} \partial E / \partial \vec{r}_{\xi,x} \\ \partial E / \partial \vec{r}_{\xi,y} \\ \partial E / \partial \vec{r}_{\xi,z} \end{pmatrix}$$

We split the problem into five main terms:

$$\begin{aligned}
\frac{\partial}{\partial \vec{r}_\xi} \text{erf}(\{\vec{r}_i\}) &= \underbrace{\frac{\partial}{\partial \vec{r}_\xi} \left(\sum_{i < j}^N \max^2 \left(0, \frac{\vec{r}_{ij}^2}{U_{ij}^2} - 1 \right) \right)}_{\textcircled{1}} \\
&+ \underbrace{\frac{\partial}{\partial \vec{r}_\xi} \left(\sum_{i < j}^N \max^2 \left(0, \frac{2L_{ij}^2}{L_{ij}^2 + \vec{r}_{ij}^2} - 1 \right) \right)}_{\textcircled{2}} \\
&+ \underbrace{\frac{\partial}{\partial \vec{r}_\xi} \sum_{(S_\alpha, S_\beta, S_\gamma, S_\delta, U_V, L_V) \in C} \max^2(0, V_{\alpha\beta\gamma\delta}(\{\vec{r}_i\}) - U_V)}_{\textcircled{3}} \\
&+ \underbrace{\frac{\partial}{\partial \vec{r}_\xi} \sum_{(S_\alpha, S_\beta, S_\gamma, S_\delta, U_V, L_V) \in C} \max^2(0, L_V - V_{\alpha\beta\gamma\delta}(\{\vec{r}_i\}))}_{\textcircled{4}} \\
&+ \underbrace{\frac{\partial}{\partial \vec{r}_\xi} \sum_{(S_\alpha, S_\beta, S_\gamma, S_\delta, U_\phi, L_\phi) \in D} \max^2 \left(0, \left| \phi + \bar{\phi} - \frac{U_\phi + L_\phi}{2} \right| - \frac{U_\phi - L_\phi}{2} \right)}_{\textcircled{5}}.
\end{aligned}$$

B.5 Distance error terms

We begin with $\textcircled{1}$, applying the chain rule:

$$\begin{aligned}
&\frac{\partial}{\partial \vec{r}_\xi} \sum_{i < j}^N \max^2 \left(0, \frac{\vec{r}_{ij}^2}{U_{ij}^2} - 1 \right) \\
&= 2 \sum_{i < j}^N \max \left(0, \frac{\vec{r}_{ij}^2}{U_{ij}^2} - 1 \right) \frac{\partial}{\partial \vec{r}_\xi} \max \left(0, \frac{\vec{r}_{ij}^2}{U_{ij}^2} - 1 \right).
\end{aligned} \tag{27}$$

If $\xi = i$, then:

$$\frac{\partial}{\partial \vec{r}_i} \frac{\vec{r}_{ij}^2}{U_{ij}^2} - 1 = -\frac{2}{U_{ij}^2} r_{ij} \tag{28}$$

and likewise, but positive, for $\xi = j$. Consequently:

$$\begin{aligned} \frac{\partial}{\partial \vec{r}_\xi} \left(\max \left(0, \frac{\vec{r}_{ij}^2}{U_{ij}^2} - 1 \right) \right) &= \frac{2}{U_{ij}^2} \vec{r}_{ij} \begin{cases} -1 & \text{if } \xi = i \\ 1 & \text{if } \xi = j \\ 0 & \text{else} \end{cases} \\ &= \frac{2}{U_{ij}^2} \vec{r}_{ij} (\delta_{\xi j} - \delta_{\xi i}), \end{aligned} \quad (29)$$

where we have discarded the possibility of $\frac{\vec{r}_{ij}^2}{U_{ij}^2} - 1 < 0$ since this case is adequately covered by the first maximum function. δ is the Kronecker delta. So, in total we have:

$$\textcircled{1} = \sum_{i < j}^N (\delta_{\xi j} - \delta_{\xi i}) \underbrace{\frac{4}{U_{ij}^2} \vec{r}_{ij} \max \left(0, \frac{\vec{r}_{ij}^2}{U_{ij}^2} - 1 \right)}_{f(i,j)} \quad (30)$$

We can transform the summation further with Kronecker deltas:

$$\sum_{i < j}^N (\delta_{\xi j} - \delta_{\xi i}) f(i, j) \quad (31)$$

$$= \sum_{i=1}^{\xi-1} f(i, \xi) - \sum_{j=\xi+1}^N f(\xi, j) \quad (32)$$

$$= \sum_{i=1}^{\xi-1} f(i, \xi) + \sum_{i=\xi+1}^N f(i, \xi) \quad (33)$$

$$= \sum_{i=1}^N (1 - \delta_{i\xi}) f(i, \xi), \quad (34)$$

where we have used that $f(i, j) = -f(j, i)$ (see Eq. 30). All in all:

$$\textcircled{1} = \sum_{i=1}^N (1 - \delta_{i\xi}) \frac{4}{U_{i\xi}^2} \vec{r}_{i\xi} \max \left(0, \frac{\vec{r}_{i\xi}^2}{U_{i\xi}^2} - 1 \right) \quad (35)$$

Let us continue with $\textcircled{2}$. Once again, we apply the chain rule:

$$\begin{aligned} &\frac{\partial}{\partial \vec{r}_\xi} \sum_{i < j}^N \max^2 \left(0, \frac{2L_{ij}^2}{L_{ij}^2 + \vec{r}_{ij}^2} - 1 \right) \\ &= 2 \sum_{i < j}^N \max \left(0, \frac{2L_{ij}^2}{L_{ij}^2 + \vec{r}_{ij}^2} - 1 \right) \frac{\partial}{\partial \vec{r}_\xi} \max \left(0, \frac{2L_{ij}^2}{L_{ij}^2 + \vec{r}_{ij}^2} - 1 \right) \end{aligned} \quad (36)$$

For $\xi = i$,

$$\frac{\partial}{\partial \vec{r}_i} \left(\frac{2L_{ij}^2}{L_{ij}^2 + \vec{r}_{ij}^2} - 1 \right) = \frac{4L_{ij}^2 \vec{r}_{ij}}{(L_{ij}^2 + \vec{r}_{ij}^2)^2}, \quad (37)$$

and likewise, but negative, for $\xi = j$. Therefore,

$$\begin{aligned} \frac{\partial}{\partial \vec{r}_\xi} \left(\max \left(0, \frac{2L_{ij}^2}{L_{ij}^2 + \vec{r}_{ij}^2} - 1 \right) \right) &= \frac{4L_{ij}^2 \vec{r}_{ij}}{(L_{ij}^2 + \vec{r}_{ij}^2)^2} \begin{cases} 1 & \text{if } \xi = i \\ -1 & \text{if } \xi = j \\ 0 & \text{else} \end{cases} \\ &= \frac{4L_{ij}^2 \vec{r}_{ij}}{(L_{ij}^2 + \vec{r}_{ij}^2)^2} (\delta_{\xi i} - \delta_{\xi j}), \end{aligned}$$

where we have excluded the possibility of $\frac{2L_{ij}^2}{L_{ij}^2 + \vec{r}_{ij}^2} - 1 < 0$ since this case is covered by the first maximum function. Altogether:

$$\textcircled{2} = \sum_{i < j}^N (\delta_{\xi i} - \delta_{\xi j}) \underbrace{\frac{8L_{ij}^2 \vec{r}_{ij}}{(L_{ij}^2 + \vec{r}_{ij}^2)^2} \max \left(0, \frac{2L_{ij}^2}{L_{ij}^2 + \vec{r}_{ij}^2} - 1 \right)}_{g(i,j)}. \quad (38)$$

Transforming the summation:

$$\sum_{i < j}^N (\delta_{\xi i} - \delta_{\xi j}) g(i, j) = - \sum_{i=1}^{\xi-1} g(i, \xi) + \sum_{j=\xi+1}^N g(\xi, j) \quad (39)$$

$$= \sum_{i=1}^{\xi-1} g(\xi, i) + \sum_{i=\xi+1}^N g(\xi, i) \quad (40)$$

$$= \sum_{i=1}^N (1 - \delta_{i\xi}) g(\xi, i), \quad (41)$$

Where we have used $g(i, j) = -g(j, i)$ (see Eq. 38). All in all:

$$\textcircled{2} = \sum_{i=1}^N (1 - \delta_{i\xi}) \frac{8L_{\xi i}^2 \vec{r}_{i\xi}}{(L_{\xi i}^2 + \vec{r}_{i\xi}^2)^2} \max \left(0, \frac{2L_{\xi i}^2}{L_{\xi i}^2 + \vec{r}_{i\xi}^2} - 1 \right) \quad (42)$$

B.5.1 Chiral error terms

Next, we consider $\textcircled{3}$. Applying the chain rule yields:

$$\begin{aligned} & \frac{\partial}{\partial \vec{r}_\xi} \sum_{(S_\alpha, S_\beta, S_\gamma, S_\delta, U_V, L_V) \in C} \max^2(0, V_{\alpha\beta\gamma\delta}(\{\vec{r}_i\}) - U_V) \\ &= 2 \sum_{(\dots) \in C} \max(0, V_{\alpha\beta\gamma\delta}(\{\vec{r}_i\}) - U_V) \frac{\partial}{\partial \vec{r}_\xi} \max(0, V_{\alpha\beta\gamma\delta}(\{\vec{r}_i\}) - U_V) \end{aligned}$$

The partial derivatives of $V_{\alpha\beta\gamma\delta}(\{\vec{r}_i\})$ with respect to \vec{r}_ξ are split into five cases. The index ξ can be an element of one of the four sets $S_\alpha, S_\beta, S_\gamma, S_\delta$ (and only one, since they are mutually disjoint) or not. The derivative for the last case is zero. In the remaining cases, one average vector \vec{s} is a function of \vec{r}_ξ but the rest are not. The partial derivative of any average vector \vec{s} is:

$$\frac{\partial}{\partial \vec{r}_\xi} \vec{s}_\alpha = \frac{\partial}{\partial \vec{r}_\xi} \frac{1}{|S_\alpha|} \sum_{i=1}^{|S_\alpha|} \vec{r}_{S_\alpha, i} = \begin{cases} \frac{1}{|S_\alpha|} \mathbf{I}_3 & \text{if } \xi \in S_\alpha \\ 0 & \text{else} \end{cases} \quad (43)$$

where \mathbf{I}_3 denotes the three dimensional identity matrix. The individual set membership cases are thus as follows:

$$\begin{aligned} \textcircled{S_\alpha} & \frac{\partial}{\partial \vec{r}_\xi} \left\{ (\vec{s}_\alpha - \vec{s}_\delta)^T \cdot [(\vec{s}_\beta - \vec{s}_\delta) \times (\vec{s}_\gamma - \vec{s}_\delta)] \right\} \\ &= \frac{\partial}{\partial \vec{r}_\xi} \left\{ \vec{s}_\alpha^T \cdot [(\vec{s}_\beta - \vec{s}_\delta) \times (\vec{s}_\gamma - \vec{s}_\delta)] \right\} - \vec{0} \\ &= \frac{1}{|S_\alpha|} [(\vec{s}_\beta - \vec{s}_\delta) \times (\vec{s}_\gamma - \vec{s}_\delta)] \\ &= \frac{\vec{s}_{\delta\beta} \times \vec{s}_{\delta\gamma}}{|S_\alpha|} \end{aligned}$$

In shorthand notation, in which all \vec{s} symbols are replaced by their subscripts:

$$\begin{aligned}
\textcircled{S_\beta} \quad & \frac{\partial}{\partial \vec{r}_\xi} (\vec{\alpha} - \vec{\delta})^T \cdot [(\vec{\beta} - \vec{\delta}) \times (\vec{\gamma} - \vec{\delta})] \\
&= \frac{\partial}{\partial \vec{r}_\xi} (\vec{\alpha} - \vec{\delta})^T \cdot \left[\vec{\beta} \times \vec{\gamma} - \vec{\beta} \times \vec{\delta} - \vec{\delta} \times \vec{\gamma} + \underbrace{\vec{\delta} \times \vec{\delta}}_{=0} \right] \\
&= \frac{\partial}{\partial \vec{r}_\xi} \left\{ \vec{\beta}^T \cdot [\vec{\gamma} \times (\vec{\alpha} - \vec{\delta})] - \vec{\beta}^T \cdot [\vec{\delta} \times (\vec{\alpha} - \vec{\delta})] \right\} - \vec{0} \\
&= \frac{1}{|S_\beta|} (\vec{\gamma} - \vec{\delta}) \times (\vec{\alpha} - \vec{\delta}) \\
&= -\frac{1}{|S_\beta|} (\vec{\alpha} - \vec{\delta}) \times (\vec{\gamma} - \vec{\delta}) \\
&= -\frac{\vec{s}_{\delta\alpha} \times \vec{s}_{\delta\gamma}}{|S_\beta|}
\end{aligned}$$

$$\begin{aligned}
\textcircled{S_\gamma} \quad & \frac{\partial}{\partial \vec{r}_\xi} (\vec{\alpha} - \vec{\delta})^T \cdot [\vec{\beta} \times \vec{\gamma} - \vec{\beta} \times \vec{\delta} - \vec{\delta} \times \vec{\gamma}] \\
&= \frac{\partial}{\partial \vec{r}_\xi} \left\{ \vec{\gamma}^T \cdot [(\vec{\alpha} - \vec{\delta}) \times \vec{\beta}] - \vec{\gamma}^T \cdot [(\vec{\alpha} - \vec{\delta}) \times \vec{\delta}] \right\} - \vec{0} \\
&= \frac{1}{|S_\gamma|} (\vec{\alpha} - \vec{\delta}) \times (\vec{\beta} - \vec{\delta}) \\
&= \frac{\vec{s}_{\delta\alpha} \times \vec{s}_{\delta\beta}}{|S_\gamma|}
\end{aligned}$$

$$\begin{aligned}
\textcircled{S_\delta} & \frac{\partial}{\partial \vec{r}_\xi} (\vec{\alpha} - \vec{\delta})^T [\vec{\beta} \times \vec{\gamma} - \vec{\beta} \times \vec{\delta} - \vec{\delta} \times \vec{\gamma}] \\
& = \frac{\partial}{\partial \vec{r}_\xi} \vec{\alpha}^T [\vec{\beta} \times \vec{\gamma} - \vec{\beta} \times \vec{\delta} - \vec{\delta} \times \vec{\gamma}] - \frac{\partial}{\partial \vec{r}_\xi} \vec{\delta}^T [\vec{\beta} \times \vec{\gamma} - \vec{\beta} \times \vec{\delta} - \vec{\delta} \times \vec{\gamma}] \\
& = \underbrace{\frac{\partial}{\partial \vec{r}_\xi} \vec{\alpha}^T (\vec{\beta} \times \vec{\gamma})}_{=0} - \frac{\partial}{\partial \vec{r}_\xi} \vec{\alpha}^T (\vec{\beta} \times \vec{\delta}) - \frac{\partial}{\partial \vec{r}_\xi} \vec{\alpha}^T (\vec{\delta} \times \vec{\gamma}) \\
& \quad - \frac{\partial}{\partial \vec{r}_\xi} \vec{\delta}^T (\vec{\beta} \times \vec{\gamma}) + \frac{\partial}{\partial \vec{r}_\xi} \underbrace{\vec{\delta}^T (\vec{\delta} \times \vec{\gamma})}_{=0} + \frac{\partial}{\partial \vec{r}_\xi} \underbrace{\vec{\delta}^T (\vec{\beta} \times \vec{\delta})}_{=0} \\
& = -\frac{\partial}{\partial \vec{r}_\xi} \vec{\delta}^T (\vec{\gamma} \times \vec{\alpha}) - \frac{\partial}{\partial \vec{r}_\xi} \vec{\delta}^T (\vec{\alpha} \times \vec{\beta}) - \frac{\partial}{\partial \vec{r}_\xi} \vec{\delta}^T (\vec{\beta} \times \vec{\gamma}) \\
& = -\frac{1}{|S_\delta|} \vec{\gamma} \times \vec{\alpha} - \frac{1}{|S_\delta|} \vec{\alpha} \times \vec{\beta} - \frac{1}{|S_\delta|} \vec{\beta} \times \vec{\gamma} \\
& = -\frac{1}{|S_\delta|} (\vec{\alpha} - \vec{\gamma}) \times (\vec{\beta} - \vec{\gamma}) \\
& = -\frac{\vec{s}_{\gamma\alpha} \times \vec{s}_{\gamma\beta}}{|S_\delta|}
\end{aligned}$$

All set membership cases can be summed up in a symbol:

$$V_C = \begin{cases} \frac{\vec{s}_{\delta\beta} \times \vec{s}_{\delta\gamma}}{|S_\alpha|} & \text{if } \xi \in S_\alpha \\ -\frac{\vec{s}_{\delta\alpha} \times \vec{s}_{\delta\gamma}}{|S_\beta|} & \text{if } \xi \in S_\beta \\ \frac{\vec{s}_{\delta\alpha} \times \vec{s}_{\delta\beta}}{|S_\gamma|} & \text{if } \xi \in S_\gamma \\ -\frac{\vec{s}_{\gamma\alpha} \times \vec{s}_{\gamma\beta}}{|S_\delta|} & \text{if } \xi \in S_\delta \\ 0 & \text{else} \end{cases} \quad (44)$$

So, overall:

$$\textcircled{3} = \sum_{(S_\alpha, S_\beta, S_\gamma, S_\delta, U_V, L_V) \in C} 2 \max(0, V_{\alpha\beta\gamma\delta}(\{\vec{r}_i\}) - U_V) V_C. \quad (45)$$

For $\textcircled{4}$, the derivation is analog save for the sign of the great amount of cases, which we extrude from the sum:

$$\textcircled{4} = - \sum_{(S_\alpha, S_\beta, S_\gamma, S_\delta, U_V, L_V) \in C} 2 \max(0, L_V - V_{\alpha\beta\gamma\delta}(\{\vec{r}_i\})) V_C. \quad (46)$$

Both terms concerning the chiral error can be summarized as follows:

$$\begin{aligned}
& \textcircled{3} + \textcircled{4} \\
&= \sum_{(\dots) \in C} 2 \max(0, V_{\alpha\beta\gamma\delta}(\{\vec{r}_i\}) - U_V) V_C \\
&\quad - \sum_{(\dots) \in C} 2 \max(0, L_V - V_{\alpha\beta\gamma\delta}(\{\vec{r}_i\})) V_C \\
&= \sum_{(\dots) \in C} 2 V_C \left[\max(0, V_{\alpha\beta\gamma\delta}(\{\vec{r}_i\}) - U_V) - \max(0, L_V - V_{\alpha\beta\gamma\delta}(\{\vec{r}_i\})) \right].
\end{aligned}$$

B.5.2 Dihedral error terms

Finally, we consider $\textcircled{5}$. The chain rule yields:

$$\frac{\partial}{\partial \vec{r}_\xi} \sum_{(\dots) \in D} \max^2(0, h(\phi)) = 2 \sum_{(\dots) \in D} \max(0, h(\phi)) \frac{\partial}{\partial \vec{r}_\xi} \max(0, h(\phi)), \quad (47)$$

where we have substituted the dihedral expression in the maximum function with $h(\phi)$. We can drop the wrapping maximum function in the derivative since the first maximum function adequately covers the case $h(\phi) < 0$. Employing the chain rule again, we note $\frac{\partial}{\partial \vec{r}_\xi} h(\phi) = \frac{\partial h}{\partial \phi} \frac{\partial \phi}{\partial \vec{r}_\xi}$. The first part is:

$$\frac{\partial h}{\partial \phi} = \frac{\partial}{\partial \phi} \left| \underbrace{\phi_{\alpha\beta\gamma\delta}(\{\vec{r}_i\}) + \bar{\phi} - \frac{U_\phi + L_\phi}{2}}_{w(\phi)} \right| - \frac{U_\phi - L_\phi}{2} = \text{sgn}(w(\phi)). \quad (48)$$

The individual derivatives $\frac{\partial \phi}{\partial \vec{s}_\alpha}, \frac{\partial \phi}{\partial \vec{s}_\beta}, \frac{\partial \phi}{\partial \vec{s}_\gamma}, \frac{\partial \phi}{\partial \vec{s}_\delta}$ are given as:

$$\vec{f} = (\vec{s}_\alpha - \vec{s}_\beta), \quad \vec{g} = (\vec{s}_\beta - \vec{s}_\gamma), \quad \vec{h} = (\vec{s}_\delta - \vec{s}_\gamma), \quad (49)$$

$$\vec{a} = \vec{f} \times \vec{g}, \quad \vec{b} = \vec{h} \times \vec{g} \quad (50)$$

$$\begin{aligned}
\frac{\partial \phi}{\partial \vec{s}_\alpha} &= -\frac{|\vec{g}|}{a^2} \vec{a} \\
\frac{\partial \phi}{\partial \vec{s}_\beta} &= \frac{|\vec{g}|}{a^2} \vec{a} + \frac{\vec{f}\vec{g}}{a^2|\vec{g}|} \vec{a} - \frac{\vec{g}\vec{h}}{b^2|\vec{g}|} \vec{b} \\
\frac{\partial \phi}{\partial \vec{s}_\gamma} &= -\frac{|\vec{g}|}{b^2} \vec{b} + \frac{\vec{g}\vec{h}}{b^2|\vec{g}|} \vec{b} - \frac{\vec{f}\vec{g}}{a^2|\vec{g}|} \vec{a} \\
\frac{\partial \phi}{\partial \vec{s}_\delta} &= \frac{|\vec{g}|}{b^2} \vec{b}
\end{aligned} \quad (51)$$

The individual membership cases are therefore:

$$\textcircled{S_i} \quad \frac{\partial \phi}{\partial \vec{r}_\xi} = \frac{\partial \phi}{\partial \vec{s}_i} \frac{\partial \vec{s}_i}{\partial \vec{r}_\xi} = \frac{1}{|S_i|} \frac{\partial \phi}{\partial \vec{s}_i} \quad (52)$$

And altogether:

$$\textcircled{5} = 2 \sum_{(\dots) \in D} \max(0, h(\phi)) \operatorname{sgn}(w(\phi)) \begin{cases} \frac{1}{|S_\alpha|} \frac{\partial \phi}{\partial \vec{s}_\alpha} & \text{if } \xi \in S_\alpha \\ \frac{1}{|S_\beta|} \frac{\partial \phi}{\partial \vec{s}_\beta} & \text{if } \xi \in S_\beta \\ \frac{1}{|S_\gamma|} \frac{\partial \phi}{\partial \vec{s}_\gamma} & \text{if } \xi \in S_\gamma \\ \frac{1}{|S_\delta|} \frac{\partial \phi}{\partial \vec{s}_\delta} & \text{if } \xi \in S_\delta \\ 0 & \text{else} \end{cases} \quad (53)$$

B.6 Demonstration details

Besides the library itself, Python bindings, documentation and tests, the code distribution of MOLASSEMBLER contains a set of analysis binaries that explore the functionality and behavior of particular aspects of the library. Among these is the **Stereopermutations** binary. To reproduce the four stereopermutations arising from the abstract octahedral (A-A)₃ binding case, call the binary as follows:

```
./Stereopermutations -s 12 -c AAAAAA -l "0,1,2,3,4,5"
Shape: octahedron
Characters: AAAAAA
Links: {{0, 1}, {2, 3}, {4, 5}}

Weight 6: chars {A, A, A, A, A, A}, links {[0, 1], [2, 3], [4, 5]},
  link angles: 90 90 180
Weight 4: chars {A, A, A, A, A, A}, links {[0, 1], [2, 4], [3, 5]},
  link angles: 90 90 90
Weight 4: chars {A, A, A, A, A, A}, links {[0, 1], [2, 5], [3, 4]},
  link angles: 90 90 90
Weight 1: chars {A, A, A, A, A, A}, links {[0, 2], [1, 3], [4, 5]},
  link angles: 180 180 180
4 stereopermutations
```

Listing 1: Bidentate octahedron stereopermutations

The other demonstration reinforcing that the molecular model chosen here is suitable for the representation of inorganic molecules with haptic bonding can be reproduced with the Python bindings in just a few lines of code:

```
import sys
import scine_molassembler as masm
```

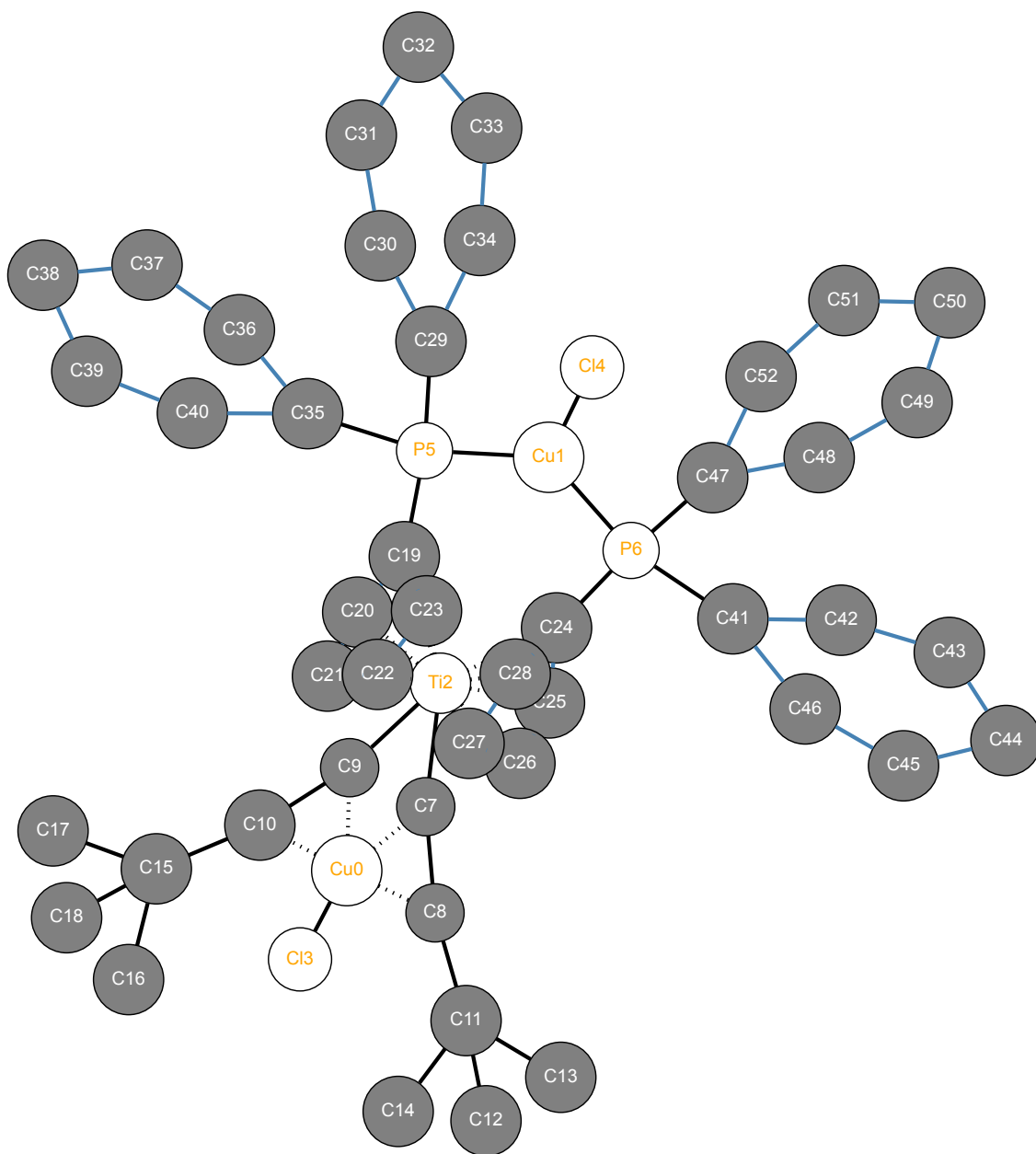


Figure 17: Graphviz output of the BIBTAH Cambridge Crystallographic Database entry after processing by MOLASSEMBLER.

```

name = sys.argv[1]
mols = masm.io.split(name)
for i, mol in enumerate(mols):
    for p in mol.stereopermutators.atom.stereopermutators():
        print(p)

    outname = name.replace(".mol", "-{}.dot".format(i))
    masm.io.write(outname, mol)

```

Listing 2: Python bindings molecule construction

This generates some terminal output and a Graphviz⁷⁹ representation for all molecules in a MOLFile passed as argument. The molecule in question is Cambridge Crystallographic Database⁸⁰ entry BIBTAH.⁸¹ The terminal output contains the following lines of interest:

```

[...]
2: tetrahedron, AABB, A-A, B-B, 0 (1)
[...]
0: triangle, AAB, A-A, 0 (1)
[...]

```

Listing 3: Python terminal output

For reference, an SVG render of the graphviz output is shown in Fig. 17.

B.6.1 Iron compound dataset

The iron compound dataset collected by Proppe and Reiher⁵⁴ with the interpreted shapes of iron atoms, their substituent rankings, number of abstract stereopermutations and number of feasible stereopermutations is shown in Tables 2, 3. In nearly all cases, shapes and ranking results are produced as expected. In the case of compound #17, the classified shape is a trigonal bipyramid, yet we would subjectively judge this a square pyramid. The coordination polyhedron is certainly strongly distorted in this case.

In order to reproduce these results, we must first determine bond orders. Bonds were detected in a binary fashion by summing the covalent radii of each pair of atoms with a tolerance of 0.4 Å, and comparing against the spatial distance. This procedure misclassifies six bonds as present in the dataset (one each in structures #13, 15, 22, 26, 33 and 35) that must be corrected manually. The bond order determination can be repeated with the following Python code:

```

import sys
import scine.utilities as su

```

```
for filename in sys.argv[1:]:
    (coordinates, _) = su.IO.read(filename)
    bonds = su.BondDetector.detect_bonds(coordinates)
    su.IO.write_topology(filename.replace("xyz", "mol"), coordinates,
                        bonds)
```

Listing 4: Dataset bond order determination

Next, the interpretation of molecules can be carried out:

```
import sys
import scine_molassembler as masm

for filename in sys.argv[1:]:
    mol = masm.io.read(filename)
    # The first atom of each structure is an iron atom:
    print(mol.stereopermutators[0])
```

Listing 5: Dataset molecule interpretation

All compounds with their interpreted shapes at iron atoms are shown in Figures 18-25.

Table 2: Interpretation of iron compounds #1–28 from Ref.⁵⁴ This table collects information from the atom-centered stereopermutator placed on an iron atom in the compound (if there are multiple, they are symmetric in this dataset). The polyhedron column collects the IUPAC symbols for the coordination polyhedron of the iron atom. Ranking is the ligand binding case, which abstracts over haptic ligands. Links denotes the connectivity between characters of the ligand binding case. F is the number of feasible stereopermutations and A is the number of abstract stereopermutations.

#	Polyhedron	Ranking	Linking	F	A
1	T-4	AAAA		1	1
2	OC-6	AAAABB	A-A, A-A	3	5
3	T-4	AABB	B-B	1	1
4	T-4	AAAB	A-A, A-A, A-A	1	1
5	TP-3	AAB	A-A	1	1
6	T-4	AAAA	A-A, A-A	1	1
7	SPY-5	AAAAB	A-A, A-A, A-A, A-A	2	5
8	T-4	AAAA		1	1
9	SP-4	AABC	A-B, A-C, A-B, A-C	1	2
10	T-4	AAAB	A-A, A-A, A-A	1	1
11	SP-4	AAAA	A-A, A-A, A-A, A-A	1	2
12	T-4	AAAB	A-A, A-A, A-A	1	1
13	OC-6	AAABCD	A-A, A-A, A-A, B-D, C-D	2	5
14	TP-3	AAB	A-A	1	1
15	OC-6	AAABCD	A-A, A-A, A-A, B-D, C-D	2	5
16	OC-6	AABBCD	A-B, A-C, A-B, A-C	7	16
17	TBPY-5	AABBC	A-B, A-B	10	12
18	TBPY-5	AAABC	A-C, A-C, A-C	3	4
19	OC-6	AABBCD	A-B, A-C, A-B, A-C	7	16
20	OC-6	AABBCD	A-B, A-C, A-B, A-C	7	16
21	OC-6	AABBCC	A-A, A-B, A-B, B-B	3	11
22	SP-4	ABCD	A-B, A-D, B-C	2	3
23	SPY-5	AAAAB	A-A, A-A, A-A, A-A	2	5
24	T-4	AAAA		1	1
25	TBPY-5	AAABC	A-C, A-C, A-C	3	4
26	SP-4	ABCD	A-B, A-C, B-D	2	3
27	SPY-5	AABBC	A-A, A-B, A-B, B-B	5	16
28	T-4	AABC		1	1

Table 3: Interpretation of iron compounds #29–44 from Ref.⁵⁴ For explanations of column headers, refer to Table 2.

#	Polyhedron	Ranking	Linking	F	A
29	OC-6	AAAABB	A-A, A-A	3	5
30	OC-6	AABBCD	A-B, A-B, A-B, A-B	3	8
31	SPY-5	AAAAB	A-A, A-A	3	5
32	T-4	AAAB		1	1
33	OC-6	AABCDE	B-C	12	15
34	OC-6	AABCDE	B-D	12	15
35	OC-6	AABCDE	B-C	12	15
36	OC-6	AABCDE	C-D, D-E	9	15
37	OC-6	AABBCD	A-B, A-C, A-B, A-C	7	16
38	OC-6	AABCDE	C-D	12	15
39	OC-6	AABCDE	D-E	12	15
40	OC-6	AABCDE	C-E	12	15
41	OC-6	AABCDE	D-E	12	15
42	SPY-5	AABBC	A-A, A-B, A-B, B-B	5	16
43	TBPY-5	AAAAA		1	1
44	SPY-5	AABBC	A-A, A-B, A-B, B-B	5	16

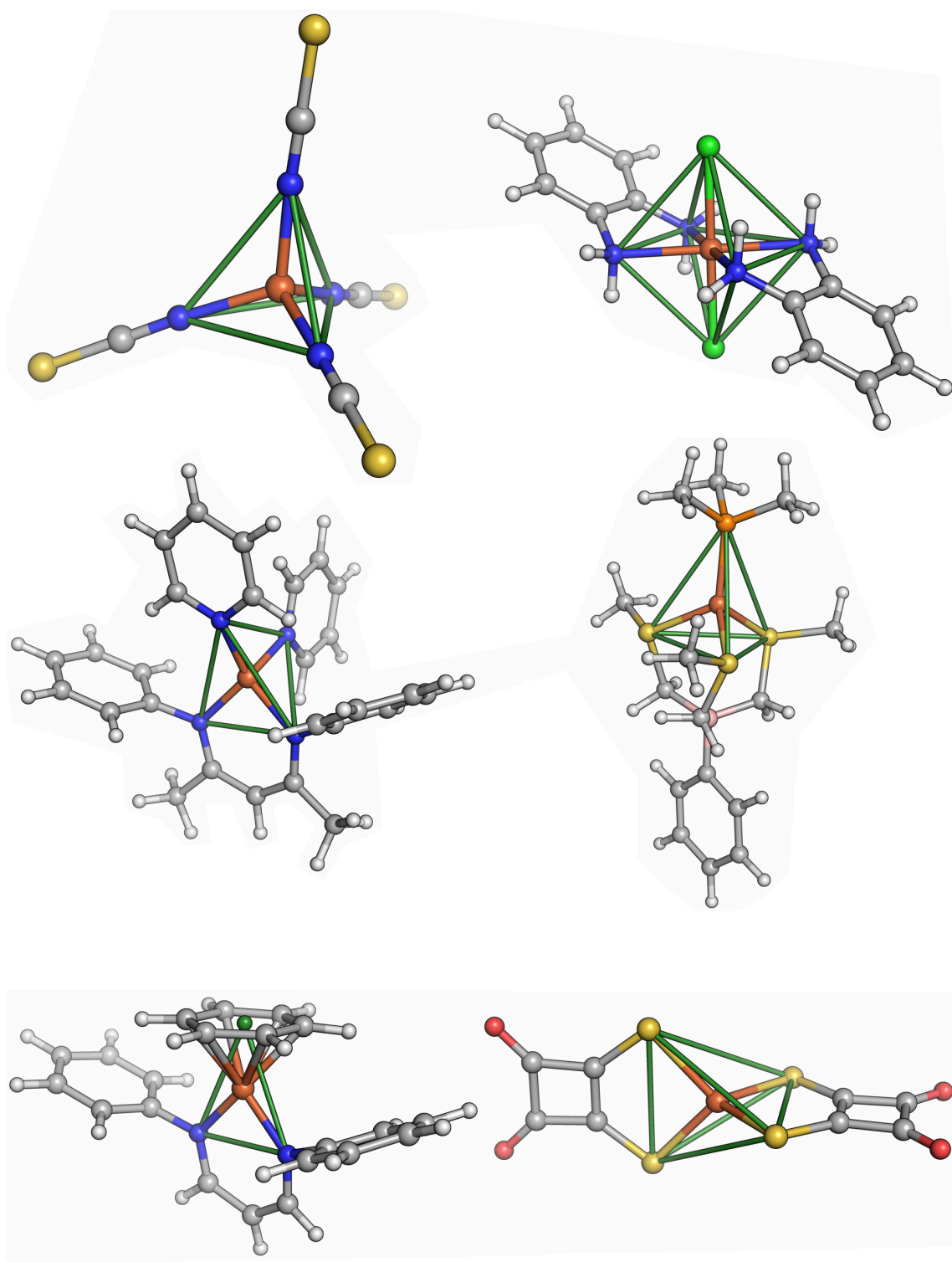


Figure 18: Iron compounds #1–6 arranged left-to-right, then row-wise, with interpreted polyhedral shapes at iron atoms highlighted in green.

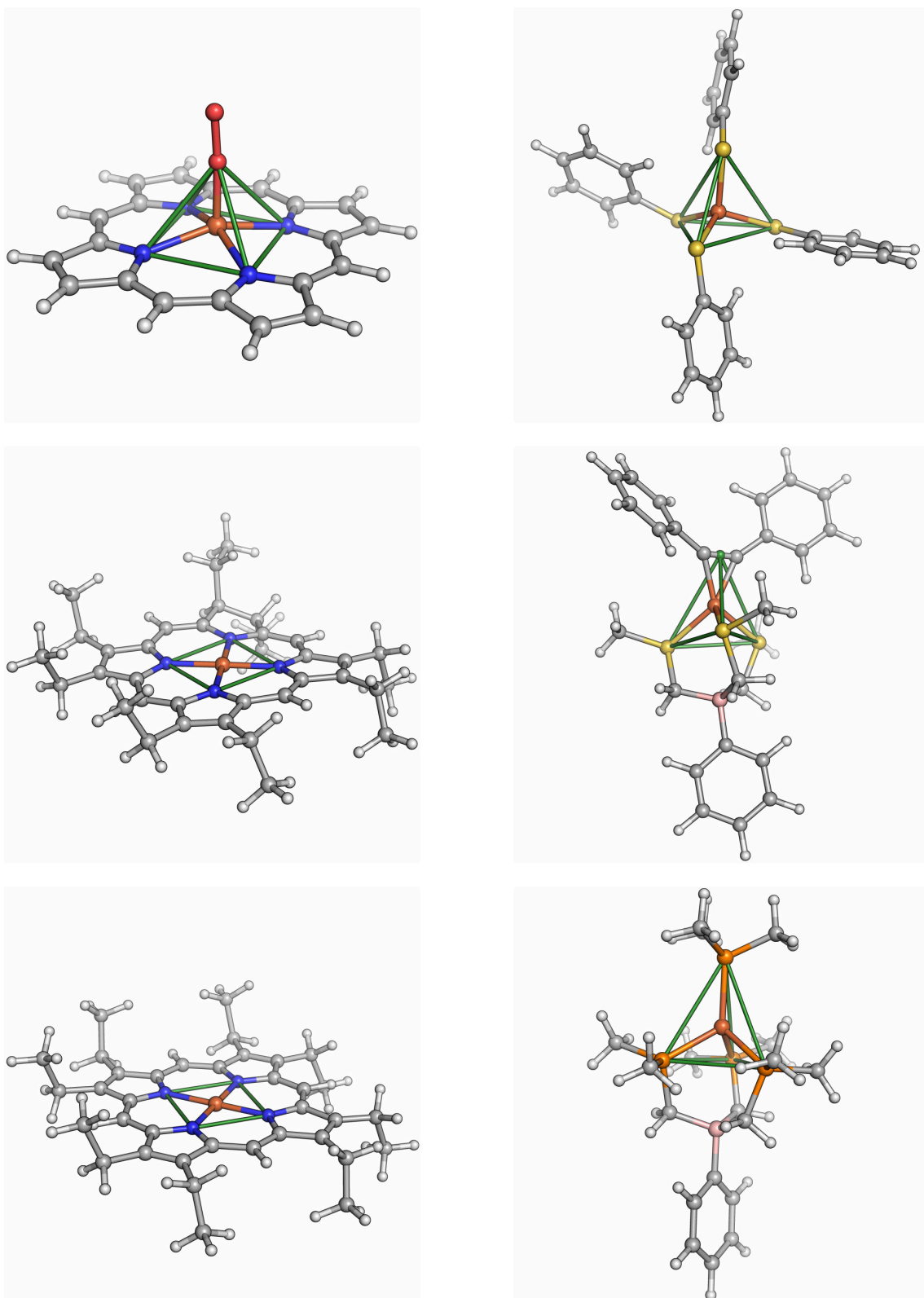


Figure 19: Iron compounds #7–12 arranged left-to-right, then row-wise, with interpreted polyhedral shapes at iron atoms highlighted in green.

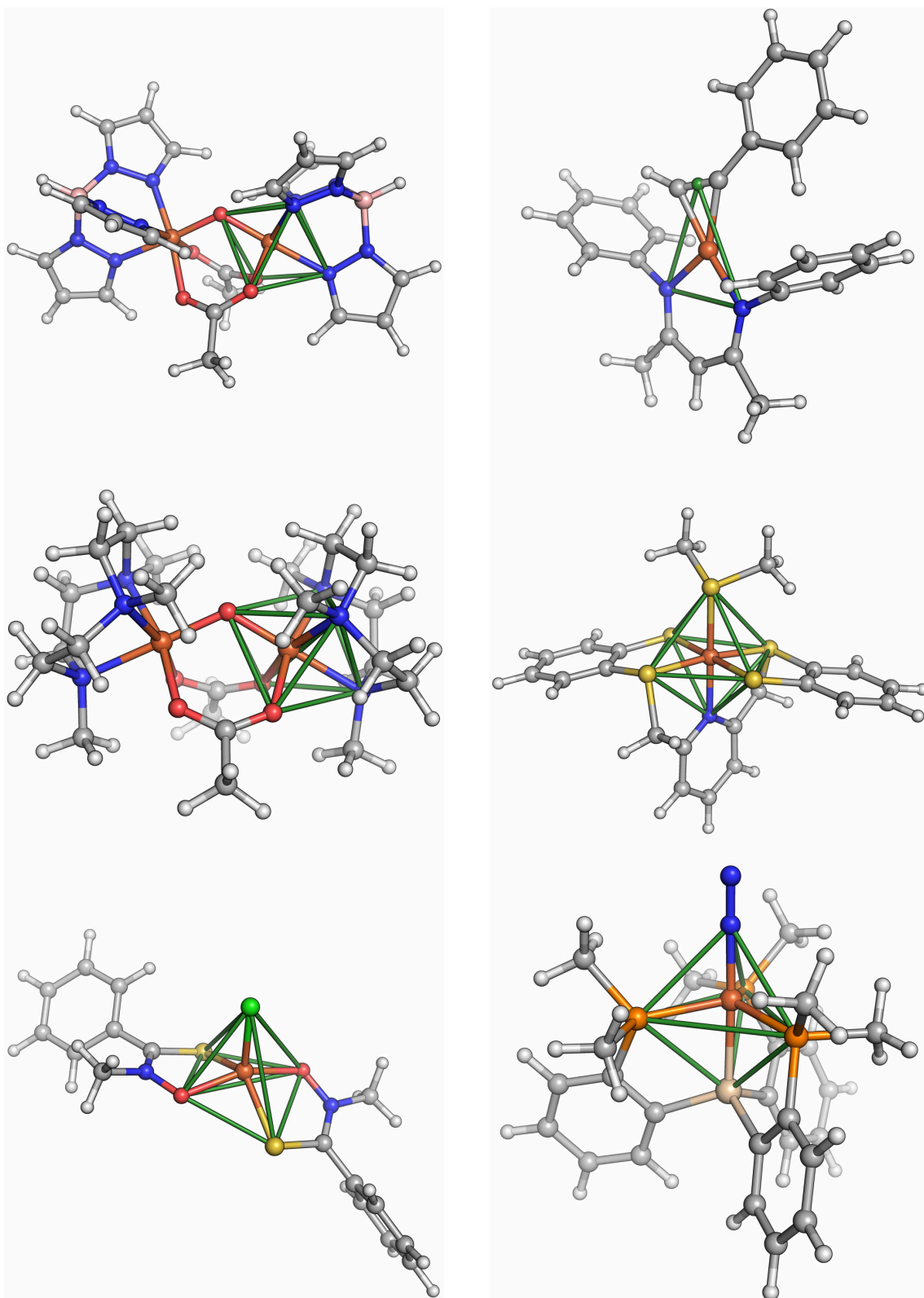


Figure 20: Iron compounds #13–18 arranged left-to-right, then row-wise, with interpreted polyhedral shapes at iron atoms highlighted in green.

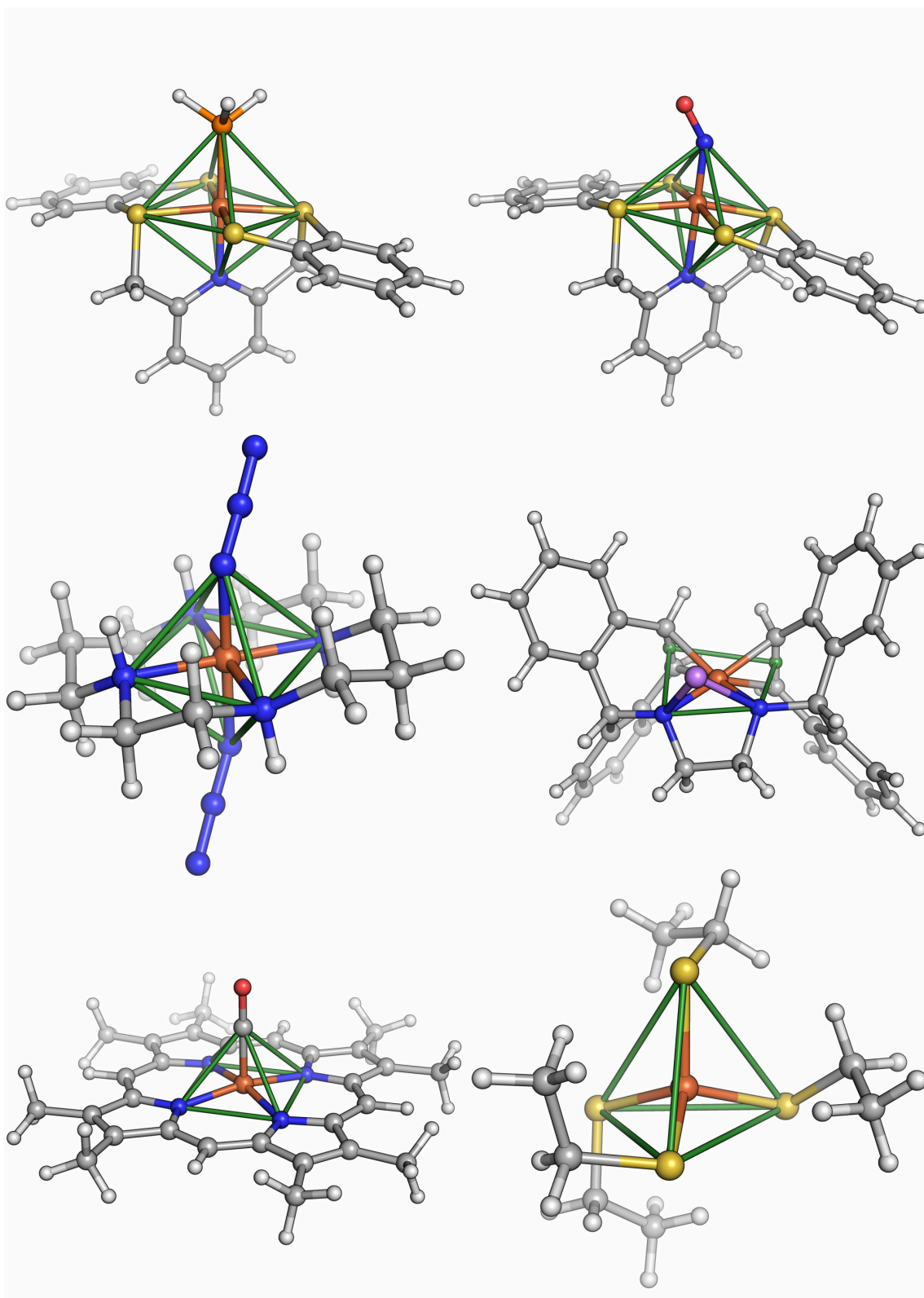


Figure 21: Iron compounds #19–24 arranged left-to-right, then row-wise, with interpreted polyhedral shapes at iron atoms highlighted in green.

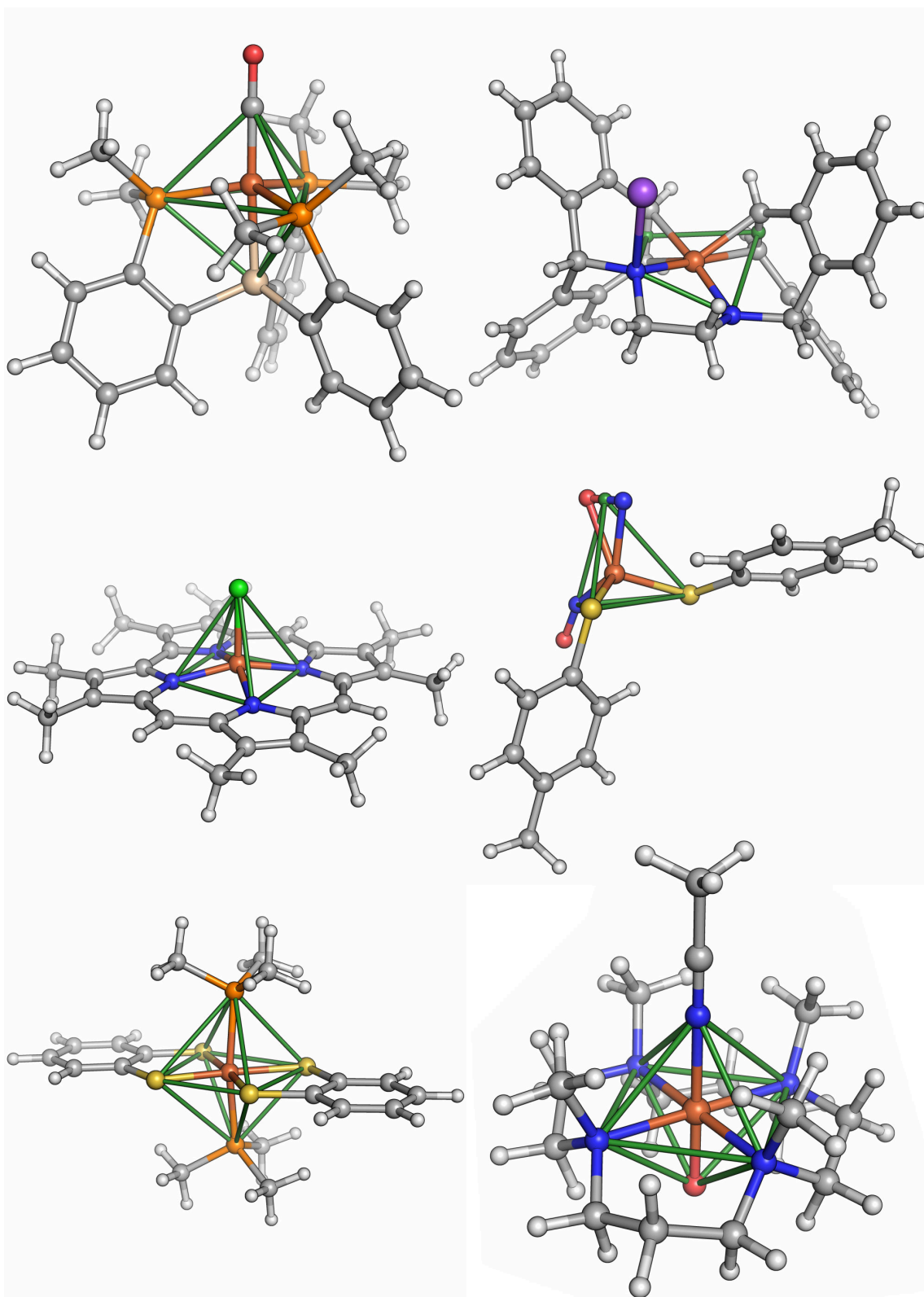


Figure 22: Iron compounds #25–30 arranged left-to-right, then row-wise, with interpreted polyhedral shapes at iron atoms highlighted in green.

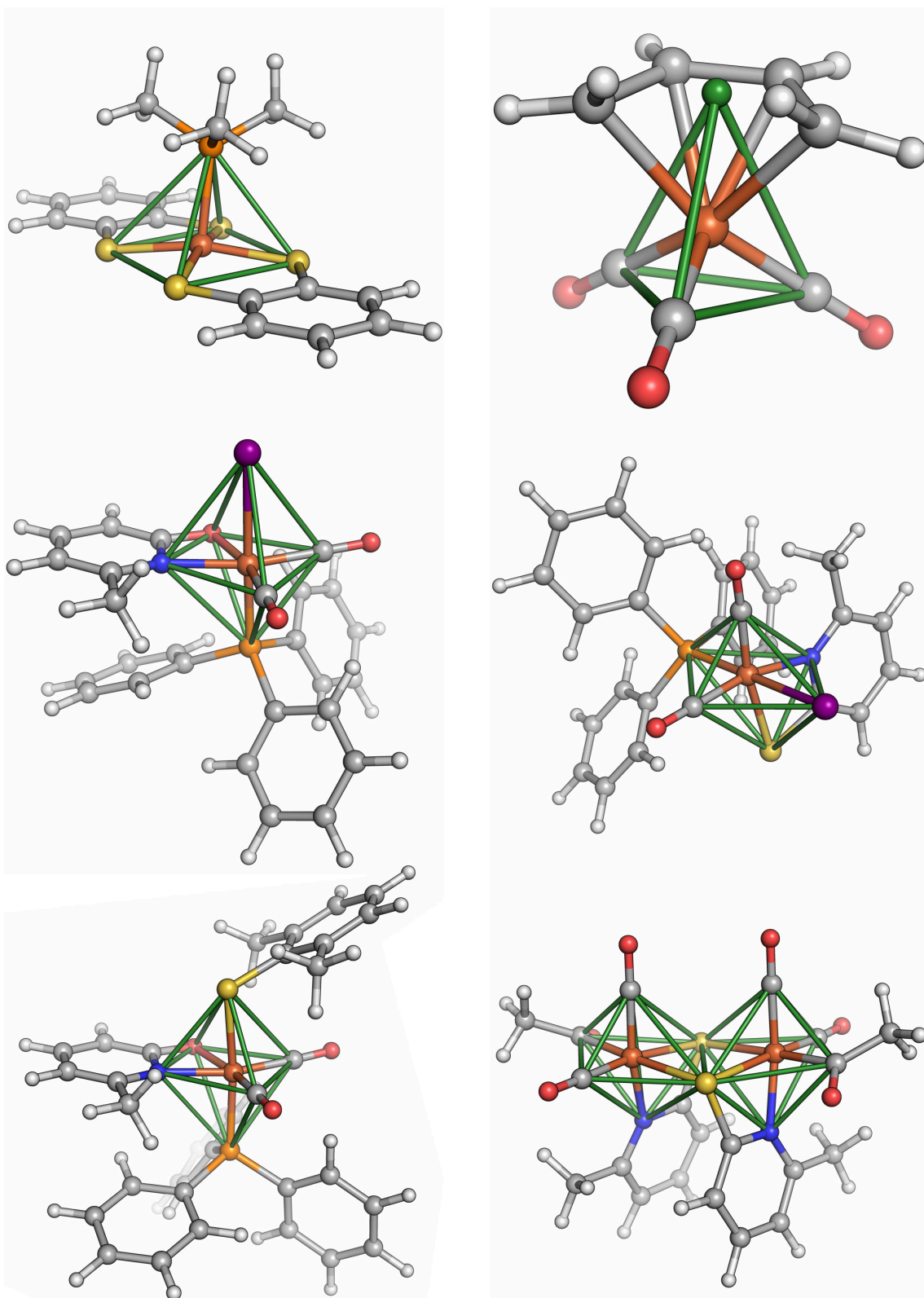


Figure 23: Iron compounds #31–36 arranged left-to-right, then row-wise, with interpreted polyhedral shapes at iron atoms highlighted in green.

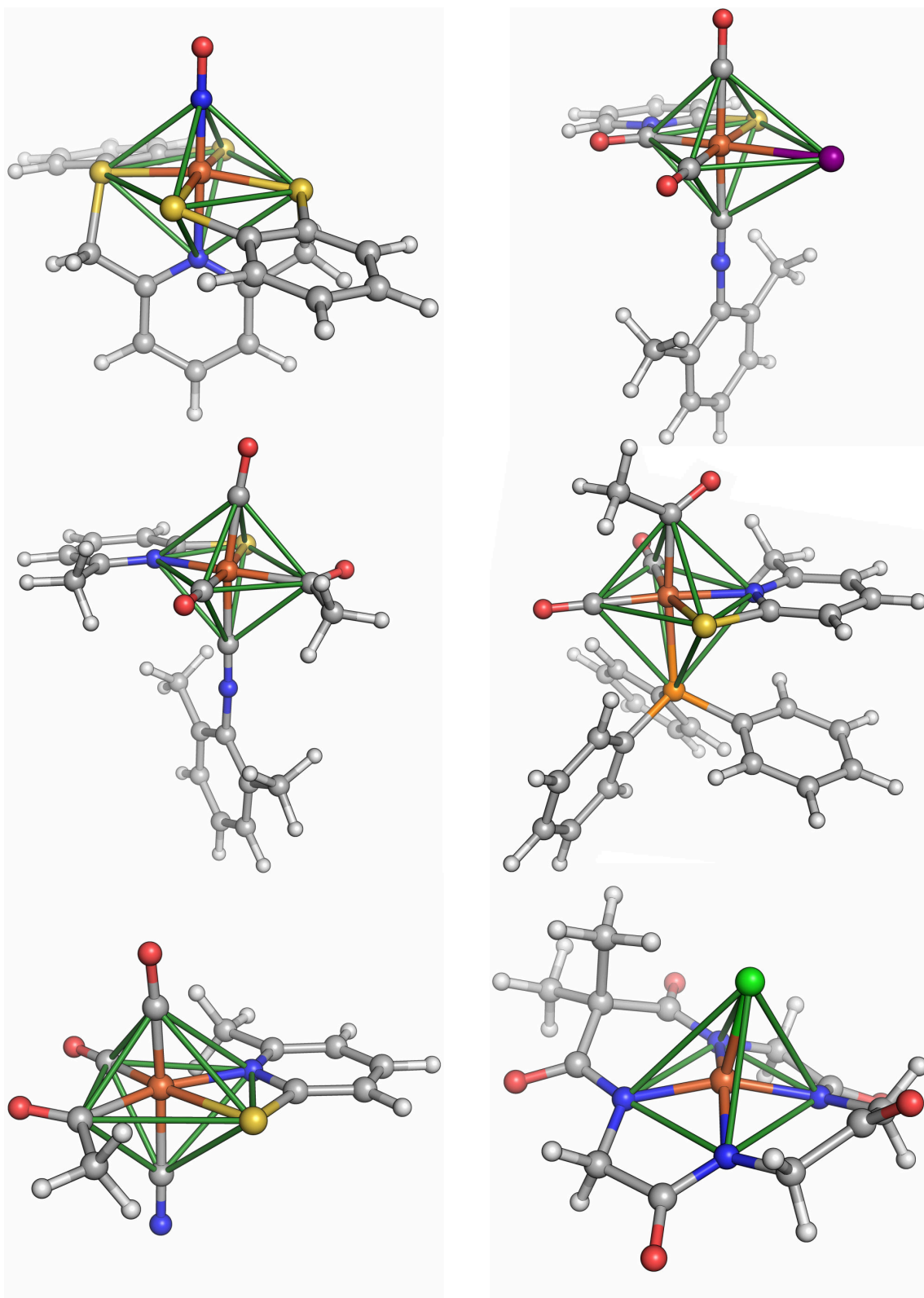


Figure 24: Iron compounds #37–42 arranged left-to-right, then row-wise, with interpreted polyhedral shapes at iron atoms highlighted in green.

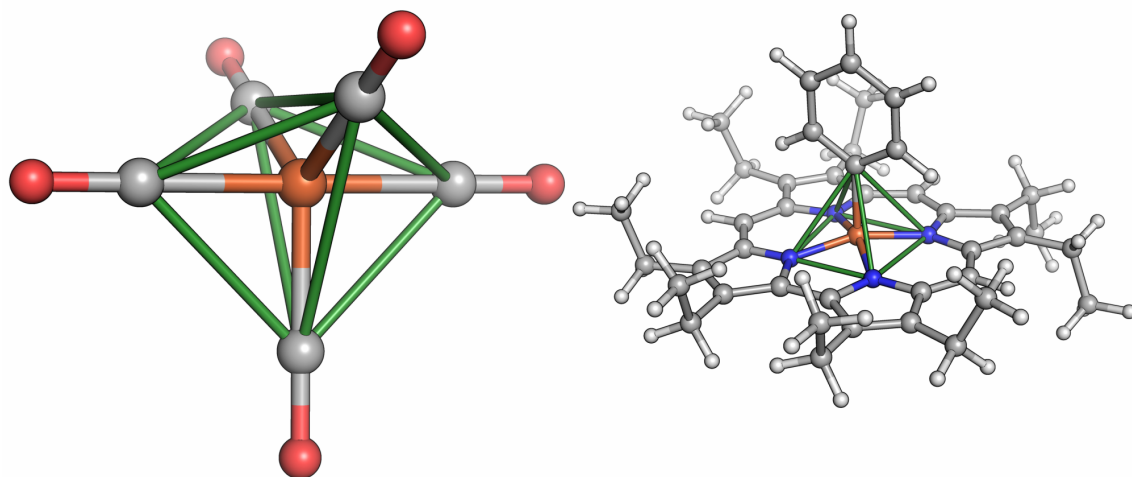


Figure 25: Iron compounds #41 and 42, with interpreted polyhedral shapes at iron atoms highlighted in green.

Lastly, in order to demonstrate a part of the program interface for the generation of conformers, we generate a conformer of each feasible stereopermutation of a structure:

```
import sys
import scine_molassembler as masm

filename = sys.argv[1]
assert filename.endswith(".mol") # We want full topologies here
mol = masm.io.read(filename)

# The first atom of each structure in the dataset is an iron atom:
iron_atom = 0
stereopermutator = mol.stereopermutators[iron_atom]
assert stereopermutator is not None

conformer_seed = 6604

for i in range(stereopermutator.num_assignments):
    print("Trying to generate conformer for assignment {}".format(i))
    # Change the stereopermutator
    mol.assign_stereopermutator(iron_atom, i)

    # Distance Geometry can fail, so we allow several attempts
    xyz = "Failure reasons are communicated by string"
    attempts = 0
    while isinstance(xyz, str):
        if attempts == 10:
            break

        print("Attempt {}".format(attempts))
        # Reuse attempts for seeding to get different reproducible
        conformers
        xyz = masm.dg.generate_conformation(mol, conformer_seed +
        attempts)
        attempts = attempts + 1

    if isinstance(xyz, str):
        print("Could not generate a conformer for assignment {} : {}".
        format(i, xyz))
        continue

    conf_filename = filename.replace(".mol", "-{}.mol".format(i))
    masm.io.write(conf_filename, mol, xyz)
```

Listing 6: Dataset molecule conformer generation

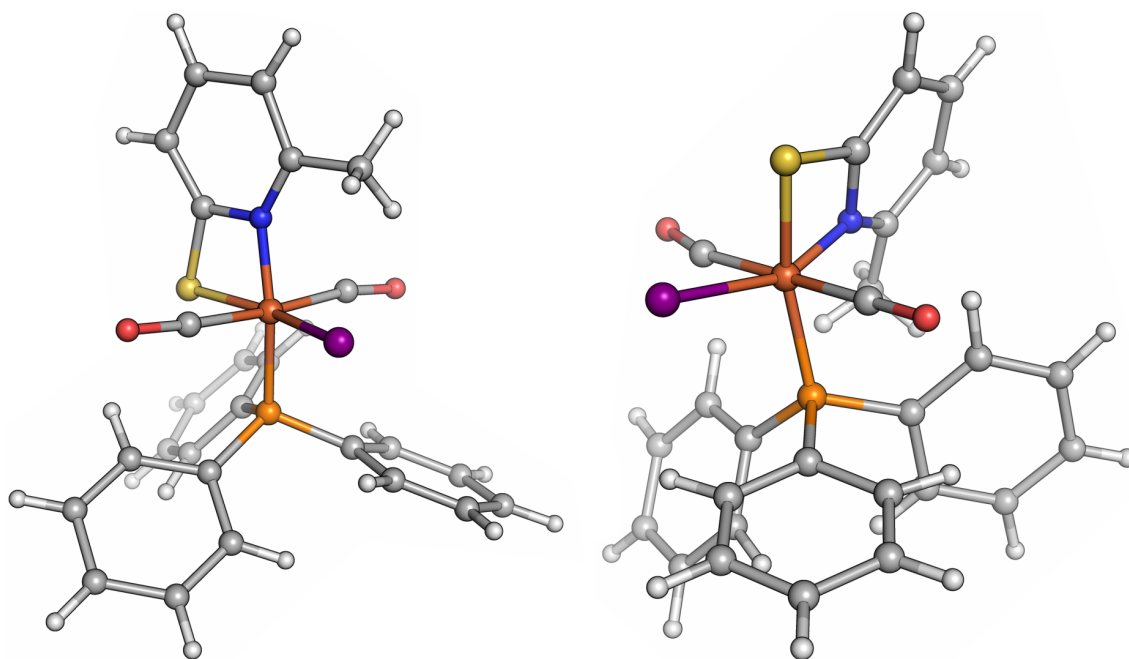


Figure 26: Conformations of stereoisomers of compound #34 of the feasible stereopermutations indexed as 10 and 11 of the iron atom-centered stereopermutator as generated by MOLASSEMBLER.

Conformations of two stereoisomers of compound #34 are displayed in Figure 26.

References

- [1] Pirhadi, S.; Sunseri, J.; Koes, D. R. Open source molecular modeling, *J. Mol. Graph. Model.* **2016**, *69*, 127–143.
- [2] Ambure, P.; Aher, R. B.; Roy, K. Recent Advances in the Open Access Cheminformatics Toolkits, Software Tools, Workflow Environments, and Databases. In *Computer-Aided Drug Discovery*; Zhang, W., Ed.; Springer New York: New York, NY, 2014.
- [3] Foscatto, M.; Occhipinti, G.; Venkatraman, V.; Alsberg, B. K.; Jensen, V. R. Automated Design of Realistic Organometallic Molecules from Fragments, *J. Chem. Inf. Model.* **2014**, *54*, 767–780.
- [4] Chu, Y.; Heyndrickx, W.; Occhipinti, G.; Jensen, V. R.; Alsberg, B. K. An Evolutionary Algorithm for de Novo Optimization of Functional Transition Metal Compounds, *J. Am. Chem. Soc.* **2012**, *134*, 8885–8895.
- [5] *Marvin 5.3.4*; <http://www.chemaxon.com>; ChemAxon: Budapest, Hungary, 2010 last visited June 8, 2020.
- [6] Steinbeck, C.; Han, Y.; Kuhn, S.; Horlacher, O.; Luttmann, E.; Willighagen, E. The Chemistry Development Kit (CDK): An open-source Java library for chemo- and bioinformatics, *J. Chem. Inf. Comp. Sci.* **2003**, *43*, 493–500.
- [7] Ioannidis, E. I.; Gani, T. Z.; Kulik, H. J. molSimplify: A toolkit for automating discovery in inorganic chemistry, *J. Comput. Chem.* **2016**, *37*, 2106–2117.
- [8] Guan, Y.; Ingman, V. M.; Rooks, B. J.; Wheeler, S. E. AARON: An Automated Reaction Optimizer for New Catalysts, *J. Chem. Theory Comput.* **2018**, *14*, 5249–5261.
- [9] Hay, B. P.; Firman, T. K. HostDesigner: a program for the de novo structure-based design of molecular receptors with binding sites that complement metal ion guests, *Inorg. Chem.* **2002**, *41*, 5502–5512.
- [10] Foscatto, M.; Venkatraman, V.; Jensen, V. R. DENOPTIM: Software for Computational de Novo Design of Organic and Inorganic Molecules, *J. Chem. Inf. Model.* **2019**, *59*, 4077–4082.
- [11] Pracht, P.; Bohle, F.; Grimme, S. Automated exploration of the low-energy chemical space with fast quantum chemical methods, *Phys. Chem. Chem. Phys.* **2020**, *22*, 7169–7192.
- [12] Spicher, S.; Grimme, S. Robust Atomistic Modeling of Materials, Organometallic, and Biochemical Systems, *Angew. Chem. Int. Ed. n/a*,.

- [13] Bergeler, M.; Simm, G. N.; Proppe, J.; Reiher, M. Heuristics-Guided Exploration of Reaction Mechanisms, *J. Chem. Theory Comput.* **2015**, *11*, 5712–5722.
- [14] Simm, G. N.; Reiher, M. Context-Driven Exploration of Complex Chemical Reaction Networks, *J. Chem. Theory Comput.* **2017**, *13*, 6108–6119.
- [15] Unsleber, J. P.; Reiher, M. The Exploration of Chemical Reaction Networks, *Ann. Rev. Phys. Chem.* **2020**, *71*, 121–142.
- [16] Tomonori Fukutani.; Miyazawa, K.; Iwata, S.; Satoh, H. G-RMSD: Root Mean Square Deviation Based Method for Three-dimensional Molecular Similarity Determination, *chemRxiv* **2020**, DOI: 10.26434/chemrxiv.11933055.v1.
- [17] Gómez-Bombarelli, R.; Wei, J. N.; Duvenaud, D.; Hernández-Lobato, J. M.; Sánchez-Lengeling, B.; Sheberla, D.; Aguilera-Iparraguirre, J.; Hirzel, T. D.; Adams, R. P.; Aspuru-Guzik, A. Automatic Chemical Design Using a Data-Driven Continuous Representation of Molecules, *ACS Cent. Sci.* **2018**, *4*, 268–276.
- [18] Favre, H. A.; Powell, W. H. *Nomenclature of organic chemistry: IUPAC recommendations and preferred names 2013*; Royal Society of Chemistry: 2013.
- [19] McNaught, A. D. *Compendium of chemical terminology*; Blackwell Science Oxford: 1997.
- [20] Thomassen, C. The graph genus problem is NP-complete, *J. Algorithms* **1989**, *10*, 568–576.
- [21] Garçon, M.; Bakewell, C.; Sackman, G. A.; White, A. J. P.; Cooper, R. I.; Edwards, A. J.; Crimmin, M. R. A hexagonal planar transition-metal complex, *Nature* **2019**, *574*, 390–393.
- [22] Thomson, J. J. XXIV. On the structure of the atom: an investigation of the stability and periods of oscillation of a number of corpuscles arranged at equal intervals around the circumference of a circle; with application of the results to the theory of atomic structure, *Philos. Mag.* **1904**, *7*, 237–265.
- [23] *The PyMOL Molecular Graphics System 2.20*; Schrödinger LLC: New York, NY, 2015.
- [24] *MarvinSketch 19.26*; ChemAxon: Budapest, Hungary, 2019.
- [25] Flachsenberg, F.; Andresen, N.; Rarey, M. RingDecomposerLib: An Open-Source Implementation of Unique Ring Families and Other Cycle Bases, *J. Chem. Inf. Model.* **2017**, *57*, 122–126.

- [26] Bennett, W. E. Computation of the number of isomers and their structures in coordination compounds, *Inorg. Chem.* **1969**, *8*, 1325–1328.
- [27] Pinsky, M.; Avnir, D. Continuous Symmetry Measures. 5. The Classical Polyhedra, *Inorg. Chem.* **1998**, *37*, 5575–5582.
- [28] Wenzel, W.; Hamacher, K. Stochastic tunneling approach for global minimization of complex potential energy landscapes, *Phys. Rev. Lett.* **1999**, *82*, 3003.
- [29] Andresen, B.; Gordon, J. M. Constant thermodynamic speed for minimizing entropy production in thermodynamic processes and simulated annealing, *Phys. Rev. E* **1994**, *50*, 4346.
- [30] Yang, L.; Powell, D. R.; Houser, R. P. Structural variation in copper (I) complexes with pyridylmethanamide ligands: structural analysis with a new four-coordinate geometry index, τ_4 , *Dalton Trans.* **2007**, 955–964.
- [31] Okuniewski, A.; Rosiak, D.; Chojnacki, J.; Becker, B. Coordination polymers and molecular structures among complexes of mercury(II) halides with selected 1-benzoylthioureas, *Polyhedron* **2015**, *90*, 47–57.
- [32] Addison, A. W.; Rao, T. N.; Reedijk, J.; van Rijn, J.; Verschoor, G. C. Synthesis, structure, and spectroscopic properties of copper (II) compounds containing nitrogen–sulphur donor ligands; the crystal and molecular structure of aqua [1, 7-bis (N-methylbenzimidazol-2-yl)-2, 6-dithiaheptane] copper (II) perchlorate, *J. Chem. Soc. Dalton* **1984**, 1349–1356.
- [33] Zabrodsky, H.; Peleg, S.; Avnir, D. Continuous symmetry measures. 2. Symmetry groups and the tetrahedron, *J. Am. Chem. Soc.* **1993**, *115*, 8278–8289.
- [34] Alvarez, S.; Alemany, P.; Casanova, D.; Cirera, J.; Llunell, M.; Avnir, D. Shape maps and polyhedral interconversion paths in transition metal chemistry, *Coordin. Chem. Rev.* **2005**, *249*, 1693–1708.
- [35] Rauk, A.; Allen, L. C.; Mislow, K. Pyramidal Inversion, *Angew. Chem. Int. Ed.* **1970**, *9*, 400–414.
- [36] Berry, R. S. Correlation of Rates of Intramolecular Tunneling Processes, with Application to Some Group V Compounds, *J. Chem. Phys.* **1960**, *32*, 933–938.
- [37] Adams, W. J.; Thompson, H. B.; Bartell, L. S. Structure, Pseudorotation, and Vibrational Mode Coupling in IF₇: An Electron Diffraction Study, *J. Chem. Phys.* **1970**, *53*, 4040–4046.
- [38] Levenshtein, V. I. Binary codes capable of correcting deletions, insertions, and reversals. In *Phys.-Dokl.*, Vol. 10; 1966.

- [39] Andersen, J. L.; Flamm, C.; Merkle, D.; Stadler, P. F. Chemical Graph Transformation with Stereo-Information BT - Graph Transformation. In ; de Lara, J.; Plump, D., Eds.; Springer International Publishing: Cham, 2017.
- [40] Connelly, N. G.; Damhus, T.; Hartshorn, R. M.; Hutton, A. T., Eds.; *Nomenclature of Inorganic Chemistry*; The Royal Society of Chemistry: 2005.
- [41] Hanson, R. M.; Musacchio, S.; Mayfield, J. W.; Vainio, M. J.; Yerin, A.; Redkin, D. Algorithmic Analysis of CahnIngoldPrelog Rules of Stereochemistry: Proposals for Revised Rules and a Guide for Machine Implementation, *J. Chem. Inf. Model.* **2018**, *58*, 1755–1765.
- [42] Glendening, E. D.; Landis, C. R.; Weinhold, F. Natural bond orbital methods, *Wiley Interdiscip. Rev.: Comput. Mol. Sci.* **2012**, *2*, 1-42.
- [43] Knizia, G. Intrinsic atomic orbitals: An unbiased bridge between quantum theory and chemical concepts, *J. Chem. Theory Comput.* **2013**, *9*, 4834–4843.
- [44] McGregor, J. J. Backtrack search algorithms and the maximal common subgraph problem, *Software Pract. Exper.* **1982**, *12*, 23–34.
- [45] James, C. A.; Vandermeersch, T.; Dalke, A. “OpenSMILES specification”, 2015 last visited June 8, 2020.
- [46] Blaney, J. M.; Dixon, J. S. Distance Geometry in Molecular Modeling, *Rev. Comput. Chem.* **1994**, *5*, 299–335.
- [47] Dress, A. W. M.; Havel, T. F. Shortest-path problems and molecular conformation, *Discrete Appl. Math.* **1988**, *19*, 129–144.
- [48] Cherkassky, B. V.; Goldberg, A. V.; Radzik, T. Shortest paths algorithms: Theory and experimental evaluation, *Math. Program.* **1996**, *73*, 129–174.
- [49] Havel, T.; Wüthrich, K. A distance geometry program for determining the structures of small proteins and other macromolecules from nuclear magnetic resonance measurements of intramolecular 1H-1H proximities in solution, *B. Math. Biol.* **1984**, *46*, 673–698.
- [50] Liu, D. C.; Nocedal, J. On the limited memory BFGS method for large scale optimization, *Math. Program.* **1989**, *45*, 503–528.
- [51] Rappé, A. K.; Casewit, C. J.; Colwell, K. S.; Goddard, W. A.; Skiff, W. M. UFF, a Full Periodic Table Force Field for Molecular Mechanics and Molecular Dynamics Simulations, *J. Am. Chem. Soc.* **1992**, *114*, 10024–10035.

- [52] Jahn, H. A.; Teller, E. Stability of polyatomic molecules in degenerate electronic states-IOrbital degeneracy, *Proc. R. Soc. London, Ser. A* **1937**, *161*, 220–235.
- [53] Grimmel, S.; Reiher, M. The Electrostatic Potential as a Descriptor for the Protonation Propensity in Automated Exploration of Reaction Mechanisms, *Faraday Discuss.* **2019**, *220*, 443–463.
- [54] Proppe, J.; Reiher, M. Reliable estimation of prediction uncertainty for physicochemical property models, *J. Chem. Theory Comput.* **2017**, *13*, 3297–3317.
- [55] Brunken, C.; Bosia, F.; Grimmel, S.; Simm, G.; Sobez, J.-G.; Unsleber, J.; Vaucher, A. C.; Weymuth, T.; Reiher, M. “SCINE Utilities”, 2019 last visited June 8, 2020.
- [56] Guennebaud, G.; Jacob, B.; Others, “Eigen v3; <http://eigen.tuxfamily.org>”, 2010 last visited June 8, 2020.
- [57] Kolodzik, A.; Urbaczek, S.; Rarey, M. Unique ring families: A chemically meaningful description of molecular ring topologies, *J. Chem. Inf. Model.* **2012**, *52*, 2013–2021.
- [58] McKay, B. D.; Piperno, A. Practical graph isomorphism, II, *J. Symb. Comput.* **2014**, *60*, 94–112.
- [59] Lohmann, N. “JSON for Modern C++; <https://github.com/nlohmann/json>”, 2013 last visited June 8, 2020.
- [60] Clow, M. “Boost Algorithms; <https://www.boost.org>”, 2017 last visited June 8, 2020.
- [61] Capeletto, M. “Boost Bimap; <https://www.boost.org>”, 2017 last visited June 8, 2020.
- [62] Dawes, B. “Boost Filesystem; <https://www.boost.org>”, 2017 last visited June 8, 2020.
- [63] Rodgers, M. “Boost Functional; <https://www.boost.org>”, 2017 last visited June 8, 2020.
- [64] Siek, J.; Lumsdaine, A.; Lee, L.-Q. *The Boost Graph Library: User Guide and Reference Manual*; Addison-Wesley Longman Publishing Co., Inc.: USA, 2002.
- [65] Dawes, B.; Walker, D.; Prota, G.; Maddock, J. “Boost Integer; <https://www.boost.org>”, 2017 last visited June 8, 2020.

- [66] Agrawal, N. *et al.* “Boost Math; <https://www.boost.org>”, 2017 last visited June 8, 2020.
- [67] Cacciola, F. “Boost Optional; <https://www.boost.org>”, 2017 last visited June 8, 2020.
- [68] Douglas, N. “Boost Outcome; <https://www.boost.org>”, 2019 last visited June 8, 2020.
- [69] de Guzman, J.; Marsden, D.; Heller, T.; Fletcher, J. “Boost Phoenix; <https://www.boost.org>”, 2017 last visited June 8, 2020.
- [70] Vidal, M.; Sokolov, I.; Tanus, F.; Flinn, J.; Jarosch, T.; Schaeling, B.; Morgenstern, K. D. “Boost Process; <https://www.boost.org>”, 2017 last visited June 8, 2020.
- [71] Groves, N.; Ottosen, T. “Boost Range; <https://www.boost.org>”, 2017 last visited June 8, 2020.
- [72] de Guzman, J.; Kaiser, H.; Nuffer, D. “Boost Spirit; <https://www.boost.org>”, 2017 last visited June 8, 2020.
- [73] Friedman, E.; Maman, I. “Boost Variant; <https://www.boost.org>”, 2017 last visited June 8, 2020.
- [74] Wenzel, J. “Pybind11 2.4.2; <https://github.com/pybind/pybind11>”, 2017 last visited June 8, 2020.
- [75] Dagum, L.; Menon, R. OpenMP: an industry standard API for shared-memory programming, *IEEE Comput. Sci. Eng.* **1998**, *5*, 46–55.
- [76] Weininger, D. SMILES, a chemical language and information system. 1. Introduction to methodology and encoding rules, *J. Chem. Inf. Comp. Sci.* **1988**, *28*, 31–36.
- [77] Stein, S. E.; Heller, S. R.; Tchekhovski, D. An Open Standard for Chemical Structure Representation - The IUPAC Chemical Identifier. In *Nimes International Chemical Information Conference*; 2003.
- [78] Boyle, N. M. O.; Banck, M.; James, C. A.; Morley, C.; Vandermeersch, T.; Hutchison, G. R. Open Babel: An open chemical toolbox, *J. Cheminform.* **2011**, *3*, 1–14.
- [79] Ellson, J.; Gansner, E.; Koutsofios, L.; North, S. C.; Woodhull, G. Graphviz-open source graph drawing tools. In *International Symposium on Graph Drawing*; 2001.

- [80] Groom, C. R.; Bruno, I. J.; Lightfoot, M. P.; Ward, S. C. The Cambridge structural database, *Acta Crystallogr., Sect. B: Struct. Sci., Cryst. Eng. Mater.* **2016**, *72*, 171–179.
- [81] Delgado, E.; Hernandez, E.; Mansilla, N.; Moreno, M. T.; Sabat, M. Coordinative ability of the new compounds [Ti (η^5 -C₅H₄R)₂ (C≡CBu^t)₂](R= PPh₂, Ph₂P=O or Ph₂P=S) as precursors in the synthesis of heterodi- and heterotri-nuclear species. Crystal structure of [ClCu (μ - η^5 : κ P-C₅H₄PPh₂)₂ Ti (μ - η^2 -C≡CBu^t)₂ CuCl], *J. Chem. Soc., Dalton Trans.* **1999**, *999*, 533–538.